

ANALYSIS OF ELECTROMAGNETIC STIMULATION OF TRANSPORT
IN WATER FOR GEOENVIRONMENTAL APPLICATIONS

by

Mahsa Azad

A thesis

submitted in partial fulfillment

of the requirements for the degree of

Master of Science in Civil Engineering

Boise State University

December 2012

© 2012

Mahsa Azad

ALL RIGHTS RESERVED

BOISE STATE UNIVERSITY GRADUATE COLLEGE

DEFENSE COMMITTEE AND FINAL READING APPROVALS

of the thesis submitted by

Mahsa Azad

Thesis Title: Analysis of Electromagnetic Stimulation of Transport in Water for Geoenvironmental Applications

Date of Final Oral Examination: 19 October 2012

The following individuals read and discussed the thesis submitted by student Mahsa Azad, and they evaluated her presentation and response to questions during the final oral examination. They found that the student passed the final oral examination.

Arvin Farid, P.E., Ph. D.	Chair, Supervisory Committee
Jim Browning, Ph.D.	Member, Supervisory Committee
Elisa H. Barney Smith, Ph.D.	Member, Supervisory Committee
Jairo Hernandez, P.E., Ph. D.	Member, Supervisory Committee
Ron Phillips	Member, Supervisory Committee

The final reading approval of the thesis was granted by Arvin Farid, P.E., Ph. D., Chair of the Supervisory Committee. The thesis was approved for the Graduate College by John R. Pelton, Ph.D., Dean of the Graduate College.

DEDICATION

This work is dedicated to my wonderful mother and father, Mahnaz Vadiie and Ali Azad, for their timeless love and support and for instilling the importance of hard work and higher education in me.

ACKNOWLEDGEMENTS

I would first like to thank my advisor, Dr. Arvin Farid, for giving me the opportunity to participate in this research. I would like to also thank Dr. Jim Browning and Dr. Elisa Barney Smith my co-advisors and committee members for their constant support and advice. I would like to thank Dr. Jairo Hernandez, and Mr. Ron Phillips for generously participating in my committee. Special thanks to Mr. Philip Boysen for his help with the design and machining of several pieces of my experimental setup. Thanks to Sahba Azad, my dear sister, for her continuous assistance and encouragement in the lab. I would also like to acknowledge Arman Tajarrod. There is no doubt in my mind that without his continued support and counsel I could not have completed this process.

ABSTRACT

Air sparging is a popular soil and groundwater remediation technique, which enables the removal of volatile organic compounds (VOCs) through diffusing contaminant-free air into saturated zones of soil. However, the VOC removal process is slow due to the soils' low permeability, and might take months to years depending on the type of the soil and contaminant. The goal of this thesis is to study the effect of electromagnetic (EM) waves —with minimal heat generation— on transport mechanisms such as diffusion, in order to improve airflow and expedite the cleanup process using air sparging or similar technologies. Because water dipole molecules oscillate under alternating electric fields, EM waves can enhance transport mechanisms such as diffusion in saturated media. This effect is studied through an experimental setup that examines the diffusion of a nonreactive dye into water.

Prior experimental work is analyzed and simulated by the author to find the potential correlation between the electric field magnitude/power and the flow characteristics of the dye. The experiment is simulated using the finite element software, COMSOL Multiphysics, to obtain a full vector representation of the EM field. In addition, the results from the digital analysis of the prior work are manipulated to study the concentration of the dye as well as the flow rate at different locations and times for all tests. The study, however, proved the necessity of a modified experimental setup for finding the correlation between the electric field pattern and the flow of the dye. For this

reason, a modified experimental setup was developed. The new setup was tested at a range of frequencies 50-200 MHz. Measurement of the electric field component of EM waves is taken to map the electric field. In addition, the electric fields are simulated in COMSOL Multiphysics for better 3D visualization and analysis. A dielectrophoretic study is performed on the simulation data. The result of this study is in agreement with the experimental result of the dye flow.

Recording the temperature change of the medium for different frequencies shows the same trend of the temperature change (less than 1°C) for all tests. However, only at the specific frequency of 65 MHz did the dye flow occur. Therefore, this observation suggest that thermal effects are not controlling the movement of the dye in the water. Since the flow of the dye is in the direction of the dielectrophoretic forces, it is believed that the governing mechanism for the dye transport is mainly dielectrophoresis.

TABLE OF CONTENTS

DEDICATION	iv
ACKNOWLEDGEMENTS	v
ABSTRACT	vi
LIST OF TABLES	xi
LIST OF FIGURES	xii
LIST OF ABBREVIATIONS	xviii
CHAPTER ONE: INTRODUCTION	1
Motivation	1
Scope	8
Simulation, Digital Analysis, and Evaluation	8
Improved Experimental Setup	9
Objectives	10
CHAPTER TWO: BACKGROUND	11
Diffusion	11
Diffusion and Advection	13
Diffusion in Porous Media	14
EM Wave Propagation	16
Rectangular Cross-Section Resonant Cavity	17
Dielectrophoresis	23

Heat Transfer and Convective Flow	24
CHAPTER THREE: MATERIALS AND METHODS	26
Section 1: Simulation, Digital Analysis, and Evaluation.....	26
Sangrey’s Experimental Setup.....	26
Simulation.....	37
Digital Analysis and Evaluations.....	40
Section 2: Improved Experimental Setup	43
CHAPTER FOUR: SUMMARY OF RESULTS AND DISCUSSION	73
Section 1: Simulation, Digital Analysis, and Evaluations	73
Simulations	73
Digital Analysis and Evaluation	79
Section 2: Modified Setup	86
Unstimulated Tests.....	86
Stimulated Tests.....	87
CHAPTER FIVE: CONCLUSION.....	108
Stimulating Effects.....	108
Effects of Power Level.....	109
Modified Experimental Setup.....	109
Temperature Effect	110
Dielectrophoresis Study	111
Digital Analysis	112
Image Pixel-Intensity Summation.....	112
Finger-Width Profile.....	113

Conclusion	113
REFERENCES	115
APPENDIX A.....	118
Simulation of Sangrey’s (2011) Experimental Setup in COMSOL Multiphysics....	118
APPENDIX B	130
Simulation of a Resonant Cavity for the Modified Experimental Setup	130
APPENDIX C	139
Script (m.file) Code Developed in MATLAB for Calculation of Diffusion Coefficient, D , in Zone 4	139
APPENDIX D.....	142
Script (m.file) Code Developed in MATLAB for Calculation of Electric Field Gradient for Dielectrophoresis Study	142
APPENDIX E	145
Script (m.file) Code Developed in MATLAB to Study Pixel Intensity Summation	145
APPENDIX F.....	154
Script (m.file) Code Developed in MATLAB to Study the Fingers Width vs. Power	154

LIST OF TABLES

Table 4.1	Diffusion Coefficient for Zone 4, calculated according to Equation 30...	85
Table 4.2	Diffusion Coefficient for Zone 2, calculated according to Equation 30...	85
Table A.1	List of parameters used for modeling	119
Table A.2	Dielectric Properties.....	126
Table B.1	List of parameters used for modeling	131
Table B.2	Dielectric Properties.....	136

LIST OF FIGURES

Figure 1	Illustration of the AS/SVE remediation concept. Through injecting air beneath a groundwater aquifer, air sparging operation can promote the volatilization or biodegradation of dissolved organic contaminants. Vapor extraction wells then create a vacuum in the subsurface to direct the flow of vapors to extraction wells (Marley et al., 1996).	2
Figure 2	Conceptual sketch of air channels and mass transfer zones (Braida and Ong, 2001).	5
Figure 3	Real (ϵ') and imaginary (ϵ'') dielectric constant and conductivity (ϵ''') of soil at different frequencies (Hilhorst, 1998).	7
Figure 4	Rectangular waveguide with its dimensions (Balanis, 1989).	18
Figure 5	Field patterns for the first 18 TE^z and / or TM^z modes (coordinate axis is shown in Figure 4) in a rectangular waveguide with $a / b = 2$ (Lee et al., 1985).	20
Figure 6	The schematic Q calculation diagram.	21
Figure 7	Coaxial transmission line to rectangular waveguide coupling: (a) The side and (b) the end views of a coaxial antenna to a waveguide electric field coupling for TE_{10} mode. (c) The side and (d) the end view for the coaxial antenna to a waveguide magnetic field coupling for TE_{10} modes (Balanis, 1989).	23
Figure 8	Sangrey's setup (2011) and experimental setup for EM-stimulated tests.	28
Figure 9	Random dye movement during the unstimulated test.	28
Figure 10	Locations of the 208 nodes used in digital pixel analysis.	30
Figure 11	Dye flow during the stimulated test with a larger concentration toward the right side of the medium.	31
Figure 12	Zones 1 through 5 used for image analysis (Sangrey, 2011).	32
Figure 13	Zones 4 and 2, diverging concentrations of 50W EM-stimulated test. The spike at 33 minute indicates the start of stimulation (Sangrey, 2011).	33

Figure 14	Zones 4 and 2, diverging concentrations in 30-W EM-stimulated test. The spike at 33 minute indicates the start of stimulation (Sangrey, 2011). 33
Figure 15	Zones 4 and 2, diverging concentrations in 10-W EM-stimulated test. The spike at 33 minute indicates the start of stimulation (Sangrey, 2011). 34
Figure 16	Zones 4 and 2, diverging concentrations in unstimulated test (Sangrey, 2011). 34
Figure 17	Linear fit-lines to concentration increases (Sangrey, 2011). 36
Figure 18	Rate (a representative of flux) of dye entering Zone 4 based on slopes of concentrations (Sangrey, 2011). 37
Figure 19	Simulated model for Sangrey’s setup. 38
Figure 20	a) Coaxial antenna structure used in experiment, b) Coaxial antenna structure detail simulated in COMSOL Multiphysics. 39
Figure 21	Nodes selected for digital analysis with grouped nodes “a” and “d” along a contour line, and group nodes “b” and “c” perpendicular to the contour line..... 41
Figure 22	Resonant cavity inside the acrylic box, bottom and sides of the resonant cavity are made of copper mesh to enable visualization but the top is from a copper plate to provide a closed resonant cavity. 45
Figure 23	Injection cup on acrylic pedestal attached to a copper plate to hold the dye after injection. 46
Figure 24	Depth (vertical, YZ) slice normalized electric field map of experimentally measured (left) and simulated in COMSOL Multiphysics (right), a) Schematic of locations of depth slices, b) Slice 1, c) Slice 2..... 48
Figure 24 (Cont.)	Depth (vertical, YZ) slice normalized electric field map of experimentally measured (left) and simulated in COMSOL Multiphysics (right), a) Schematic of locations of depth slices, d) Slice 3, e) Slice 4, f) Slice 5, and g) Slice 6. 49
Figure 25	Experimental medium for the modified setup showing the acrylic box, resonant cavity filled with water, injection cup, injection pipette, and loop antenna. 50
Figure 26	Green food color used as the diffusing material in the experiment. 52
Figure 27	S_{11} (dB) of the medium when using a probe coupling..... 54

Figure 28	S_{11} (dB) of the medium when using a loop coupling.....	55
Figure 29	Grounding loop antenna by connecting antenna to top boundary of resonant cavity, photo of top surface of resonant cavity.	56
Figure 30	Schematic of impedance-matching network.....	57
Figure 31	Test apparatus used in modified experimental setup including amplifier, signal generator, spectrum analyzer, and the dual-direction coupler and matching box (respectively, right and left on the black table).....	58
Figure 32	(a) Lighting frames with a layer of Lycra and the additional frame with another layer of Lycra to create uniform lighting and (b) above-mentioned frames when lights are on.	60
Figure 33	Triaxial antenna-positioner connected to measuring coaxial, monopole probe.	62
Figure 34	Output file of LABVIEW showing Cartesian coordinates of each measuring node as well as measured power magnitude.	64
Figure 35	Modified experimental setup as modeled in COMSOL Multiphysics. The coordinate system shows the axes direction and the origin of the axes. The numbers in the figure are in meters.....	66
Figure 36	Location of nodes used to analyze effect of electric field pattern in COMSOL Multiphysics. The numbers in the figure are in meters.....	68
Figure 37	Study zone in Intensity Summation analysis referred to as upper zone. ..	70
Figure 38	The study zone in the Finger Height analysis referred to as the finger zone.	72
Figure 39	Schematic of locations (top view of the setup) of field mapping on depth (vertical) slices.....	74
Figure 40	Experimentally measured (left) and simulated in COMSOL Multiphysics (right) normalized electric field color map for depth-slices of Figure 39: a) Slice 1 (XZ Slice), b) Slice 2 (XZ Slice).	75
Figure 40 (Cont.)	Experimentally measured (left) and simulated in COMSOL Multiphysics (right) normalized electric field color map for depth-slices of Figure 39: c) Slice 3 (XZ Slice), d) Slice 4 (YZ Slice), e) Slice 5 (YZ Slice), f) Slice 6 (YZ Slice).....	76

Figure 40 (Cont.)	Experimentally measured (left) and simulated in COMSOL Multiphysics (right) normalized electric field color map for depth-slices of Figure 39: g) Slice 7 (YZ Slice), h) Slice 8 (YZ Slice), and i) Slice 9 (YZ Slice).	77
Figure 41	Grouped nodes used for investigation of effect of electric field magnitude on dye concentrations in Sangrey’s work (2011). All parallel lines are located at a 2cm distance from their neighboring lines. Locations of perpendicular line-crossings coincide with nodes used in digital analysis.	79
Figure 42	Change of Concentration over time for Group 1 for: (a) 0 W, (b) 10 W, (c) 30 W, (d) 50 W; ‘a’ and ‘d’ are groups of nodes tangential to electric field contour lines, and ‘b’ and ‘c’ are groups of nodes normal to electric field contour lines.....	81
Figure 43	Change of Concentration over time of Group 2, for (a) 0 W, (b) 10 W, (c) 30 W, (d) 50 W; ‘a’ and ‘d’ are groups of nodes tangential to electric field contour lines, and ‘b’ and ‘c’ are groups of nodes normal to electric field contour lines.....	82
Figure 44	Average diffusion coefficient (D) versus power for Zones 2 and 4 of Sangrey’s (2011) results.	86
Figure 45	Dye transport during unstimulated test; dye randomly rises out of injection cup and descends.....	87
Figure 46	Dye flow in an EM-stimulated experiment at 65 MHz frequency and power level of 10 W at 20 minutes; dye rises out of injection cup toward top boundary.	88
Figure 47	Dye flow in an EM-stimulated experiment at 65 MHz frequency and power level of 20 W at 20 minutes; dye rises toward top boundary at a faster rate compared to 10 W case.	89
Figure 48	Dye flow in an EM-stimulated experiment at 65 MHz frequency and power level of 30 W at 20 minutes; dye rises out of injection cup toward top boundary at a faster rate compared to 10 W and 20 W cases.	89
Figure 49	Dye flow in an EM-stimulated experiment at 60 MHz frequency and power level of 30 W; dye rises out of injection cup and descends toward bottom boundary similar to unstimulated tests.	92
Figure 50	Dye flow in an EM-stimulated experiment at 65 MHz frequency and power level of 30 W; dye rises out of injection cup toward top boundary.	92

Figure 51	Dye flow in an EM-stimulated experiment at 69 MHz frequency and power level of 30 W; dye rises out of injection cup and descends toward bottom boundary similar to unstimulated tests.	93
Figure 52	Dye flow in an EM-stimulated experiment at 75 MHz frequency and power level of 30 W; dye stays in injection cup as long as medium is stimulated.....	93
Figure 53	Dye flow in an EM-stimulated experiment at 77 MHz frequency and power level of 30 W; dye rises out of injection cup and descends toward bottom boundary similar to unstimulated tests.	94
Figure 54	Change of water temperature 1 cm away from the center of the loop antenna at different frequencies over time for an RF power of 30 W.	95
Figure 55	Plot of average magnitude of electric field over volume versus frequency for simulation data using COMSOL Multiphysics to represent quality factor (Q -value); two peaks occur at first two modes, TE_{110} and TE_{111}/TM_{111} at 62 MHz and 75 MHz, respectively in the ascending frequency order.	96
Figure 56	Map of experimentally measured electric field normalized to maximum electric field value in entire cavity, with maximum electric field at 65 MHz and 30 W of power.	97
Figure 57	Contour map of Z-component of ∇E^2 (V^2/m^3) according to COMSOL Multiphysics results at 65 MHz.	100
Figure 58	Contour map of X-component of ∇E^2 (V^2/m^3) according to COMSOL Multiphysics results at 65 MHz.	100
Figure 59	Plot of adjusted sum of image pixel intensities (representing transported dye amount) vs. time for unstimulated test, three stimulated tests at 65 MHz at power levels of 10 W, 20 W, and 30 W as well as a stimulated test at 75 MHz and 30 W; summation is performed over upper zone in digital images.	103
Figure 60	Plot of adjusted sum of pixel intensities (representing transported dye) vs. power for unstimulated test, three stimulated tests at 65 MHz and 10 W, 20 W, and 30 W, and stimulated test at 75 MHz and 30 W; summation is performed over upper zone in digital images.	104
Figure 61	Plot of total of number of pixels containing enough dye to be considered a finger (representing width of the dye finger) accumulated over time vs. vertical distance above injection cup.	106

Figure A.1 Schematic of experimental setup of Sangrey (2011). 120

LIST OF ABBREVIATIONS

AC	Alternating Current
AS	Air Sparging
CPVC	Chlorinated PolyVinyl Chloride
CW	Continuous Wave
DC	Direct Current
EM	Electromagnetic
FD	Finite Difference
MTZ	Mass Transfer Zone
PEC	Perfect Electric Conductor
RC	Resonant Cavity
RF	Radio Frequency
SVE	Soil Vapor Extraction
TE	Transverse Electric
TM	Transverse Magnetic
VOC	Volatile Organic Compound

CHAPTER ONE: INTRODUCTION

Motivation

Remediation of contaminated soil and groundwater has become an important area of interest to most federal and state agencies in recent decades. This interest is especially significant given that about 23% of the freshwater used in the United States in 2005 came from groundwater sources (USGS, 2005). Several remediation techniques have been used for removing the contaminants among which air sparging (Johnson et al., 1998) is recent and very popular. In-situ air sparging (AS) is a technique in which air or oxygen is injected into water-saturated zones for the purpose of removing organic contaminants by a combination of volatilization and aerobic biodegradation processes. This technology involves the injection of contaminant-free air into the saturated zones of the subsurface, enabling a phase transfer of organic contaminants from a dissolved or adsorbed state to a vapor phase. Air sparging is most often used with soil vapor extraction (SVE), which creates a negative pressure in the unsaturated zone —above the water table level— through a series of extraction wells to control the vapor plume migration and to capture vapors. Figure 1 illustrates an AS/SVE in-situ remediation field setup.

Air sparging can be used to mitigate liquefaction as well. During an earthquake, for example, the sudden rise in pore water pressure can cause a sudden drop in effective stress, resulting in saturated loose sandy layers losing their shear strength, causing liquefaction of the sand and large settlements and foundation/structure damage (Yegian et

al., 2007). Research has shown that a small reduction in the degree of saturation of fully-saturated sand can result in a significant increase in the shear strength against liquefaction. Yegian et al. (2007) proposed and proved that air sparging can be used as an innovative way to mitigate liquefaction.

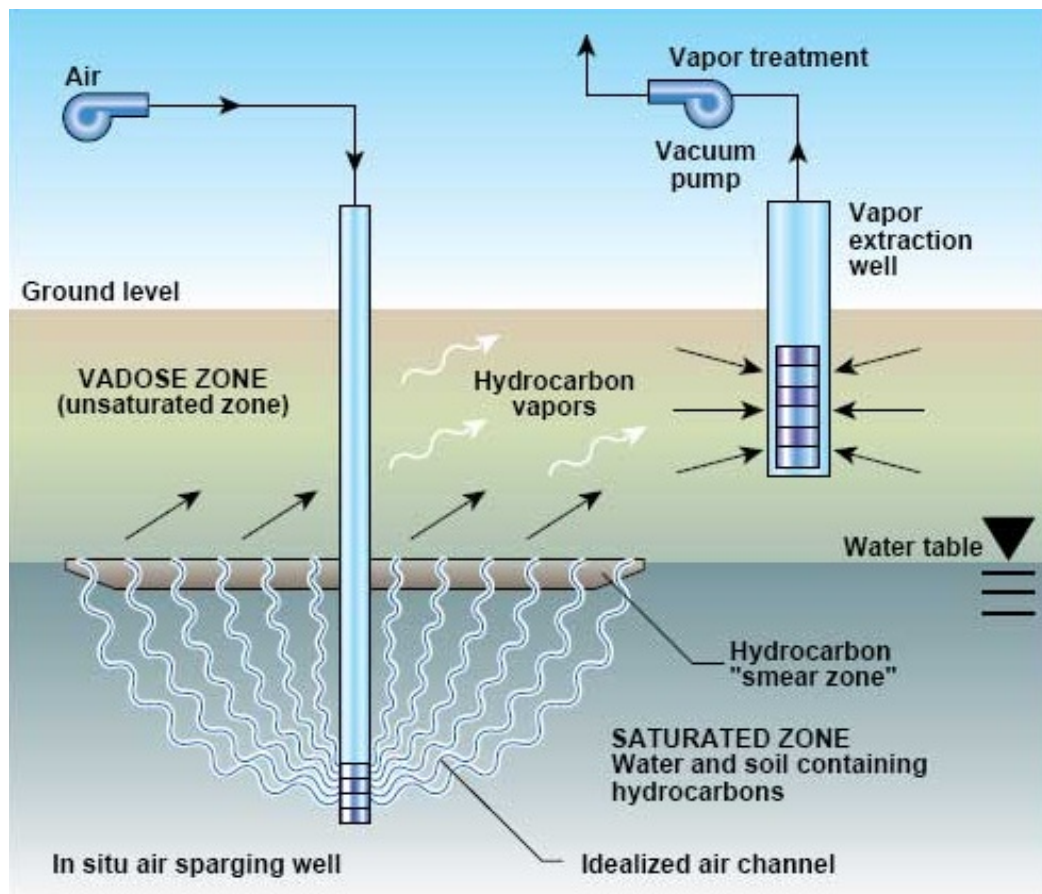


Figure 1 Illustration of the AS/SVE remediation concept. Through injecting air beneath a groundwater aquifer, air sparging operation can promote the volatilization or biodegradation of dissolved organic contaminants. Vapor extraction wells then create a vacuum in the subsurface to direct the flow of vapors to extraction wells (Marley et al., 1996).

Despite the impressive effects, AS is limited because it is considered a semi-random remediation process (Braid and Ong, 2001). Pumping air into the saturated

regions creates bubbles and decreases the degree of saturation of soil in preferred zones. At a specific saturation degree, the bubbles create random air channels. Since air can flow more easily in partially saturated media compared to water-saturated ones, the flow of air starts and continues only through the already randomly-formed air channels. The possibility of forming new air channels, even using pulsation of AS well pumps, is low. Braida and Ong (2001) pointed out that the area surrounding individual air channels, referred to as the Mass Transfer Zone (MTZ), is the region through which air diffuses and through which treatment of contaminants occurs but at an extremely slow rate. Figure 2 shows the conceptual illustration of the air channels and MTZ. Chao et al. (1998) compared the cleanup rate outside and inside air channels and concluded that the cleanup outside air channels was negligible. As a result, several portions of contaminated regions would not be exposed to the air and would remain untreated. Thus, the efficiency of air sparging for the remediation of contaminants depends on the flow paths of this semi-random air channel formation, which depends on the soil properties and is out of the users' control.

Several methods have been proposed for improving AS including pulsation of injection pumps at different periods and patterns (Benner et al., 2002). Although it is effective, pulsation of air pumps is time consuming because of the time lost when the system is off. Using direct electric current (DC) or alternating current (AC) is another proposed and applied method in saturated soils (Suthersan and Raton, 1999). Direct current (DC) can generate and control contaminate transport and the flow of oxygen in the direction of the electric current. DC may help to diffuse more air out of the air channels as well as alter air channel formation. The new air channels will probably be

created wherever the electric conductivity is larger, which is in locations of high moisture content due to the higher porosity. Once several channels are formed, the preferential paths would be the existing formed air channels. As a result, the airflow paths would still be limited. Although the heat produced by DC enhances the diffusion between air channels, there may be adverse effects on microbial activity due to the resulting heat generated by DC and AC and due to altered pH by DC.

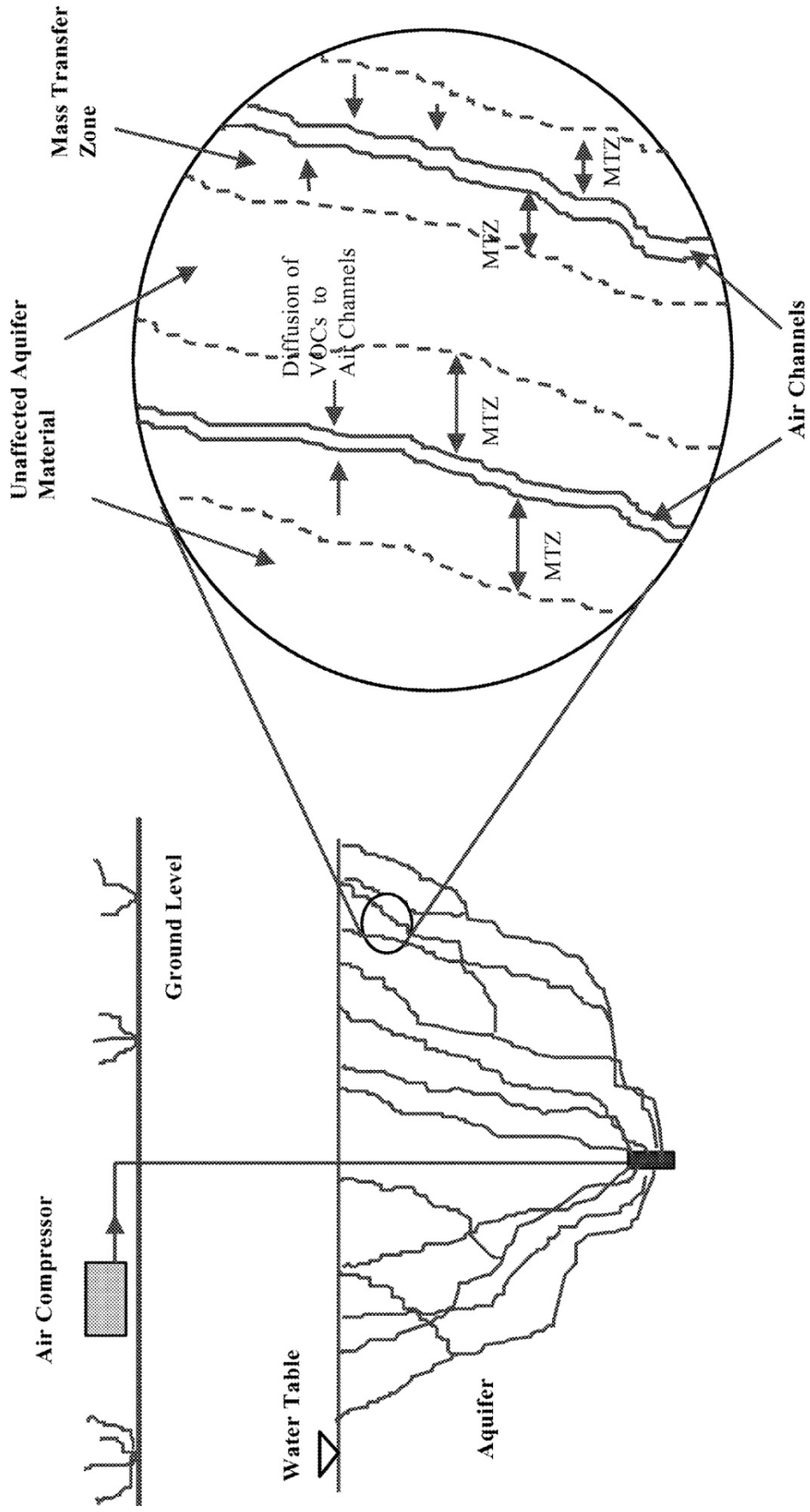


Figure 2 Conceptual sketch of air channels and mass transfer zones (Braida and Ong, 2001).

Other researchers have studied the effect of EM waves on air sparging. Most studies of EM stimulation of AS are about EM heating. Vermeulen and McGee (2000) studied the use of EM heating of the environment. They used low frequency EM waves (60 Hz) to heat the soil in order to change the viscosity of energy fuels to promote removal of contaminants. They observed that EM power heats the soil and brings the vapor pressure to a point where SVE is more efficient. Price et al. (1999) studied the same phenomenon and performed in-situ tests with a 25-kW radio frequency (RF) wave generator used in conjunction with air sparging and SVE wells. The results showed an increased removal of gasoline range organic compounds. However, the negative environmental impacts due to overheating of biological organisms were never investigated.

The goal of this research is to study the effect of electromagnetic waves on transport mechanisms at frequencies ranging between 50MHz-200MHz where heat generation is minimal (e.g., less than 1°C). Because EM waves oscillate dipole water molecules, it can enhance several transport mechanisms such as diffusion in saturated media. As a result, EM stimulation can improve airflow in saturated soil and, therefore, expedite the cleanup process using air sparging or similar technologies.

Because mass transfer during AS is assumed to be controlled by diffusion (Braid and Ong, 2001), increasing the existing diffusion rate would improve the efficiency of the AS technique. An advantage of EM over other enhancement methods such as DC is that EM waves can be applied at low frequencies (MHz) and, therefore, would dissipate a small amount of energy in the medium. Then the water temperature would only be slightly affected due to its high heat capacity. This issue is important because the

generation of heat can affect microbial activities within the soil. However, according to the Wagner relaxation theorem (Figure 3), applying the EM waves at lower frequencies would lead to higher values of the electric permittivity of the water molecules. In other words, the alignment of the water molecules with the electric field occurs more easily, and therefore oscillation of the molecules by applying an oscillating electric field would be more feasible. The fluctuations of molecules would enhance any transport mechanism within saturated regions of the soil. In addition, EM waves propagate better through zones of low electric conductivity, which are zones with lower moisture content. These are regions where the flow of air and electric currents are limited due to smaller pores and lower electrical conductivity. However, more diffusion can take place in those regions after EM stimulation.

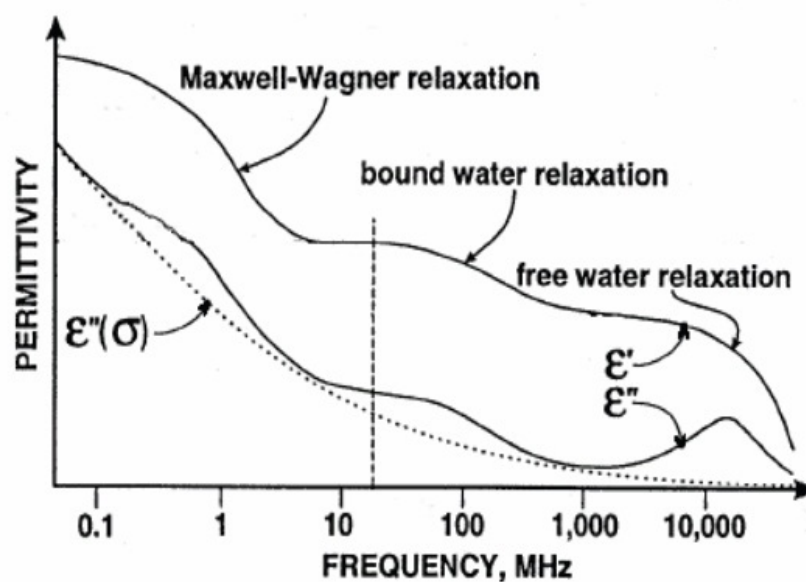


Figure 3 Real (ϵ') and imaginary (ϵ'') dielectric constant and conductivity (ϵ''') of soil at different frequencies (Hilhorst, 1998).

Scope

This work includes a quantitative study of “EM stimulation of water for geotechnical applications” by Sangrey (2011), referred to as the “previous work” or “Sangrey’s work.” Sangrey prepared an experimental setup for observation of the effect of EM waves on the transport mechanism of a nonreactive dye in water. The EM wave propagation of that experiment is simulated in COMSOL Multiphysics here, and the experimental results of that work are analyzed to find the correlation between the electric power magnitude and the transport mechanism. As is discussed in the next chapters, the simulation and analysis proved that it was essential to modify the experimental setup for a more precise analysis. In the next chapters, a modified setup is explained in detail, and several analyses are performed to investigate the effects of EM stimulation on the transport mechanism.

For a better understanding of the work performed, the methodology and the results are categorized in two different sections. In the first section, “Simulation, Digital Analysis and Evaluation,” the previous experimental setup is simulated and analyzed to find the correlation factors. In the second section, “Improved Experimental Setup,” the new experimental setup is discussed. The experimental and simulation results of the new setup are analyzed. The tasks of this work are listed and briefly introduced in the following.

Simulation, Digital Analysis, and Evaluation

Below is the list of tasks performed to analyze the previous experimental setup.

- Simulation of EM waves to obtain a 3D visualization of the electric vector field provided in the experiment: The experiment is simulated by a finite element method using COMSOL Multiphysics software for visualization of the three components of electric and magnetic fields. An attempt is made to validate the simulated electric field by comparing it with the experimentally measured field.
- Evaluation of diffusion coefficient for each experimental setup using the provided data from the experiment and analysis of digital images: Digital imaging of the dye diffusion process was performed to record the concentration of the dye at various locations over time with and without EM stimulation. The data from the digital analysis of these pictures are analyzed to quantify the transport rate.

Improved Experimental Setup

Below is the list of tasks performed to improve the previous experimental setup to obtain more accurate results.

- Preparation of an experimental setup to study the effects of EM waves on diffusion in saturated media. For this purpose, the diffusion of a nonreactive, inert dye in water is studied as a visible analogy to airflow in saturated media: A 40 cm × 40 cm × 40 cm acrylic box containing a 38 cm × 38 cm × 38 cm resonant cavity (RC) made of copper mesh is filled with water. A coaxial antenna connected to the EM-wave source coupled to the resonant cavity, launches EM waves into the medium. The resonant cavity provides a standing wave pattern and strengthens the field. The vertical component of the electric field is measured to validate the simulated field in COMSOL Multiphysics.

- Simulation of EM waves to obtain the *3D* visualization of the electric vector field provided in the experiment: The experiment is simulated in COMSOL Multiphysics to obtain a 3D visualization of the electric field.
- Digital image analysis of the transport of the dye in the improved setup: The transport of the dye is recorded with and without EM stimulation of the medium. Digital images are processed to quantify the effect of EM stimulation (e.g., electric field frequency and power) on the flow pattern.

Objectives

The most important objective of this work is to find the governing phenomenon that directs the movement of the dye when EM stimulation is applied. Studying the relationship between the magnitude of the EM power and the transport rate, or a representative of the transport rate, is another objective of this work.

CHAPTER TWO: BACKGROUND

Diffusion

The theory of diffusion describes the spread of particles through random motion depending on their interactions with the surrounding particles from regions of higher concentration to regions of lower concentration. Diffusion can be described by a partial differential equation that incorporates the variables influencing the physical mechanism of matter transport. Although the movement of individual particles is random, if there is a gradient in the concentration of the quantity, there will be a net flux in the system in order to reduce this gradient. Hence, this gradient will consequently be reduced until the net flux of the system and the gradient approaches zero.

According to Fick's first law, the rate of diffusion (flux) is proportional to the gradient of the concentration of the substance,

$$\vec{F} = -\bar{D} \cdot \vec{\nabla}C \quad (1)$$

where \vec{F} is the rate of diffusion ($\text{g}/\text{m}^2\text{s}$), \bar{D} is the diffusion coefficient tensor (m^2/s), and C is the concentration of the diffusing matter (g/m^3).

Fick's second law relates the spatial and temporal variations of the diffusing matter concentration via the diffusion coefficient. It states that the temporal variations of the concentration at each point in space is related to the divergence of the rate (flux) of diffusion (i.e., net flow into the element). Assuming $D_{xy} = D_{yx} = D_{xz} = D_{zx} = D_{yz} = D_{zy} = 0$,

and D_x , D_y , and D_z are the diffusion coefficient in x, y, and z direction, respectively (X, Y, and Z are the coordinate axes (m)), Fick's 2nd law can be written as

$$\frac{\partial C}{\partial t} = -\vec{\nabla} \cdot \vec{F} = \frac{\partial}{\partial x} \left(D_x \frac{\partial C}{\partial x} \right) + \frac{\partial}{\partial y} \left(D_y \frac{\partial C}{\partial y} \right) + \frac{\partial}{\partial z} \left(D_z \frac{\partial C}{\partial z} \right), \quad (2)$$

where t is time (s). For a homogenous and isotropic medium such as the water medium of our experiment, ($D_x = D_y = D_z = D$), Fick's second law in three dimensions would be simply expressed as

$$\frac{\partial C}{\partial t} = D \left(\frac{\partial^2 C}{\partial x^2} + \frac{\partial^2 C}{\partial y^2} + \frac{\partial^2 C}{\partial z^2} \right). \quad (3)$$

In order to solve Eqn. 3 for the diffusion coefficient, D , one needs to know the concentration at different nodes at different times. The medium can be discretized, and Eqn. 3 can then be solved for D using a 3D finite element or finite difference method. However, solving Eqn. 3 for the concentration when the value of the diffusion coefficient is known is more complicated. For a semi-infinite slab, with constant concentrations of C_0 and C_∞ at $z = 0$ and $z = \infty$, respectively, the solution can be simplified using the method of "combination of variables," as introduced by Boltzman in 1894 (cited in Cussler, 1997), to transform the partial differential equation to an ordinary differential equation. This approach assumes the diffusion coefficient is not a function of time, concentration, or position. Assuming a new variable, $\zeta = \frac{x_i}{\sqrt{4Dt}}$ where x_i can represent X, Y, or Z (Cussler, 1997), Eqn. 3 can be rewritten as:

$$\frac{dC}{d\xi} \left(\frac{\partial \xi}{\partial t} \right) = D \left(\frac{d^2 C}{d\xi^2} \left(\frac{d\xi}{dx_i} \right)^2 \right) \quad (4)$$

which can be simplified to the

$$\frac{d^2C}{d\xi^2} + 2\xi \frac{dC}{d\xi} = 0. \quad (5)$$

In other words, the partial differential equation has been transformed into an ordinary differential equation. One integration of Eqn. 5 over ξ gives:

$$\frac{dC}{d\xi} = ae^{-\xi^2}, \quad (6)$$

where a is an integration constant that can be found using boundary conditions. A second integration and use of boundary conditions gives:

$$\frac{C - C_0}{C_\infty - C_0} = \text{erf } \xi, \quad (7)$$

where $\text{erf } \xi = \frac{2}{\sqrt{\pi}} \int_0^\xi e^{-s^2} ds$, which is the error function of ξ . This result gives the desired concentration profile providing the variation of the concentration with position and time. This solution, however, is not the general solution to Fick's second law. In general, when the diffusion coefficient is known, a system of simultaneous equations should be solved for obtaining the concentrations at different times and locations.

Diffusion and Advection

If advection is present along with diffusion, the total flux would be

$$\vec{J} = \vec{F} + C\vec{V}, \quad (8)$$

where \vec{J} is the total flux ($\text{g/m}^2\text{s}$), \vec{F} is the flux due to only diffusion ($\text{g/m}^2\text{s}$), C is the concentration (g/m^3), and \vec{V} is the velocity of the particles carried by the background (in this case water) flow (m/s).

Diffusion in Porous Media

In a porous medium, diffusion takes place in the liquid phase enclosed by a porous solid (Domenico and Schwartz, 1997). Diffusion in a porous medium such as soil obeys rules similar to the above-mentioned ones. However, additional parameters need to be introduced in Eqns. 1 and 2. One important reason is that there is no diffusion through the solid matrix (soil grains). Hence, only a reduced area is available for diffusion. Another significant difference is due to tortuosity; diffusion takes place over a longer distance in a porous medium than in a homogeneous medium. In addition, the effect of viscous forces in small pores mitigates turbulence. According to Domenico and Schwartz (1997), Fick's first law in the fluid phase of saturated, porous sediments can be written as

$$\vec{F} = -D \left(\frac{\partial Cn}{\partial x} \hat{i} + \frac{\partial Cn}{\partial y} \hat{j} + \frac{\partial Cn}{\partial z} \hat{k} + \frac{\vec{\tau}'}{\nabla} \right), \quad (9)$$

where n is porosity, τ' is the tortuosity vector (g/m) to account for the hindering of free diffusion by collision with pore walls, and ∇ is the averaging volume (m^3). This form has prompted the definition of a bulk diffusion coefficient, D^* , to account for the effects of tortuosity

$$\vec{F} = -D^* n \left(\frac{\partial C}{\partial x} \hat{i} + \frac{\partial C}{\partial y} \hat{j} + \frac{\partial C}{\partial z} \hat{k} \right). \quad (10)$$

As a result, Fick's 2nd law will be

$$\frac{\partial(nC)}{\partial t} = \frac{\partial}{\partial x} \left(D^* n \frac{\partial C}{\partial x} \right) + \frac{\partial}{\partial y} \left(D^* n \frac{\partial C}{\partial y} \right) + \frac{\partial}{\partial z}. \quad (11)$$

With the further assumption that porosity and D^* do not vary spatially, Eqn. 11 can be simplified to the form

$$\frac{\partial C}{\partial t} = D^* \left(\frac{\partial^2 C}{\partial x^2} + \frac{\partial^2 C}{\partial y^2} + \frac{\partial^2 C}{\partial z^2} \right). \quad (12)$$

In the absence of an equivalent D^* , Eqn. 10 can also be written using an effective diffusion coefficient, D'

$$\vec{F} = -\dot{D} \left(\frac{\partial C}{\partial x} \hat{i} + \frac{\partial C}{\partial y} \hat{j} + \frac{\partial C}{\partial z} \hat{k} \right), \quad (13)$$

where \dot{D} is related to D using different expressions available. One example of these expressions is the Greenkorn and Kessler, 1972 (as cited in Domenico and Schwartz, 1997), definition

$$D' = \frac{n}{\tau} D. \quad (14)$$

In this latter formulation, the tortuosity is defined as the square root of the ratio of the length of a flow channel for a fluid particle to the length of a porous medium sample.

Transport of gas in water or fluids in porous media obeys the same rules. However, the transport depends on the degree of water saturation. Fick's first and second laws for the transport of gas in porous media are the same as Eqns. 10 and 11. However, the porosity should be replaced by n_g , which is the part of total porosity occupied by the gas phase (as cited in Domenico and Schwartz, 1997). In addition, the diffusion coefficient D^* in unsaturated zones is an effective diffusion coefficient that is obtained from

$$D^* = \tau D, \quad (15)$$

where D is the diffusion coefficient of the diffusing gas in air and τ , the tortuosity, is frequently taken from the empirical development of Millington and Quirk, 1961, (as cited in Domenico and Schwartz, 1997).

$$\tau = \frac{n_g^{7/3}}{n^2} . \quad (16)$$

EM Wave Propagation

During the EM stimulation, the major task is to correlate the transport mechanism to the electric field component of the EM waves in the medium. Electromagnetic analysis involves solving Maxwell's equations subject to certain boundary conditions. Maxwell's equations are a set of equations, written in a differential or integral form, stating the relationships between the fundamental electromagnetic quantities. The fundamental quantities are the electric field intensity, E (V/m); the electric flux density, D (C/m²); the magnetic field intensity, H (A/m); the magnetic flux density, B (Wb/m²); the current density, J (A/m²); and the electric charge density, ρ (C/m³).

For general time-varying fields, Maxwell's equations can be written as follows.

$$\nabla \times \vec{H} = \vec{J} + \frac{\partial \vec{D}}{\partial t} \quad (17)$$

$$\nabla \times \vec{E} = -\frac{\partial \vec{B}}{\partial t} \quad (18)$$

$$\nabla \cdot \vec{D} = \rho \quad (19)$$

$$\nabla \cdot \vec{B} = 0. \quad (20)$$

The first two equations, Eqns. 17 and 18, are also referred to as Maxwell-Ampère's law and Faraday's law, respectively. The third and fourth equations, Eqns. 19 and 20, are two forms of Gauss' law, the electric and magnetic forms, respectively. Another fundamental equation is the equation of continuity, which can be written as

$$\nabla \cdot \vec{J} = -\frac{\partial \rho}{\partial t}. \quad (21)$$

Out of the five above-mentioned equations, Eqn. 17 through 21, only three are independent ($\vec{D} = \epsilon \vec{E}$, $\vec{B} = \mu \vec{H}$, and, $\nabla \times \vec{B} = \mu \vec{J}$; where ϵ and μ are the dielectric permittivity and magnetic permeability constants of the medium, respectively). The first two, Eqns. 17 and 18, combined with either the electric form of Gauss' law or the equation of continuity, form such an independent system.

Rectangular Cross-Section Resonant Cavity

Waveguide cavities, a very important class of microwave components, are formed by taking a section of a waveguide and enclosing its front and back faces with conducting plates. A waveguide, in general, means any structure that supports propagation of a wave. The most common types of waveguides are hollow conductive metal pipes used to carry high-frequency radio waves. Metallic waveguide structures differ in their geometry. One common geometry is a rectangular waveguide as demonstrated in Figure 4.

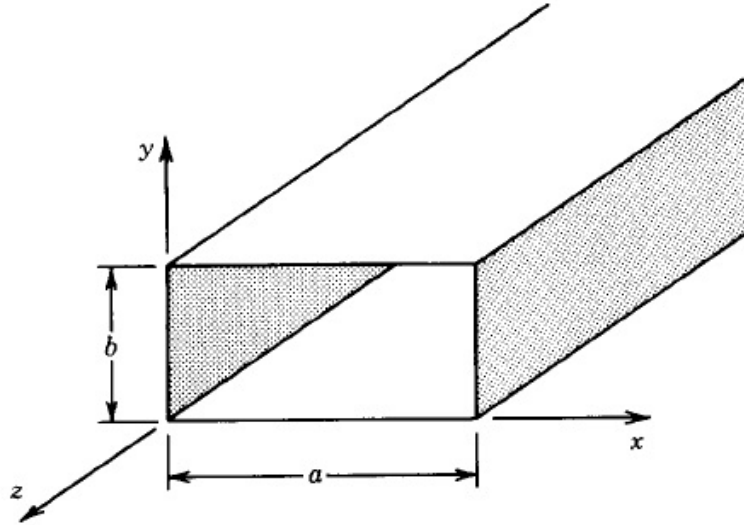


Figure 4 Rectangular waveguide with its dimensions (Balanis, 1989).

Cavity Modes- Resonant cavities can support specific three-dimensional field patterns or modes based on their dimensions and the frequency of the wave. These frequencies are resonant frequencies of the cavity. The field configuration inside a rectangular cavity may be either TE (transverse electric) or TM (transverse magnetic) modes. In the former, the component of the electric field parallel to the longitudinal axis of the cavity is zero, whereas in the latter that of the magnetic field parallel to the waveguide longitudinal axis is zero.

The electric and magnetic field components for a resonant cavity are derived in a manner similar to rectangular waveguide's. However, additional boundary conditions as well as allowing a standing wave pattern (versus a traveling wave pattern) along the length of the waveguide should be considered. The resonant frequency for a TE_{mnp}^z or TM_{mnp}^z mode can be written (Balanis, 1989) as

$$f_{mnp}^{\text{TE/TM}} = \frac{1}{2\pi\sqrt{\mu\epsilon}} \sqrt{\left(\frac{m\pi}{a}\right)^2 + \left(\frac{n\pi}{b}\right)^2 + \left(\frac{p\pi}{c}\right)^2}. \quad (22)$$

Here, f_{mnp} represents the resonant frequency of TE_{mnp}^z or TM_{mnp}^z mode, a , b , and c are the dimensions of the rectangular cavity in X, Y, and Z directions. Finally, m , n , and p are mode numbers representing the number of half wavelength in X, Y, and Z direction, respectively. The possible mode numbers for TE^z and TM^z are

$$\text{for } TE^z: \begin{cases} m = 0, 1, 2, \dots \\ n = 0, 1, 2, \dots \\ p = 1, 2, 3, \dots \end{cases} m = n \neq 0 \quad (23)$$

and

$$\text{for } TM^z: \begin{cases} m = 1, 2, 3, \dots \\ n = 1, 2, 3, \dots \\ p = 0, 1, 2, \dots \end{cases}. \quad (24)$$

The two dimensional cross-sectional field distribution for the first 18 modes of a rectangular waveguide with cross-sectional dimensions $a/b = 2$ are plotted in Figure 5. It is noteworthy that for a resonant cavity, these configurations follow the same analogy.

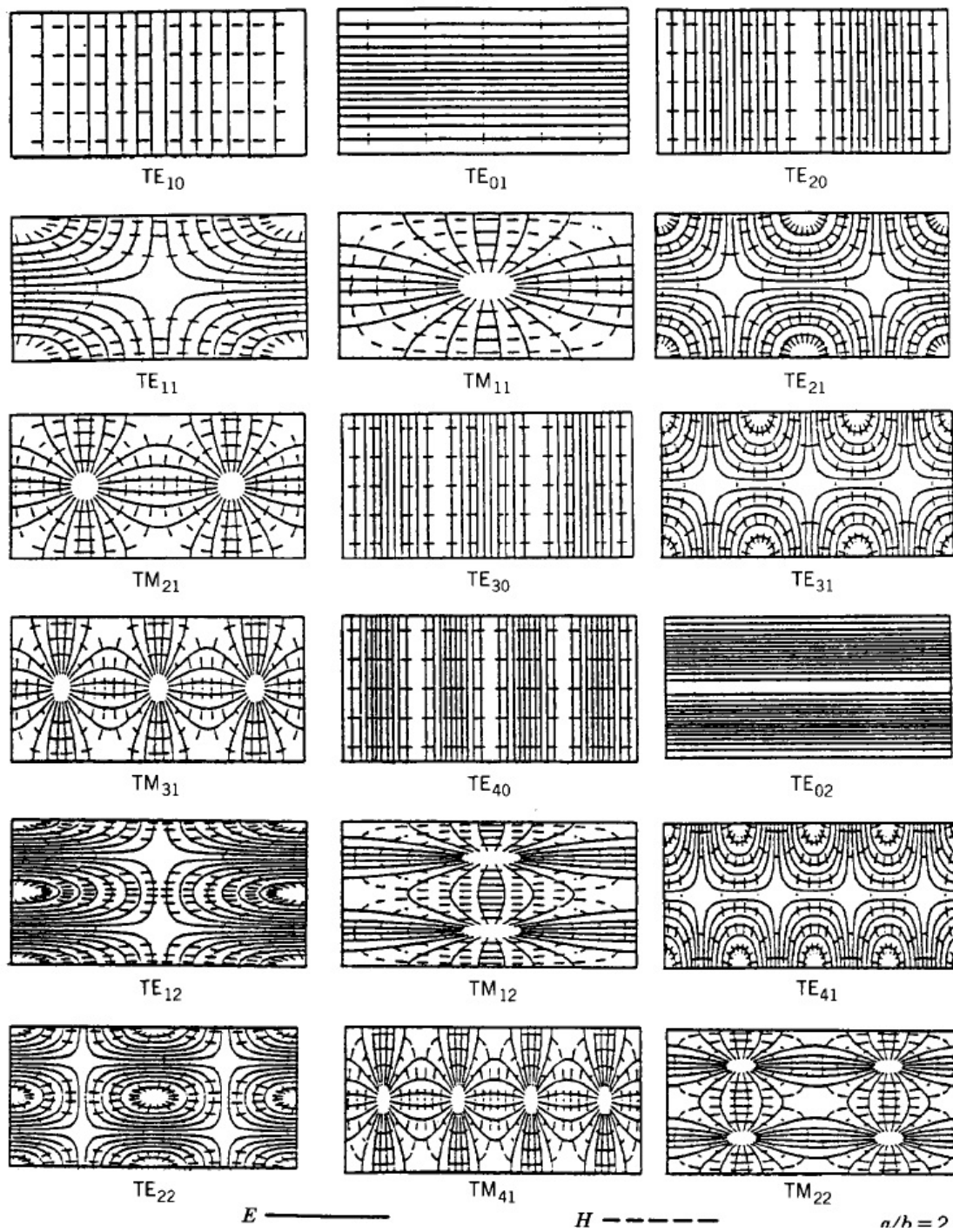


Figure 5 Field patterns for the first 18 TE^z and / or TM^z modes (coordinate axis is shown in Figure 4) in a rectangular waveguide with $a/b = 2$ (Lee et al., 1985).

Quality Factor- An important characteristic of waveguide cavities is their high quality factors,

$$Q = \omega \frac{\text{Stored Energy}}{\text{Dissipated Power}} , \quad (25)$$

where ω is the angular frequency (rad/s). A higher Q indicates a lower rate of energy loss relative to the stored energy. Resonators having higher Q factors resonate with greater amplitudes (at the resonant frequency), but have a smaller range of frequencies around that frequency for which they resonate. With a good approximation, it is also possible to calculate the quality factor by defining $Q = \frac{f_0}{\Delta f}$, where f_0 is the resonant frequency, and Δf is the 3-dB bandwidth or the bandwidth of $\frac{1}{2} E_{\max}$ (Dey and Mirra, 1998). Figure 6 schematically represents this method of calculation of the quality factor.

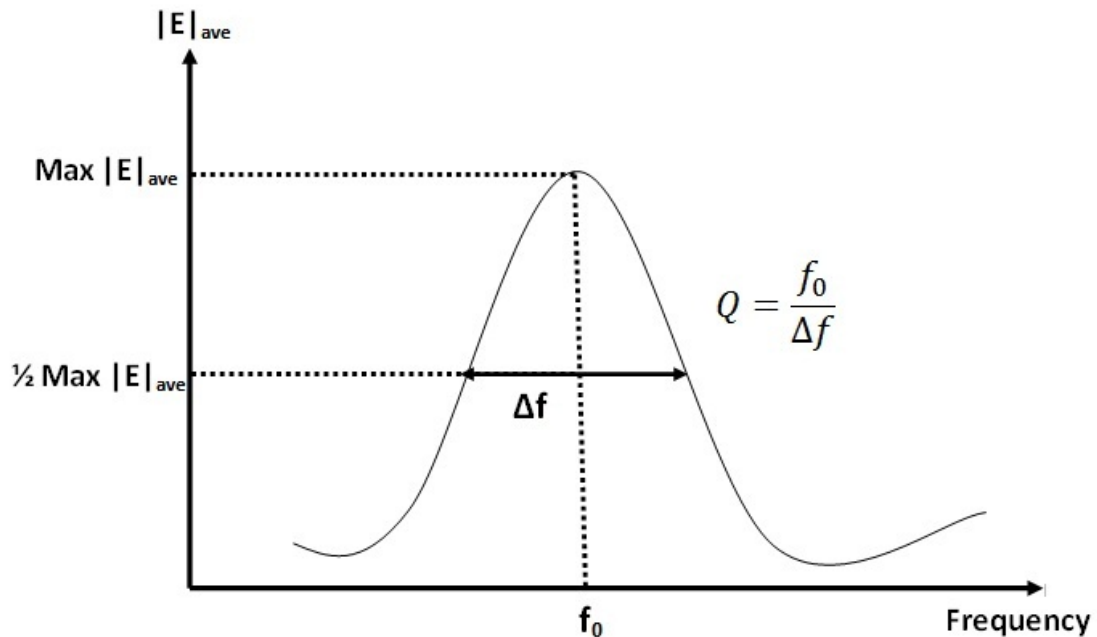


Figure 6 The schematic Q calculation diagram.

Coupling- Whenever a given mode is to be excited, the excitation scheme must maximize the energy exchange between the source and the guide (Balanis, 1989). If the energy exchange is from a transmission line such as a coaxial line to a cavity, two of the popular methods, consistent with the experimental setup of this work, are as follows (Brown et al., 1973).

- **Probe Coupling-** Probe coupling is a linear probe or antenna oriented parallel to the electric field lines in the cavity. The probe should be placed near the maximum of the electric field mode pattern. This is usually referred to as electric field or probe coupling (Figures. 7a and 7b).
- **Loop Coupling-** In this case, a loop antenna oriented in such a way that the plane of the loop is perpendicular to the magnetic field lines. The probe should be placed near the maximum of the magnetic field mode pattern. This is usually referred to as magnetic field or loop coupling (Figures. 7c and 7d).

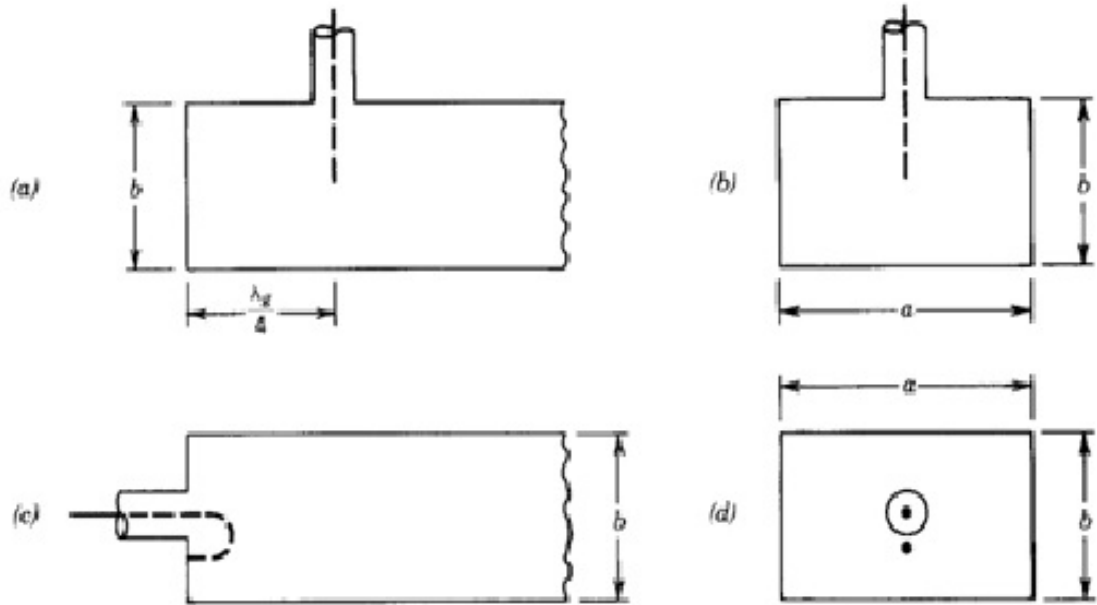


Figure 7 Coaxial transmission line to rectangular waveguide coupling: (a) The side and (b) the end views of a coaxial antenna to a waveguide electric field coupling for TE_{10} mode. (c) The side and (d) the end view for the coaxial antenna to a waveguide magnetic field coupling for TE_{10} modes (Balanis, 1989).

Dielectrophoresis

Dielectrophoresis is a possible mechanism of dye motion from EM stimulation (Sangrey, 2011). Dielectrophoresis is a phenomenon in which particles that are not electrically charged but are in a background medium can experience a force created by an EM electric field gradient. An alternating electric field induces a polarization in particles in the medium, and the particles are subject to a net force from an electric field gradient regardless of their charge. The result of this force is dependent on the electric properties of both the medium and the particle, the size of the particle, and the frequency of the electric field. Although dielectrophoresis is most readily observed for particles with diameters ranging from 1-1000 μm (Mokkapati, 2011), the 1-5 nm dye particles used in this experiment can still be affected. The force that can be exerted by the

dielectrophoresis is dependent on the complex dielectric permittivity of the particle, ϵ_p^* (F/m) and that of the surrounding medium, ϵ_m^* . This relationship for the induced force, \vec{F}_{DEP} (N), is described by

$$\vec{F}_{DEP} = 2\pi r^3 \epsilon_m^* \operatorname{Re} \left\{ \frac{\epsilon_p^* - \epsilon_m^*}{\epsilon_m^*} \right\} \nabla |\vec{E}|^2, \quad (26)$$

where E is the nonuniform EM electric field (V/m), and r is the radius (m) of the homogeneous sphere of the particle molecule with no net charge. This force is proportional to the gradient of the magnitude of the nonuniform electric field squared. When the dielectric permittivity of the particle is higher than that of the medium, the particle will move toward the area of lower electric field intensity. In a case where the dielectric permittivity of the medium is higher than that of the particle, the particle will move against the gradient of the electric field (i.e., toward the area of higher electric field intensity). The effect of dielectrophoresis is frequency-dependent for each medium and particle combination.

Heat Transfer and Convective Flow

The heat equation is an equation that describes the diffusion of heat (or variations in temperature) in a given region over time. For a temperature $u(x, y, z, t)$ as a function of three spatial variables (x, y, z) and the time variable t , the heat equation is

$$\frac{\partial u}{\partial t} = -\nabla \cdot (-\alpha \nabla u), \quad (27)$$

where α is a positive constant (m^2/s) called thermal diffusivity. For a homogeneous, isotropic case, Eqn. 27 turns into

$$\frac{\partial u}{\partial t} = \alpha \left(\frac{\partial^2 u}{\partial x^2} + \frac{\partial^2 u}{\partial y^2} + \frac{\partial^2 u}{\partial z^2} \right). \quad (28)$$

Eqn. 28 states that the rate of change of temperature at a specific location over time is proportional to the spatial Laplacian of the temperature. Based on this equation, if a temperature gradient is applied in a specific location in a medium, the transfer of heat, which can affect the transfer of particles, occurs until the gradient of the heat disappears. This is important for the experiment of diffusion because any possible heat emitted from the antenna body (source of generation of EM waves in the medium) into the surrounding medium should be taken into account in the analysis. Although efforts are made to keep the temperature constant, any little change in temperature might alter the transport mechanism. Therefore, the diffusion equation might need to be coupled with the heat equation and resulting convective flow.

CHAPTER THREE: MATERIALS AND METHODS

This chapter is organized in two sections. In the first section, “Simulation, Digital Analysis and Evaluation,” methods of analysis of the experimental results of the work performed by Sangrey (2011) are explained. The analytical results of this section proved the necessity of a modified experimental setup. Hence, in the second section, “Modified Experimental Setup,” a modified experimental setup is introduced for a more accurate analysis. The simulation of the new experimental setup as well as the method used to analyze the results of the simulation and experimentation are also explained in detail.

Section 1: Simulation, Digital Analysis, and Evaluation

This section describes methods used for the analysis of Sangrey’s experimental results (2011) by the author. However, before describing the simulation details and correlation development and evaluation, the experimental setup of his work is summarized here to provide a clear background for the analysis. For a more detailed description of Sangrey’s setup, refer to Sangrey (2011).

Sangrey’s Experimental Setup

In order to study effects of EM stimulation on diffusion without any temperature change, a nonreactive, inert dye was injected into a water medium to diffuse while the temperature was recorded continually and showed no change. Meanwhile, a number of pictures were taken for later analysis of digital images of the diffusion process. Acquiring images at consistent time intervals (every 1 minute) and using the intensity of the images

to measure the dye concentration enabled the determination of the transport rate. The same procedure was repeated; however, the medium and dye in the test apparatus were stimulated by a CPVC-cased, monopole antenna (an RG8 coaxial cable with 7 cm of the outer conducting shield stripped) placed at the center of the box, submerged in the medium. The stimulation was repeated for different magnitudes of power: 10, 30, and 50 W, to find a possible correlation between the power magnitude and dye diffusion. At each run of the experiment, the electric field component of the EM waves was measured and mapped on specific depth (vertical) slices for a better understanding of the relationship between the diffusion and EM stimulation (since the electric field magnitude is expected to be the possible controlling factor). An RF coaxial probe was used to measure one component of the RF electric field. For this reason, it is essential to simulate the experiment to obtain the three components of the electric field as well as a 3D visualization of the variation of the electric field.

It is noteworthy that in order to isolate the experimental setup from the surrounding environment and to prevent interference from outside the experiment, the entire system —the water-filled acrylic box, the radiating antenna, and the injection equipment— was placed in a Faraday cage made of aluminum mesh. Figure 8 shows the experimental setup configured for the electric field mapping.

Unstimulated Tests- The unstimulated diffusion is horizontally symmetric around the injection area. The dye descends vertically from the injection table and spreads in all directions along the bottom of the tank and up the sides. Figure 9 shows an example of pictures captured during the unstimulated diffusion test, which confirms no preference in the flow of the dye toward the left or right side of the box.

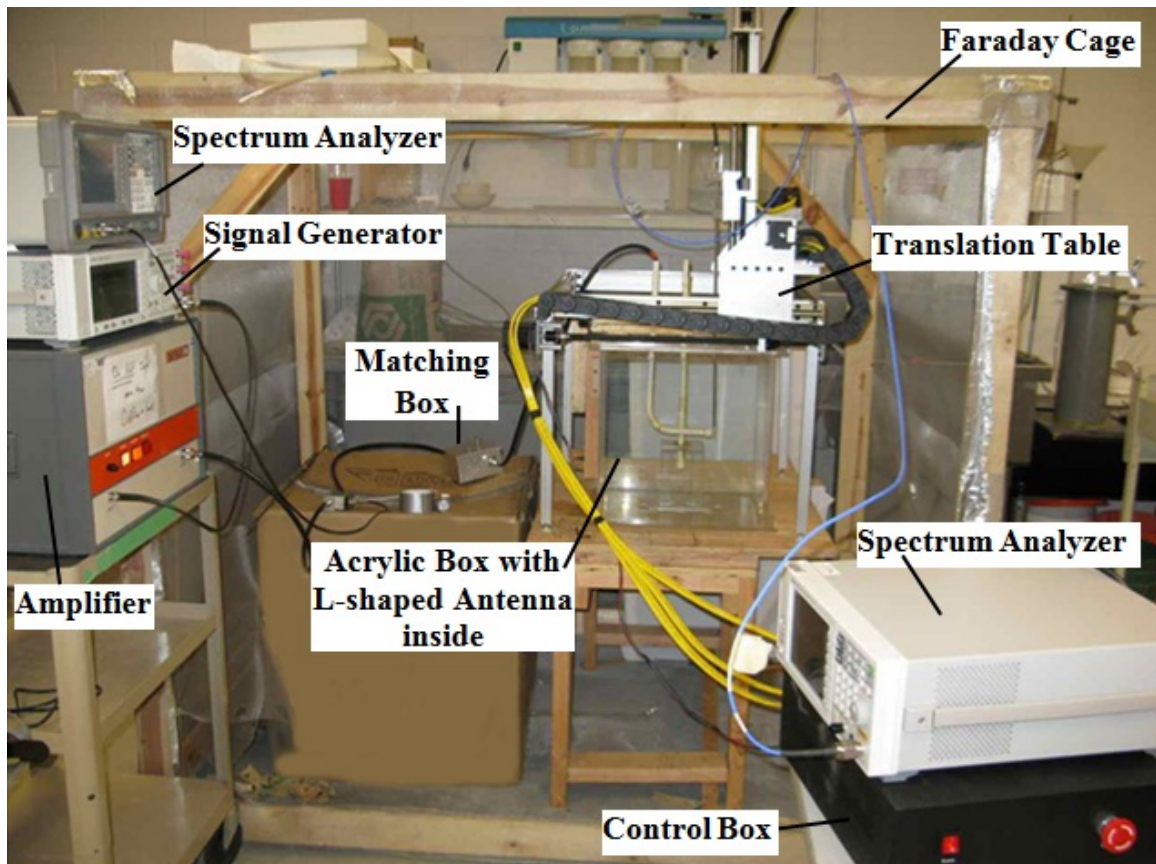


Figure 8 Sangrey's setup (2011) and experimental setup for EM-stimulated tests.

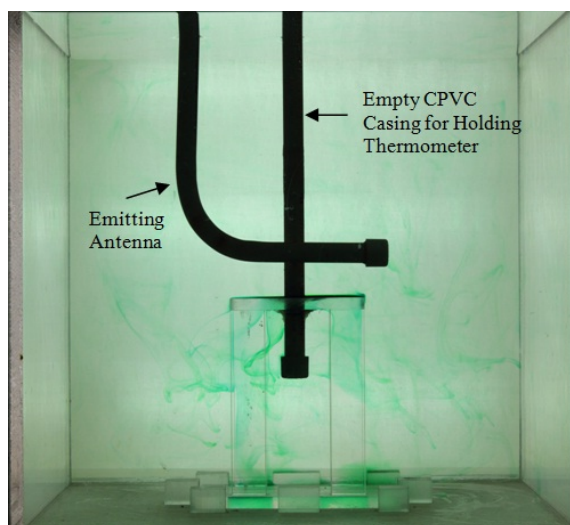


Figure 9 Random dye movement during the unstimulated test.

For analysis, even though the problem is three-dimensional, the intensity of each pixel of the 2D (two-dimensional) image correlates to the integral of the concentration of the dye along the line of sight corresponding to the pixel. Hence, the results are analyzed as 2D images. The camera is placed at a distance far enough from the test box to ensure that lines of sight for the central region (away from boundaries) of the box are relatively parallel. A series of calibration experiments were performed using the same lighting setup to calibrate the pixel intensity of the 2D images to the integral of dye concentration along the corresponding pixel. Ten pictures of the background were captured and averaged. The average background was subtracted from all other images to eliminate the background, box, injection table, and antenna to leave only the diffusing dye.

The results of the digital pixel analysis provide a matrix of concentrations of the dye corresponding to different nodes in the medium at different times. Figure 10 shows the locations of 208 nodes in the test medium where the dye intensity was studied at 130 time intervals (1 minute apart). The nodes are spaced every 2 cm, and images are saved at 1-minute intervals. After calibration, the result is a matrix of 208×130 dye concentrations for these nodes where 208 (16×13) refers to the total number of nodes and 130 refers to the captured times. Note that the same procedure is used for the EM-stimulated tests as well.

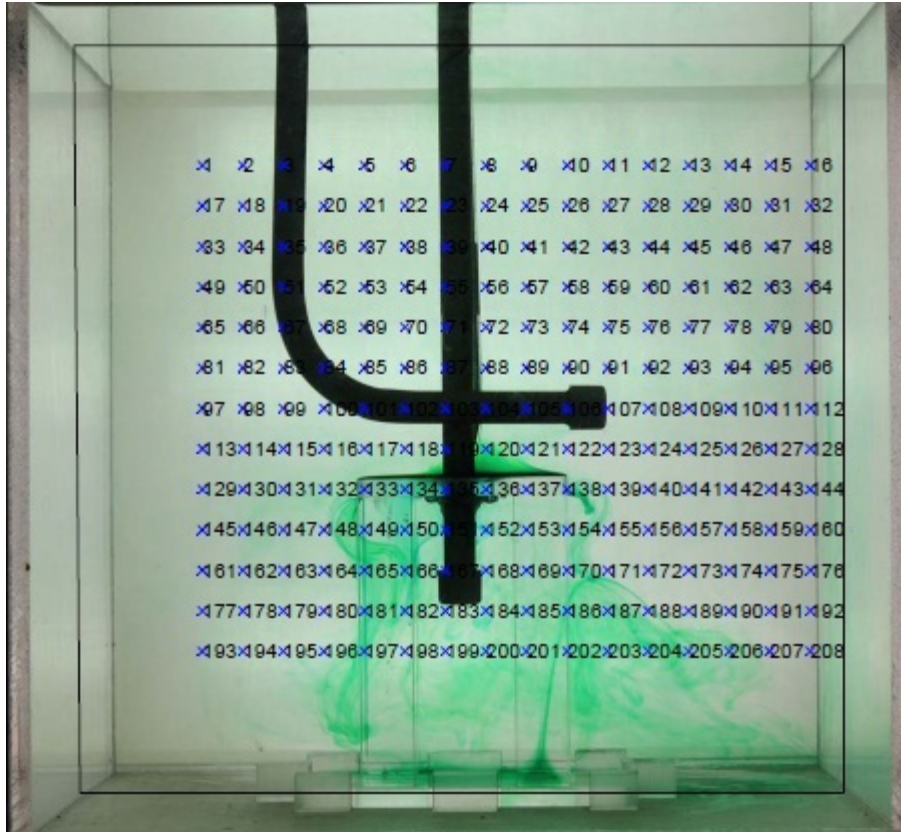


Figure 10 Locations of the 208 nodes used in digital pixel analysis.

EM-Stimulated Tests- When the medium is stimulated by a horizontally-polarized L-shaped antenna and after the dye descends from the injection table, the diffusing dye moves to the right of the testing medium with very little dye diffusing to the left. This effect is in contrast to the unstimulated case. It is noteworthy that no measurable temperature change was recorded. The diffusion pattern shows the clear effect of the EM stimulation and the radiation pattern of the antenna on the diffusion of the dye in water. Figure 11 demonstrates an example of an EM-stimulated transfer mechanism where the concentration of the dye at the right side of the testing box is larger than that of the left side. The EM-stimulated tests used for these data consist of two runs each at powers of 0, 10, 30, and 50 W.

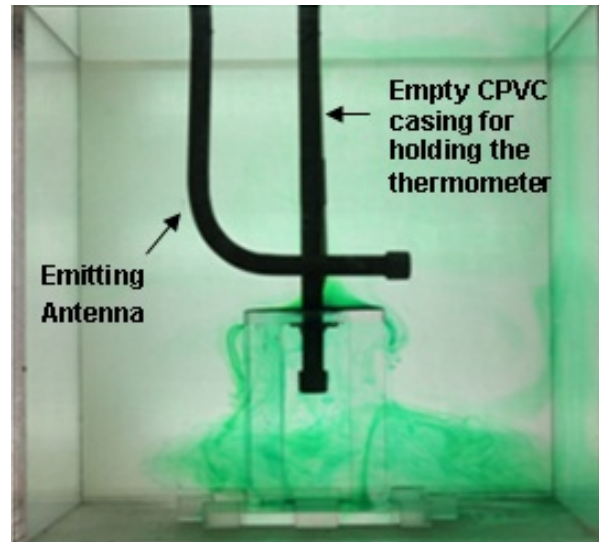


Figure 11 Dye flow during the stimulated test with a larger concentration toward the right side of the medium.

Computational code was developed using MATLAB software to compare and quantify the relative dye transport. The program integrates the amount of dye in different zones of the medium. The five zones that are used for comparison to determine the effect of EM stimulation are shown in Figure 12. Because the dye moved toward the right side of the testing box during EM stimulation and had no apparent preferred path during unstimulated tests, Zones 2 and 4 are compared and contrasted. Zones 1 and 5 had compounded errors because of reflections at the water acrylic interface (i.e., left and right walls of the acrylic box) in the box at the imaging angle.

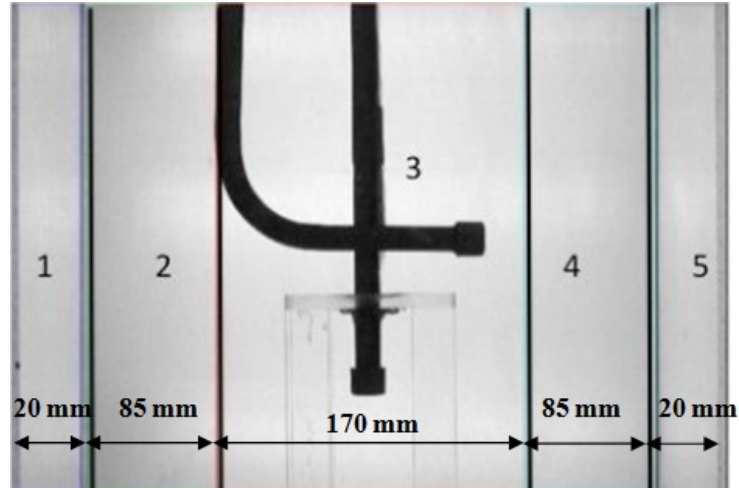


Figure 12 Zones 1 through 5 used for image analysis (Sangrey, 2011).

The average dye concentrations from Zones 2 and 4 are plotted in Figures 13 through 16. Figures 13 through 16 show the blue concentration of the three-color (i.e., red, green, and blue) spectra of digital images. The same trend was also seen in the same graphs for the red concentration. In Figure 13, the Zone 2 concentration, 50W-Z2R1, diverges from the Zone 4 concentration, 50W-Z4R1. 50W-Z4R1 is a notation for the 50 W, EM-stimulated test, Zone 4 (as shown in Figure 12), and 1 indicates that this was the first run out of 2 duplicate tests performed for the 50 W EM stimulation. The tests shown in Figures 13 through 16 are all of the same imaging zones (i.e., Zones 2 and 4), during EM stimulation of 50 W, 30 W, 10 W, and 0 W at a frequency of 154 MHz.

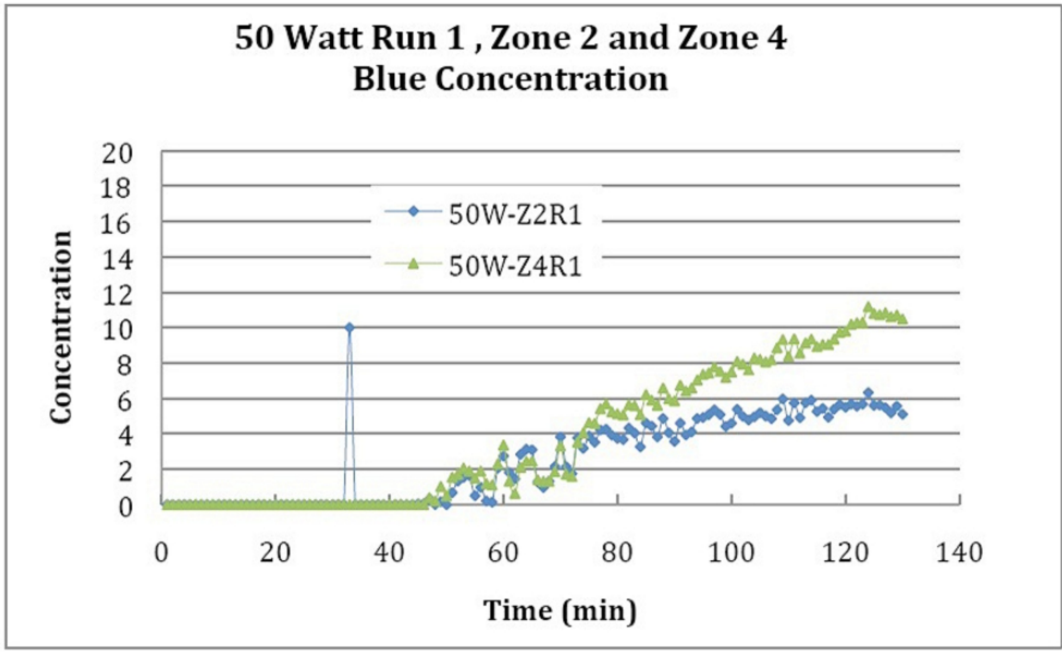


Figure 13 Zones 4 and 2, diverging concentrations of 50W EM-stimulated test. The spike at 33 minute indicates the start of stimulation (Sangrey, 2011).

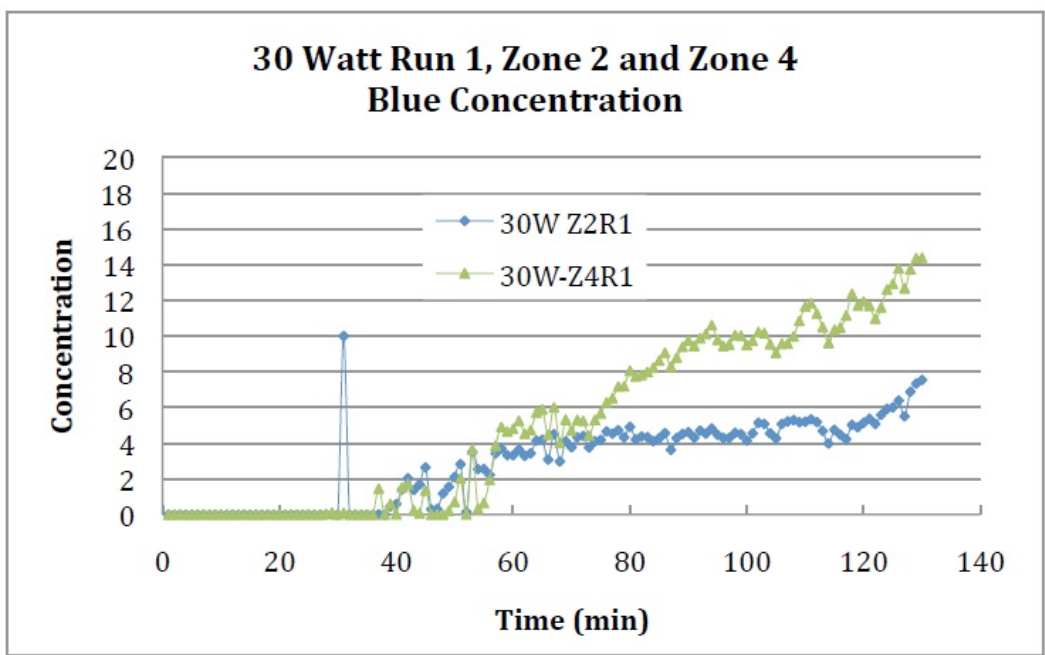


Figure 14 Zones 4 and 2, diverging concentrations in 30-W EM-stimulated test. The spike at 33 minute indicates the start of stimulation (Sangrey, 2011).

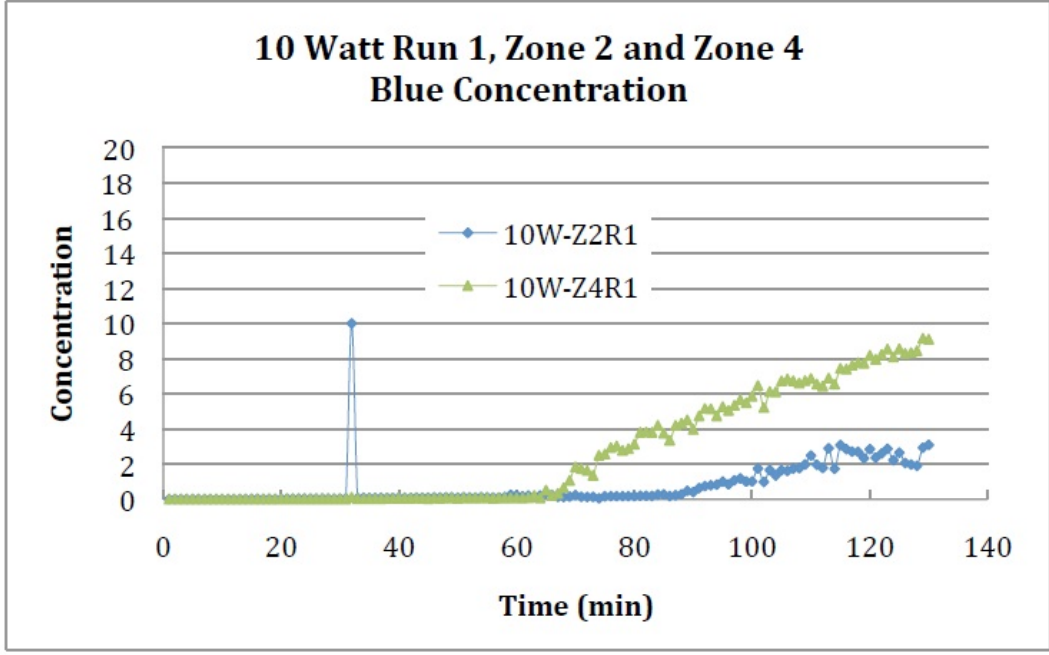


Figure 15 Zones 4 and 2, diverging concentrations in 10-W EM-stimulated test. The spike at 33 minute indicates the start of stimulation (Sangrey, 2011).

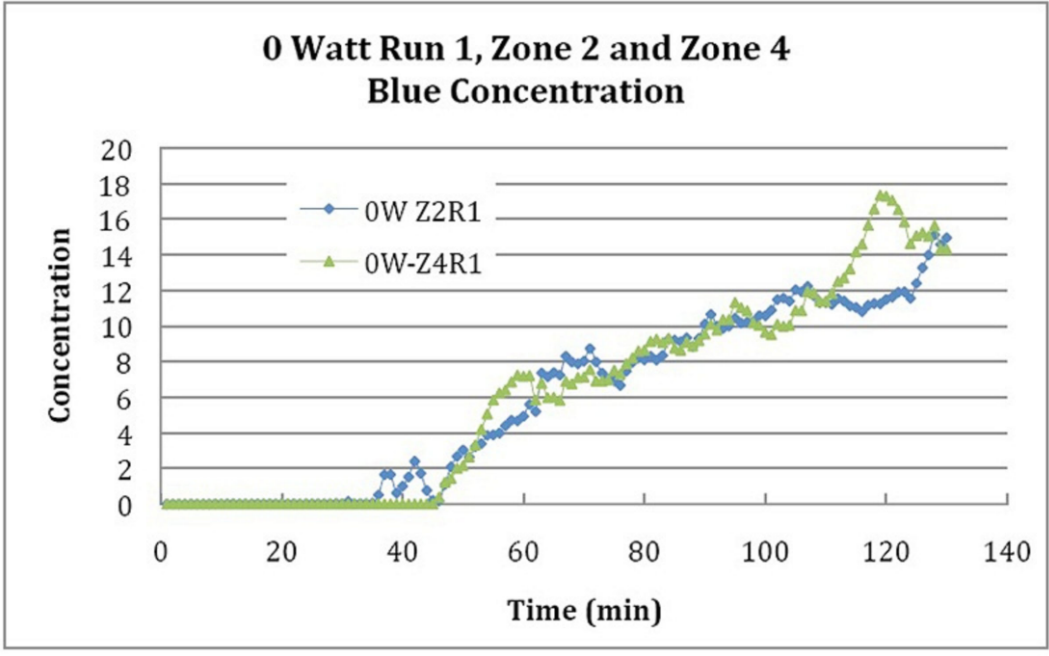


Figure 16 Zones 4 and 2, diverging concentrations in unstimulated test (Sangrey, 2011).

In Figures 13 through 16, tests start unstimulated, and then EM stimulation starts after about 30 minutes. As seen in Figure 16, the concentration in Zones 2 and 4 of the unstimulated plot shows an increase at a similar rate throughout the test. Figure 16 (i.e., unstimulated case) shows that the dye concentrations in Zones 2 and 4 rise together, diverging little other than the noise due to temporary differences from dye fingering. The slope of the plot of concentration versus time is representative of the rate of increase in concentration in a given zone and, therefore, is proportional to the rate of transport (flux) of the dye in that direction. Using a linear trend-line function, the slope of the concentration plot is found. The slope is only measured after the 60th-minute mark to eliminate the artificial marking spike indicating the start of EM-stimulation and the long flat portion of the curve associated with the unstimulated period. An example of the trend lines used for analysis is shown in Figure 17. The rate of dye transport into Zone 4 versus the input RF power is plotted in Figure 18. Although the results are consistent for each power at all tests, they do not have a trend from which a relationship between the diffusion rate and power can be determined. The same result is seen for Zone 2 as well.

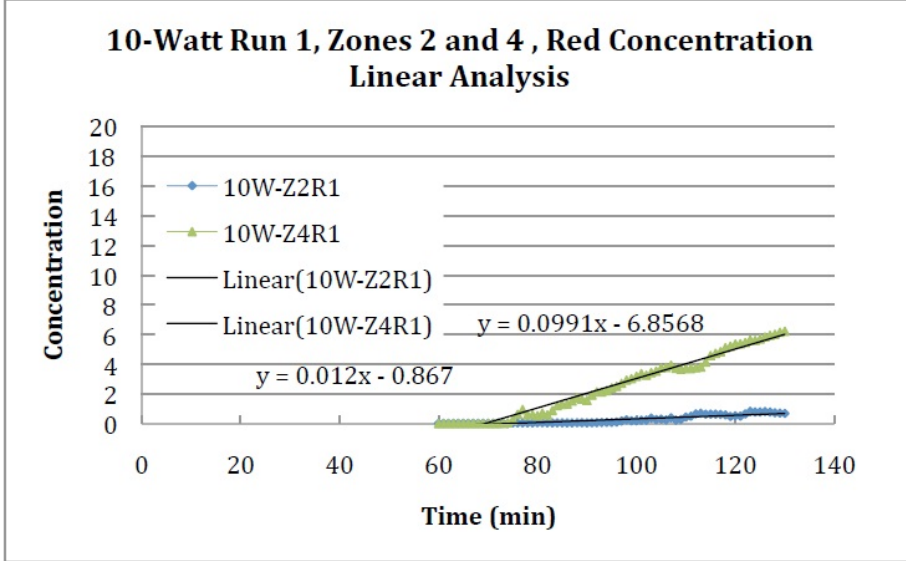


Figure 17 Linear fit-lines to concentration increases (Sangrey, 2011).

The results of Sangrey’s work (2011) qualitatively proved the effect of EM-waves on transport mechanisms. However, to investigate the effect of the electric field magnitude on the transport mechanism, a full vector of the electric field is required. As a result, this work attempts to provide a full expression of the electric field by simulation of the experiment, which is described in the following.

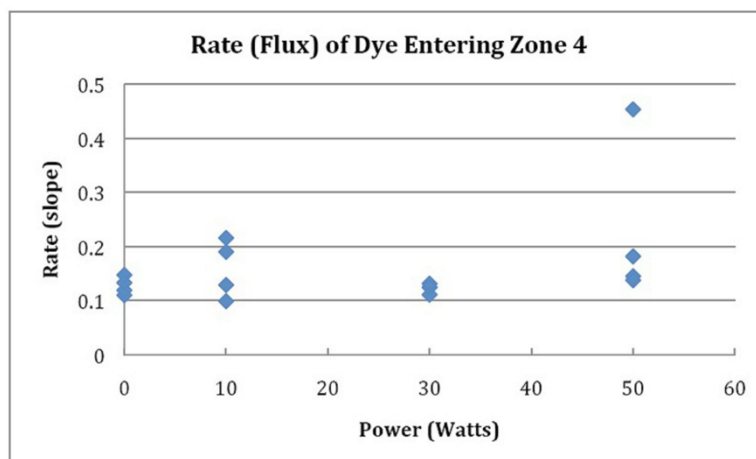


Figure 18 Rate (a representative of flux) of dye entering Zone 4 based on slopes of concentrations (Sangrey, 2011).

Simulation

As mentioned previously, the experimental field measurement could only provide the value dominated by the vertical component of the electric field. For a complex, full vector, 3D visualization of the electric field, the Faraday cage, the water-filled acrylic box and the coaxial antenna (Figure 19) are modeled by the author using the finite element software, COMSOL Multiphysics 4.1. The RF module of COMSOL Multiphysics was used to model the electromagnetic field developed in the medium by the coaxial antenna. It should be mentioned that this model was only used to enable the visualization of the EM field without simulating the diffusion of the dye inside the water.

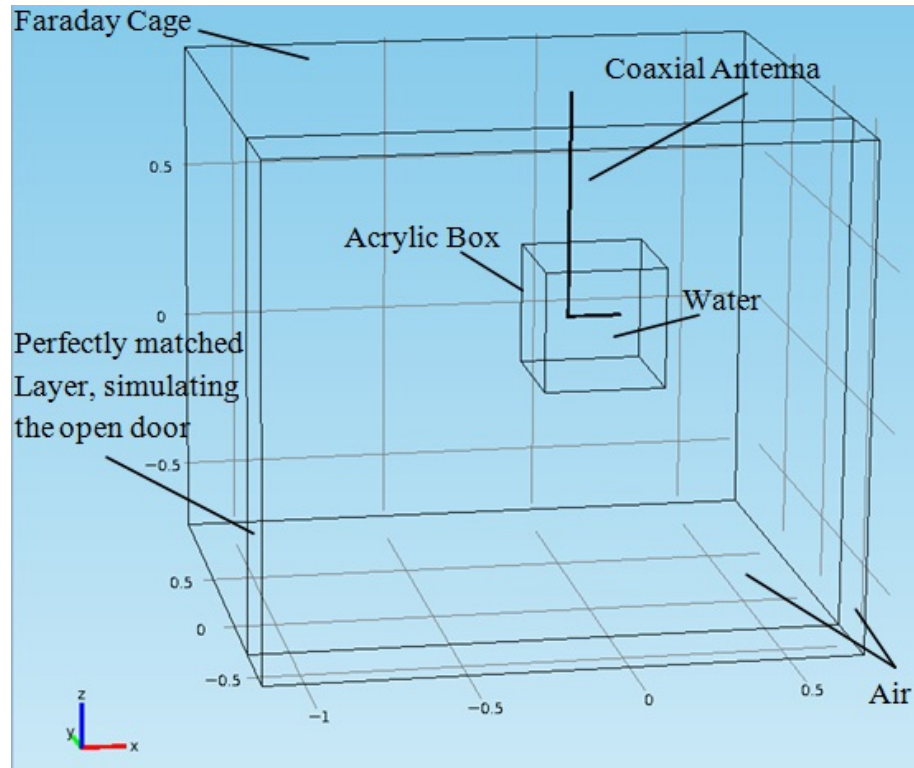


Figure 19 Simulated model for Sangrey's setup.

The acrylic box filled with deionized water, the coaxial antenna as a source of EM wave, and the Faraday cage are simulated as described in detail in Appendix A. In order to avoid the complexity of modeling a curvature, the L-shaped antenna is modeled as two perpendicular narrow cylinders. This is feasible because the coaxial port is modeled in the horizontal part of the L-shaped antenna. The body of the antenna beyond the port (from the port toward the top boundary of the Faraday cage) is merely modeled to represent the metal domain of the antenna, which affects the field. The antenna is long enough to pass through the top edge of the Faraday cage to represent the extension of the cable in the experiment. Figure 20a illustrates the structure of the antenna used in the experiment while Figure 20b shows this structure as simulated in COMSOL Multiphysics.

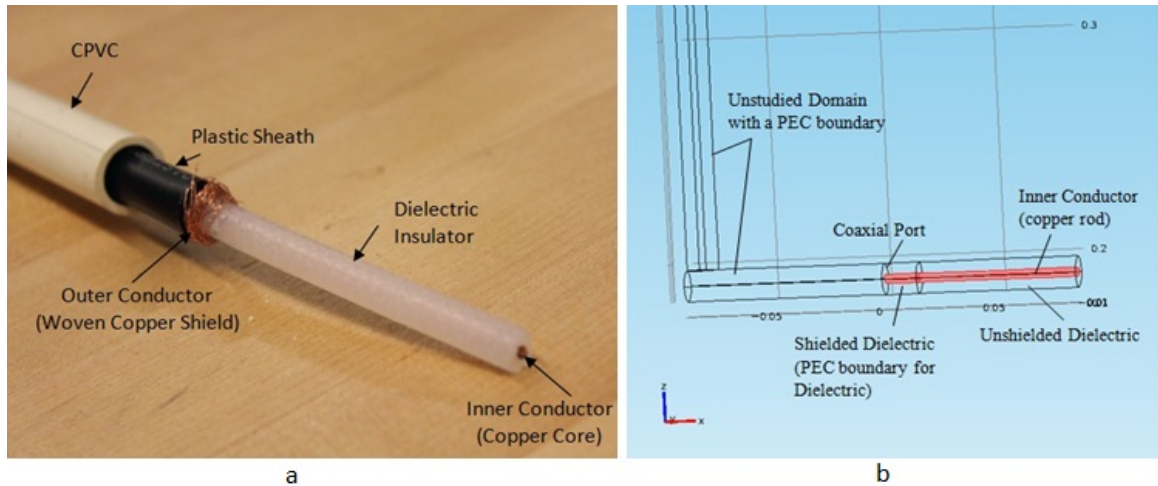


Figure 20 a) Coaxial antenna structure used in experiment, b) Coaxial antenna structure detail simulated in COMSOL Multiphysics.

The simulation of the antenna requires several considerations listed below.

- The inner conductor is modeled as a copper rod whereas the outer conductor is modeled as a PEC (Perfect Electric Conductor) boundary of the dielectric domain surrounding the inner conductor.
- The excitation is simulated by defining a coaxial port with an active excitation. The port is located within the horizontal part of the L-shaped antenna, 2 cm away from the beginning point of exposing the outer conductor of the antenna.
- In order to reduce the cost of modeling, a large portion of the antenna body is deselected from the analysis. The boundaries of the body of the antenna are modeled as PECs to represent the outer conductor of the antenna (since it affects the field), but no calculation was performed within this body.

After the geometry of the experimental setup is modeled, the model can be studied at different frequencies of interest. Using the frequency of 154 MHz as in the

experiment, the electromagnetic field is computed in COMSOL Multiphysics. The software enables the visualization of the EM wave components (electric and magnetic fields) at any node within the studied domain. The results of the simulated electric field and the comparison of these results with that of the experiment, as provided in Sangrey's (2011) work, are summarized in the next chapter.

Digital Analysis and Evaluations

The analysis of the digital pictures from Sangrey's (2011) work results in several matrices, each corresponding to the concentration of the dye at different locations and times for various performed tests. This section involves various methods to find the correlation between the concentration obtained from digital analysis and the electric field/power.

Investigation of Magnitude of Electric Field on Concentration- One approach to find the correlation of the concentration and the electric field is to use the electric field contour map. Observing the change in the concentrations of nodes along any contour line of the electric field map and comparing them to nodes on a line normal to the same contour line can be used to reveal the effects of the electric field magnitude. If the concentration is related to the electric field intensity, the change of concentrations over time of nodes along an electric field contour line should be different from the nodes normal to that contour-line. For this purpose, the following tasks are performed.

Several sets of nodes are selected based on their locations with respect to the electric field's contour map. Each set includes four groups of nodes: two along a contour line of the field map and the other two perpendicular to the contour line. The decision was made to select nodes that are away from the boundaries or noisy areas. Figure 21

shows a schematic of group nodes selected for this study. Grouped nodes “a” and “d” are along a contour line, but grouped nodes “b” and “c” are perpendicular to the same contour line. The reason behind selecting groups of nodes rather than individual nodes is the fact that viscous fingering produces high fluctuations of concentration for individual nodes and does not allow this study.

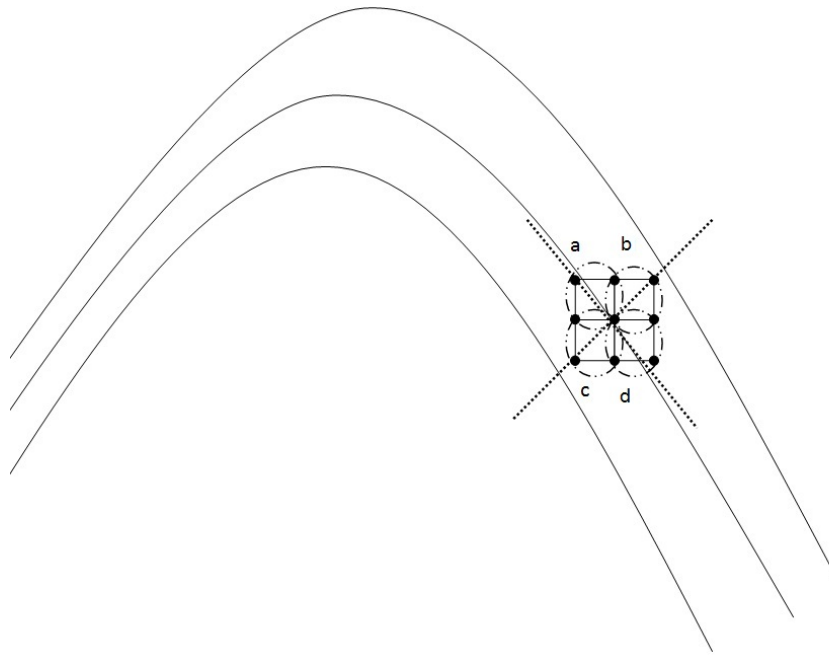


Figure 21 Nodes selected for digital analysis with grouped nodes “a” and “d” along a contour line, and group nodes “b” and “c” perpendicular to the contour line.

The change of the concentration of these grouped nodes is studied over time. If the magnitude of the electric field affected the transport, the change of concentration of grouped nodes along a contour line would show the same trend. This trend should be different for grouped nodes perpendicular to the contour line. This is because of the fact that the nodes along a contour line are experiencing the same electric field magnitude.

Investigation of Power Level on Transport Rate- In order to investigate the effect of power magnitude on the transport flux, a study on the diffusion coefficient is performed. Even though the problem is three-dimensional, the intensity of each image pixel correlates to the integral of the concentration of the dye along the line of sight corresponding to the pixel because the results are analyzed as 2D images.

A finite difference (FD) code was developed in MATLAB to calculate the diffusion coefficient based on Fick's second law (see Appendix C). Fick's second law for a homogenous, isotropic medium (i.e., $D_y = D_z = D$ and is spatially constant) relates the temporal changes of concentration to the divergence of the diffusive flux of concentration. A 2D representation of Fick's second law is described by

$$\frac{\partial C}{\partial t} = D \left[\frac{\partial^2 C}{\partial x^2} + \frac{\partial^2 C}{\partial z^2} \right], \quad (29)$$

where C is the concentration (g/m^3), t is the time (s), D is the diffusion coefficient (m^2/s), and x and z are coordinates (in meters) shown in Figure 19. Using an implicit, forward difference in time and a central difference in space for a stable result for the D value, Eqn. 29 can be discretized,

$$\frac{C_{y,z}^{m+1} - C_{y,z}^m}{dt} = D \left[\frac{C_{y-1,z}^m - 2C_{y,z}^m + C_{y+1,z}^m}{(dy)^2} + \frac{C_{y,z-1}^m - 2C_{y,z}^m + C_{y,z+1}^m}{(dz)^2} \right]. \quad (30)$$

The results of the digital analysis have provided the concentration of different nodes at different times. It is noteworthy that the homogeneity assumption may not be valid even in a homogeneous unstimulated media when a nonuniform EM field is applied. However, for the purpose of this preliminary work and only where fingers do not

occur, the homogeneity and isotropy assumptions are made. Because of the approximation of homogeneity and isotropy, D can readily be calculated for each node, and the system of equations does not need to be solved simultaneously. Based on this equation, a matrix is produced giving the diffusion coefficient for 154 nodes (D was not calculated for boundary nodes) at 129 time intervals (time zero is excluded).

This approach is a preliminary step to estimate D and not a full diffusion and convection analysis at this stage. The results of this approach would not lead to equivalent values of the diffusion coefficient (due to the existence of viscous fingers), but to a representation of the rate of transport where no finger exists. The calculated D values for different tests with different power magnitudes are presented and discussed in the next chapter.

Section 2: Improved Experimental Setup

Sangrey's (2011) experimental setup successfully proved the effect of EM waves on diffusion. The results showed that EM waves direct the transport according to the antenna design. However, to examine the effect of the electric field on the flow, a more organized electric field pattern was required. Although the vertical component of the electric field was mapped carefully using the translation table outside the lossy water-filled medium, the existence of the translation table close to the medium during the electric field probing of Sangrey's experiment might have affected the measurements (refer to Figure 8). The fact that this structure is built of metal elements could change the field pattern during the measurements. Therefore, the measured electric field would be different from the exact electric field inside the medium. This interference is discussed more in the next chapter.

To ensure that the electric field is not distorted due to the surrounding medium and to provide a monotonically changing electric field contour plot, a modified setup is prepared. A resonant cavity is designed to provide a specific field pattern that is desirable for this study. In addition, using the new setup would help to avoid any interference from the surrounding medium (because the metal boundaries of the resonant cavity contains the entire medium); even the translation table is placed outside the cavity during the measurements.

The experimental setup consists of the following material and equipment.

- A 40cm × 40cm × 40cm acrylic box for containing the water.
- A 38cm × 38cm × 38cm RF resonant cavity that is placed inside the acrylic box (Figure 22).

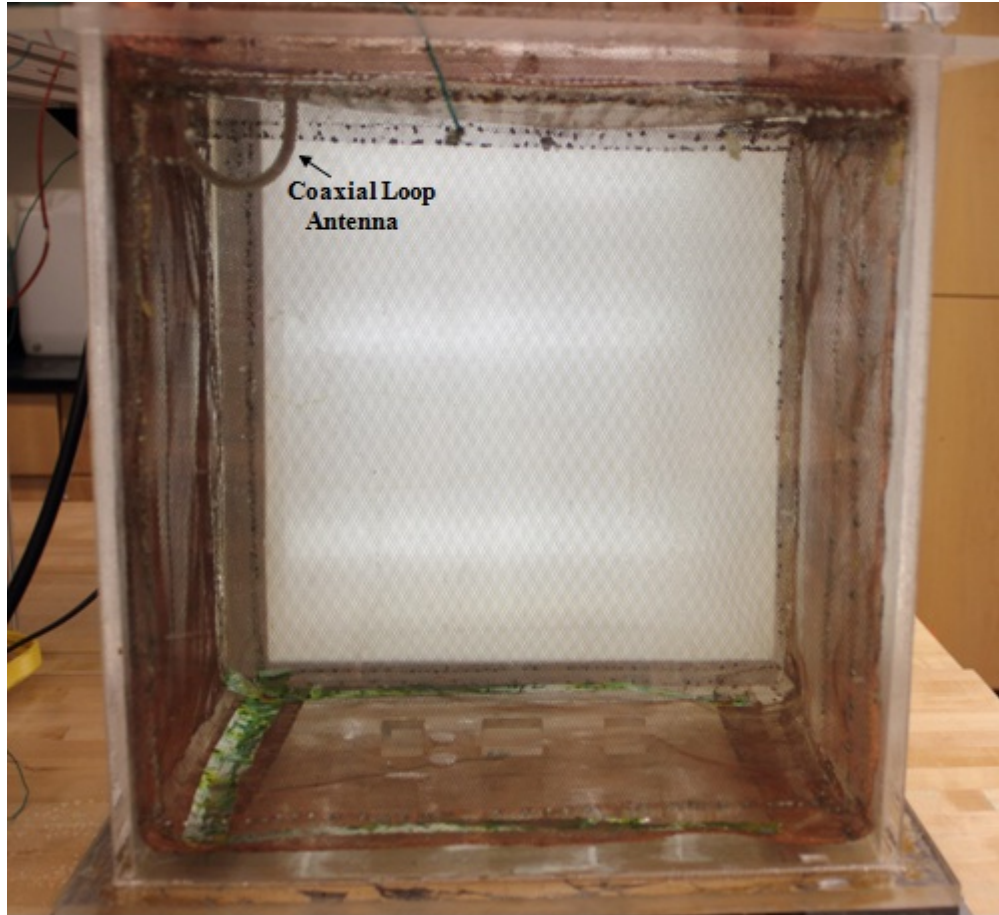


Figure 22 Resonant cavity inside the acrylic box, bottom and sides of the resonant cavity are made of copper mesh to enable visualization but the top is from a copper plate to provide a closed resonant cavity.

- A coaxial loop antenna connected to the EM source to launch EM waves into the medium (shown in upper left side of Figure 22).
- Box filled with deionized, deaerated water.
- Inert, nonreactive, water-based dye.
- A plastic cup glued to an acrylic pedestal to allow the injection of the dye close to the center of the medium (Figure 23).

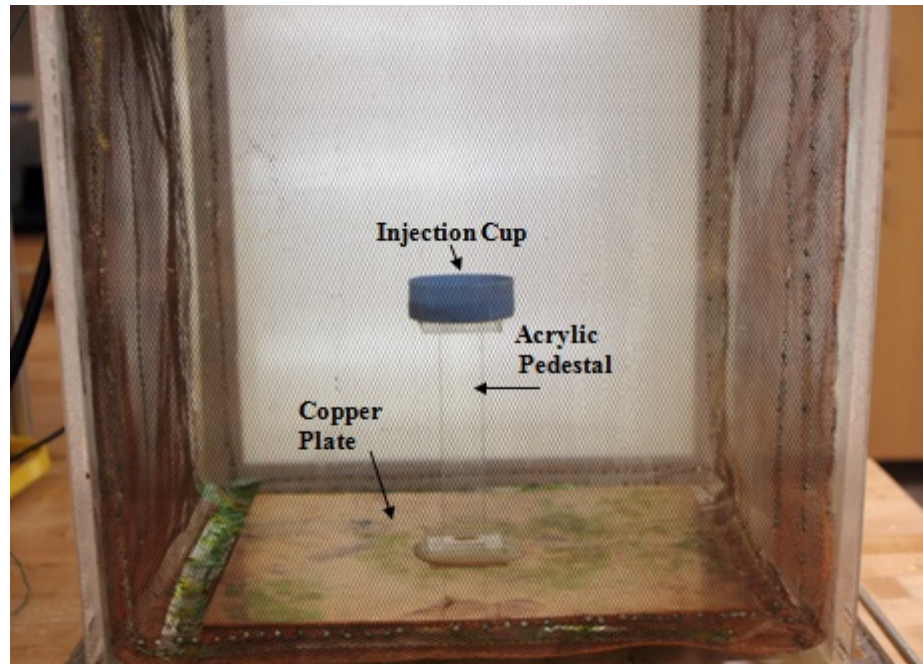


Figure 23 Injection cup on acrylic pedestal attached to a copper plate to hold the dye after injection.

- A digital camera to record the transport process of the dye inside the water.
- A light box to ensure a consistent lighting condition during imaging.
- An RF coaxial probe connected to a 3D computer-controlled translation table to measure the RF electric field inside the medium.

The new setup is simulated in COMSOL Multiphysics in the same manner that Sangrey's work was simulated. The choice of the applied frequency for the resonant cavity of the improved setup is based on the validation of the simulated electric field. The electric field is experimentally measured on different slices for various frequencies (close to the mode frequencies of the resonant cavity) in the range of 50-200 MHz. Lower values of frequency are preferred to create less variation in the electric field within the medium. A contour map of the electric field is prepared for each of the slices at each frequency. At the same time, the simulated model is studied at the same frequency, and

the vertical component of the electric field is compared with the experimentally measured one. The process is repeated for several frequencies until the two contour maps (experimental and simulated) resulted in the same pattern. Performing the process for several frequencies, the best experimentally validated simulation resulted at a frequency of 65 MHz. At this frequency, the measured electric field patterns on different slices closely—but not exactly—match the corresponding simulated field patterns for E_z . Figure 24 shows the measured and simulated contour maps for several slices at this frequency.

Because of the fact that the measuring probe is polarized (placed) vertically, E_z is the dominant component that is experimentally measured and is used for comparison with the simulated results. For the isotropic medium within a resonant cavity, if the E_z component of the simulated and measured electric fields match, the other components are assumed to match as well. This assumption was used because of the lack of required instruments (such as a 3D electric field measuring probe) to measure the full electric field inside the medium. As a result, the simulated full 3D, vector, electric field is used for further analysis.

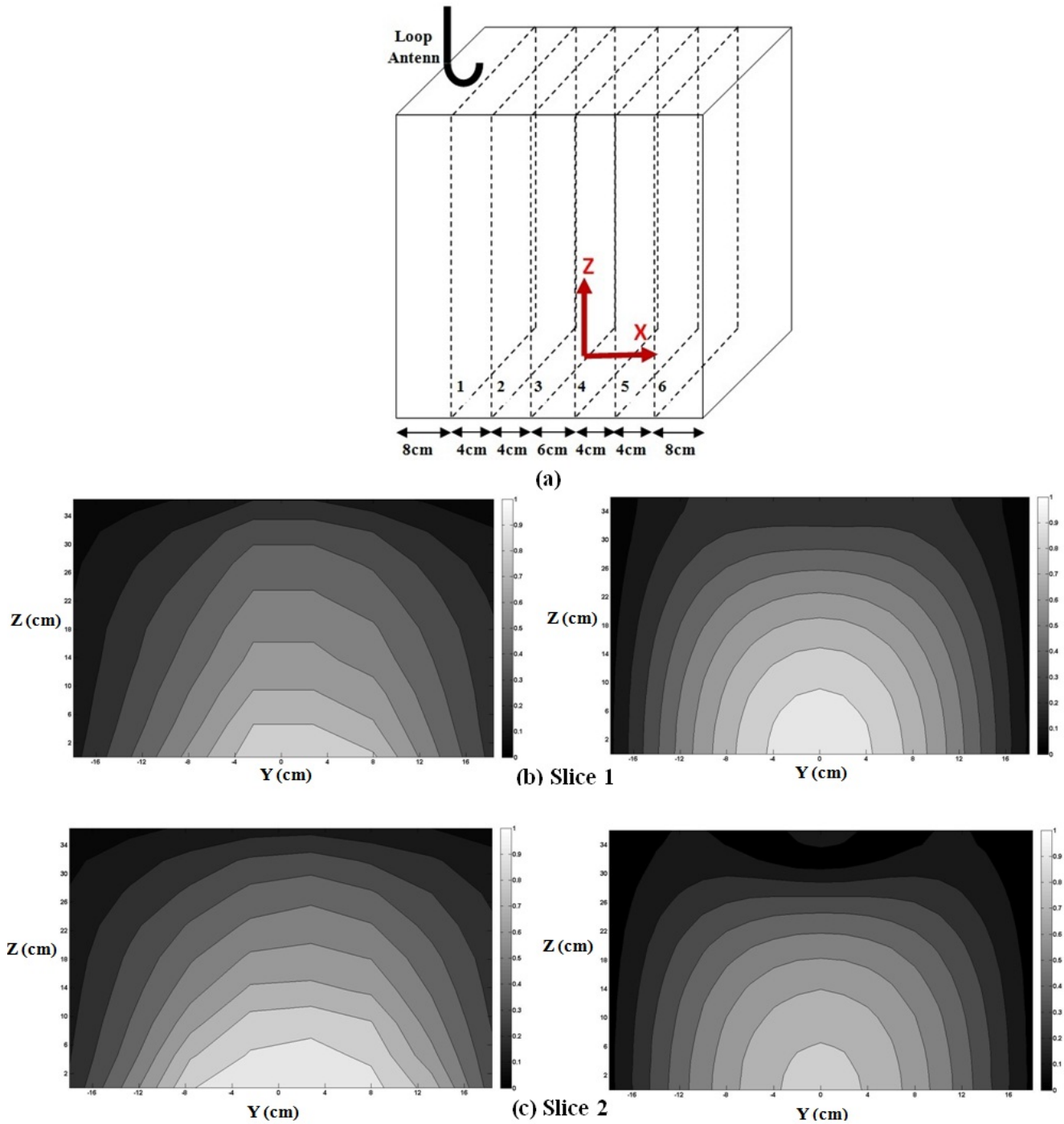


Figure 24 Depth (vertical, YZ) slice normalized electric field map of experimentally measured (left) and simulated in COMSOL Multiphysics (right), a) Schematic of locations of depth slices, b) Slice 1, c) Slice 2.

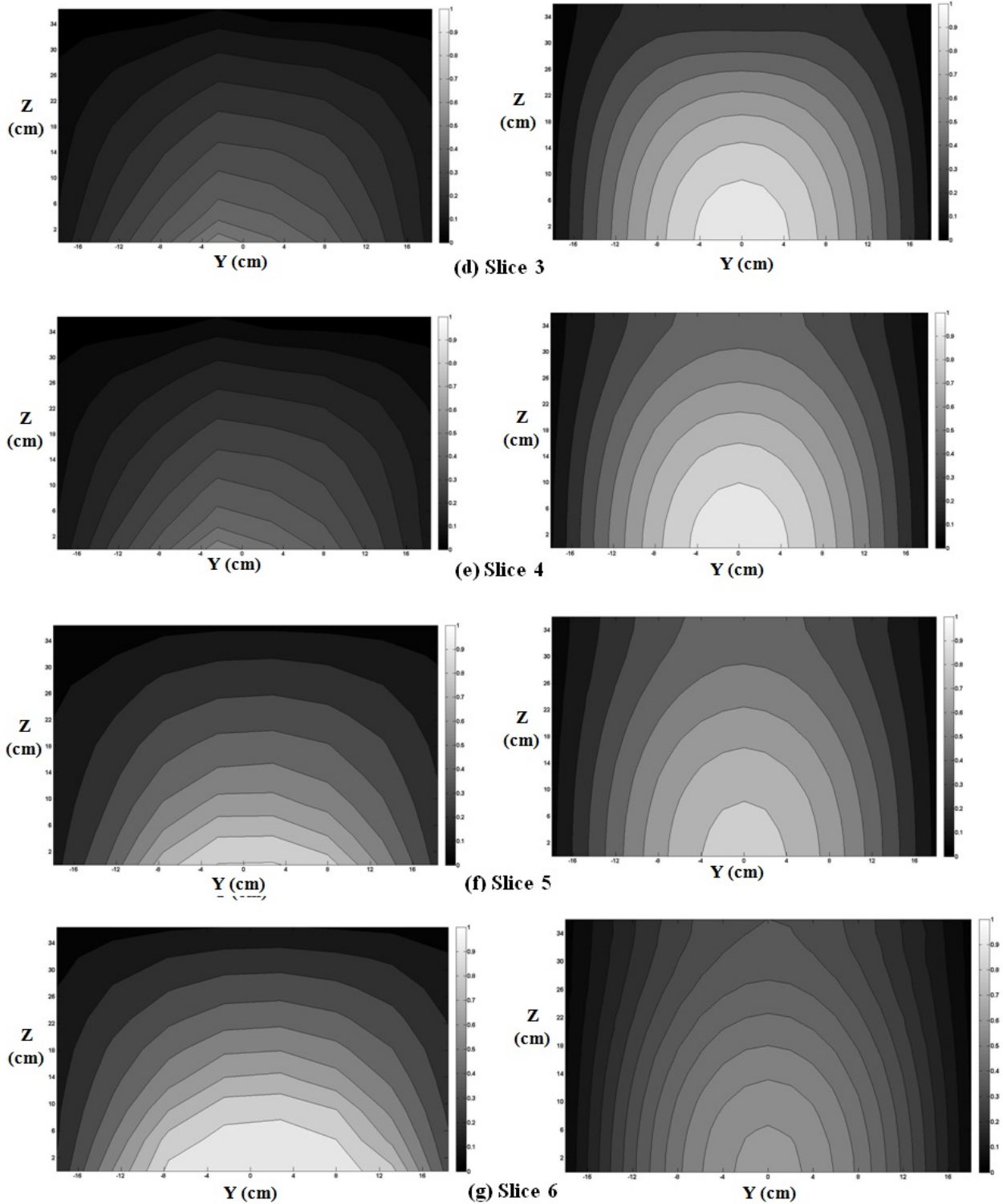


Figure 24 (Cont.) Depth (vertical, YZ) slice normalized electric field map of experimentally measured (left) and simulated in COMSOL Multiphysics (right), a) Schematic of locations of depth slices, d) Slice 3, e) Slice 4, f) Slice 5, and g) Slice 6.

Experiment Procedure- The deionized and deaerated water is used to fill the acrylic box containing the resonant cavity and the injection cup. A specific amount of the dye (5 g) is injected into the cup through a narrow (5 mm) pipette. After complete injection of the dye, the pipette is pulled out slowly to avoid any adhesion of the dye to the surface of the pipette due to interface tension. The movement of the dye is recorded by imaging every 30 seconds for a two-hour period of time after the injection of the dye. This procedure is performed at 65 MHz for 0, 10, 20, and 30 W of electric power (0 W refers to the unstimulated case). Although the experimental setup was consistent and the body of the antenna used for stimulation exists in all the tests, the antenna emitted EM waves inside the medium only in the stimulated tests. Figure 25 shows the experimental setup during the injection of the dye.

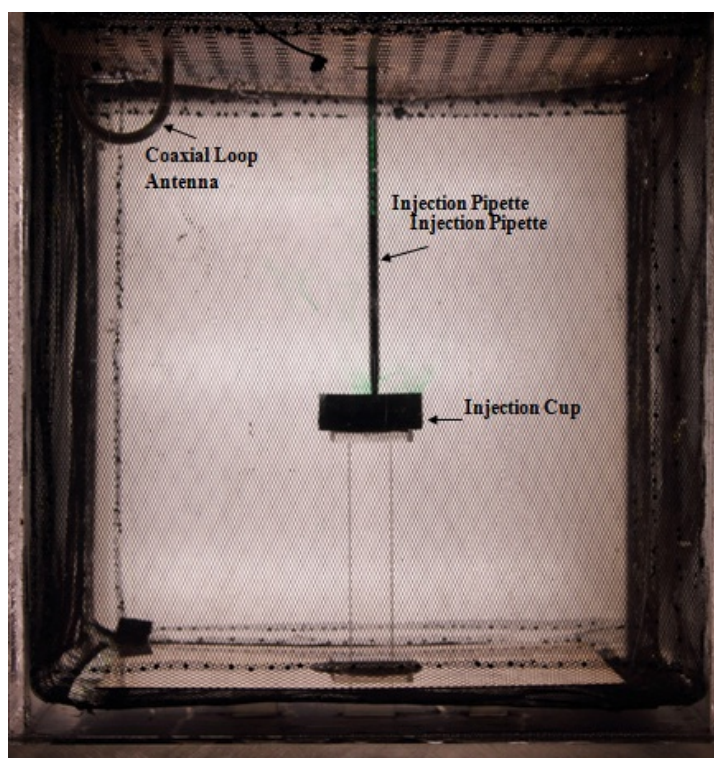


Figure 25 Experimental medium for the modified setup showing the acrylic box, resonant cavity filled with water, injection cup, injection pipette, and loop antenna.

Experimental Setup Details- The acrylic box was made from 1 cm-thick acrylic plates and a 1.2 cm-thick bottom plate. The sides when assembled measure 40 cm outside edge to outside edge. The bottom measures 45 cm × 45 cm, and the walls are centered leaving an even gap all around. To stiffen the walls and prevent sag or failure, 2.5-cm-wide stiffeners were added perpendicular to the walls creating a ridge 2 cm from the top edge. All acrylic parts were joined using “WELD-ON 4” glue, creating watertight and optically clear joints. This assembly provides a stable environment to conduct diffusion measurements while allowing for an unobstructed view for analysis.

The resonant cavity enhances the effects of the EM waves. The cavity structure increases the electric field amplitude and provides a controlled, standing-wave pattern in the medium. The conductive walls also electrically shield the test medium from the surrounding environment. The cavity structure is built using copper mesh screens instead of solid copper plates to enable imaging and visualization. It is noteworthy that the diameter of openings of the mesh is 3.175 mm (1/8 inch), which is much smaller than the wavelength of the applied 50-200 MHz frequency (160-660 mm in water). This mesh behaves electrically as a solid plate to an acceptable degree of accuracy. Hence, the copper mesh acts as a near perfect electric conductor over this range of frequencies.

The water is deionized and deaerated before each test. The use of deaerated water is quite important to prevent the generation of air bubbles, which can obscure images for analysis. When non-deaerated water is used, air bubbles form on the surfaces of the acrylic box, creating obstructions and error in the image analysis. Deionized water is provided through a supply accessed from a faucet in a laboratory. An ELE brand Water DeAiring System is used to deaerate the water for at least 45 minutes per batch. The test

medium is approximately 0.057 m^3 (57 liters), and several batches are required to fill the apparatus. Once the apparatus is filled with water, it is left overnight to settle any turbulence and reach a steady state.

The dye used for this set of experiments is a McCormick green food color that is electrically inert and nonreactive with water (Figure 26). The dye is first weighed in a vial using a scale to ensure a consistent proportion is maintained. This vial is covered with a penetrable cap for removal of the dye with a syringe. This method ensures consistent measurements for dye injections.



Figure 26 Green food color used as the diffusing material in the experiment.

A clear acrylic cup was built to allow introduction of the dye close to the center of the medium. The injection table has a total height of 15 cm, including the 1-cm top and bottom plates. A circular plastic cup with a radius of 30 mm is glued to the top plate of the table using a glue-gun. The cup is used to hold the dye close to the center of the medium (far from the boundaries) during the initial injection to prevent the dye from descending out of the table down to the bottom of the box. The table is held in place by adhesion to a copper plate. The glue used for this purpose is submersible Gorilla glue that

can attach glass to metal. The copper plate sits on the bottom boundary of the resonant cavity and can act as part of this boundary.

As mentioned, the medium and the dye in the test apparatus are stimulated by a loop antenna submerged in the medium. The antenna is built of an RG8 coaxial cable. Although both probe and loop couplings can be used for energy exchange from a coaxial line to a cavity, the resulting experimental EM fields of the two are not equal. For a home-built cavity, as the one used here, the loop coupling was experimentally the best choice. Figure 27 shows the reflection frequency-response at Port 1 (S_{11}) due to the medium when using the probe coupling. The horizontal and vertical axes are frequency (MHz) and reflection-response (dB) respectively. As seen in Figure 27, in the interested range of frequency (50-200 MHz), the values of S_{11} are near 0 dBm everywhere showing poor coupling of the RF power from the 50- Ω source (i.e., amplifier) to the cavity. According to the definition of S_{11} ,

$$S_{11} = 20 \log\left(\frac{\text{Power recieved by Port 1}}{\text{Power transmitted by Port 1}}\right) \quad (31)$$

which is the logarithm of the ratio of the power reflected to Port 1 to the power transmitted from Port 1, when this ratio is 0 dBm, all the transmitted power is reflected back, and therefore no power is coupled to the cavity box.

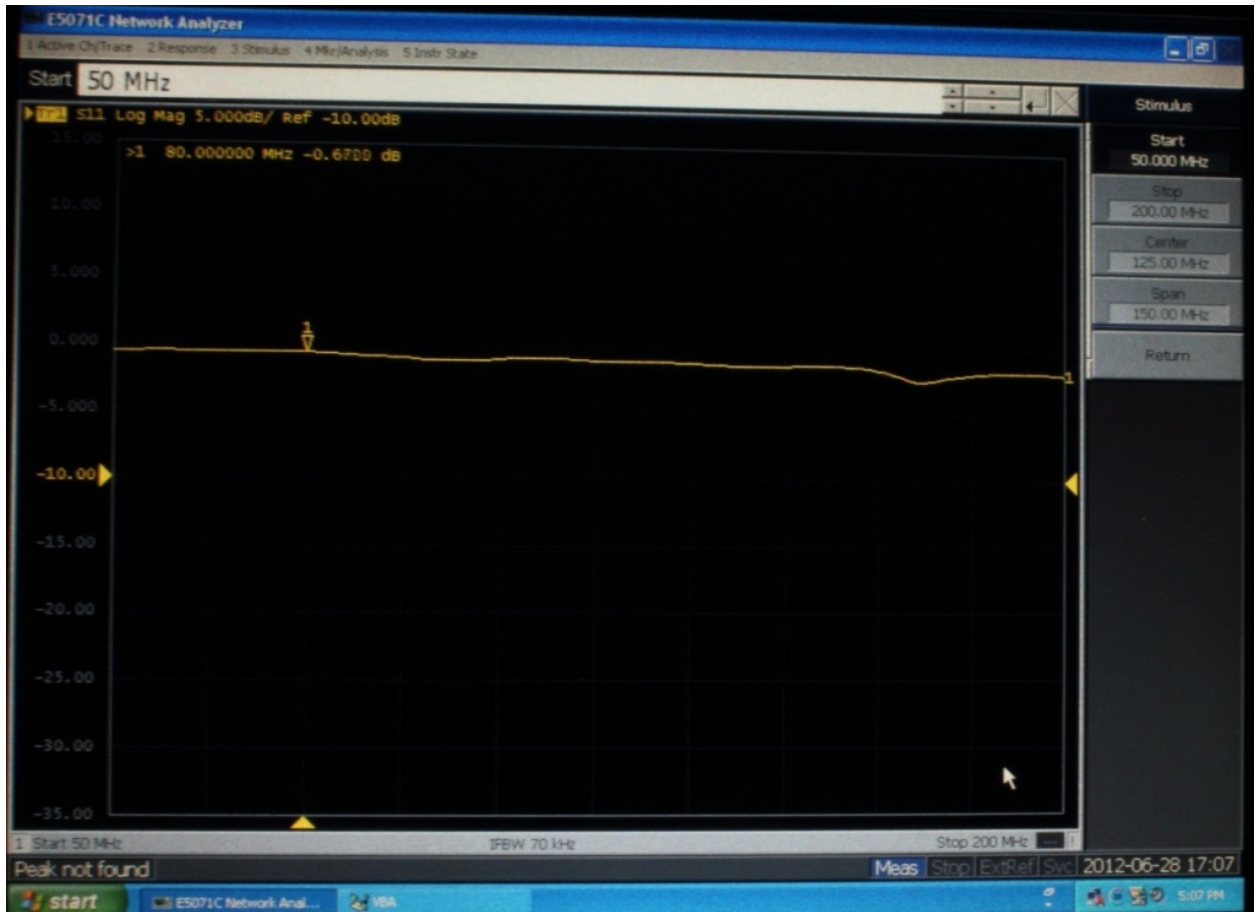


Figure 27 S_{11} (dB) of the medium when using a probe coupling.

However, measuring S_{11} for the same setup when the loop coupling is used, the measured S_{11} shows resonance at the range of frequencies of interest (Figure 28). Based on these values, at specific frequencies, which are the frequencies of specific modes of the cavity, more energy can be coupled into the cavity. In other words, for these frequencies with the loop antenna, more coupling exists between the medium and the EM source (i.e., amplifier). As a result, a loop antenna is used as the source of EM waves for the resonant cavity.



Figure 28 S_{11} (dB) of the medium when using a loop coupling.

The coaxial cable is shielded for a length of 140 mm at one end and bent to create a loop antenna in the resonant cavity. The outer conductor of the cable is grounded at both ends of the cable. At one end, the cable is screwed to the matching box, which is electrically connected to the rest of the grounded electrical equipment and leads to grounding the cable. At the other end, where the antenna meets the resonant cavity, the outer conductor surrounds a copper pipe electrically connected to the top boundary of the resonant cavity as seen in Figure 29. This approach is used to apply the same grounding system for the equipment, the antenna, and the resonant cavity. In order to ensure that the

inner conductor of the antenna is connected to the top boundary of the resonant cavity (as described in Chapter 2), the inner conductor passes through a brass piece welded to the top boundary. The continuity of different parts of the setup is always checked using a multimeter.

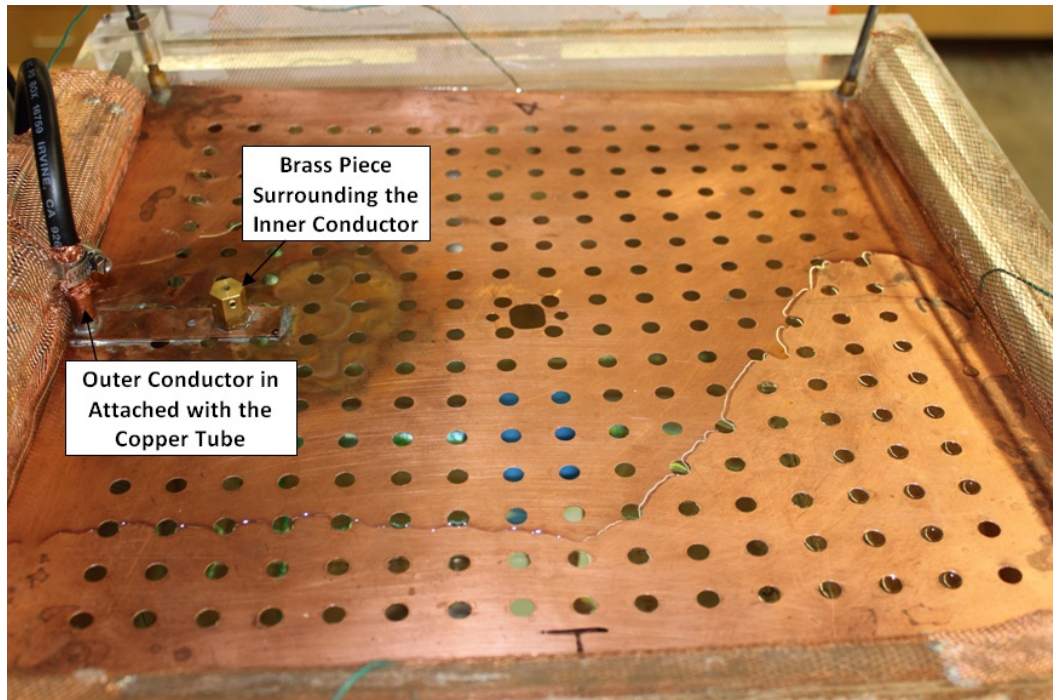


Figure 29 Grounding loop antenna by connecting antenna to top boundary of resonant cavity, photo of top surface of resonant cavity.

A continuous wave (CW) RF signal was generated using an HP E4400B signal generator. A Model 100 LMB amplifier manufactured by Amplifier Research was used to amplify the generated signal. To maximize the forward power output into the testing medium and reduce the reflection back into the amplifier, the impedance of the source (Z_{source}) and of the load, in this case the medium (Z_{load}), must be equal,

$$Z_{\text{source}} = Z_{\text{load}} \cdot \quad (32)$$

A matching network was used to match the impedance of the testing medium to the source's impedance (i.e., of the amplifier = $50\ \Omega$). The L-shaped matching network circuit was confined to a metal to contain the EM waves and provide shielding. This network was used to minimize the reflection at the interface between the medium of interest, the antenna, and the amplifier. Matching the impedance of the testing medium and the source (amplifier) ensures the maximum power transfer into the medium and protects the amplifier. The matching network includes two variable (10-pF to 500-pF), two-gang, air capacitors, one in parallel, and one in series to tune the impedance. The components were connected with 50- Ω RG8 coaxial cables. A schematic of the network is shown in Figure 30.

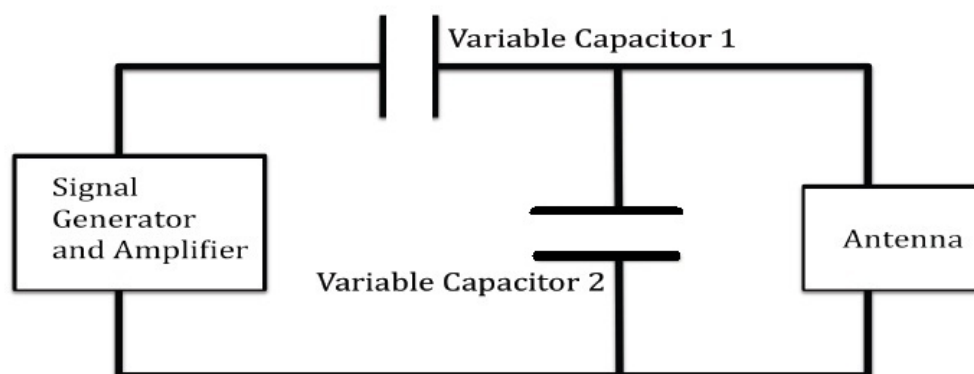


Figure 30 Schematic of impedance-matching network.

This impedance matching was performed for each individual frequency within the frequency range of the optimum performance of the amplifier (50 MHz to 230 MHz). To measure the circuit impedance for network matching, an Agilent Technologies E5071C vector network analyzer was used. At each frequency, the antenna in the medium was

matched using the matching network to find the lowest reflected power. The test apparatus for the EM stimulation tests are shown in Figure 31.

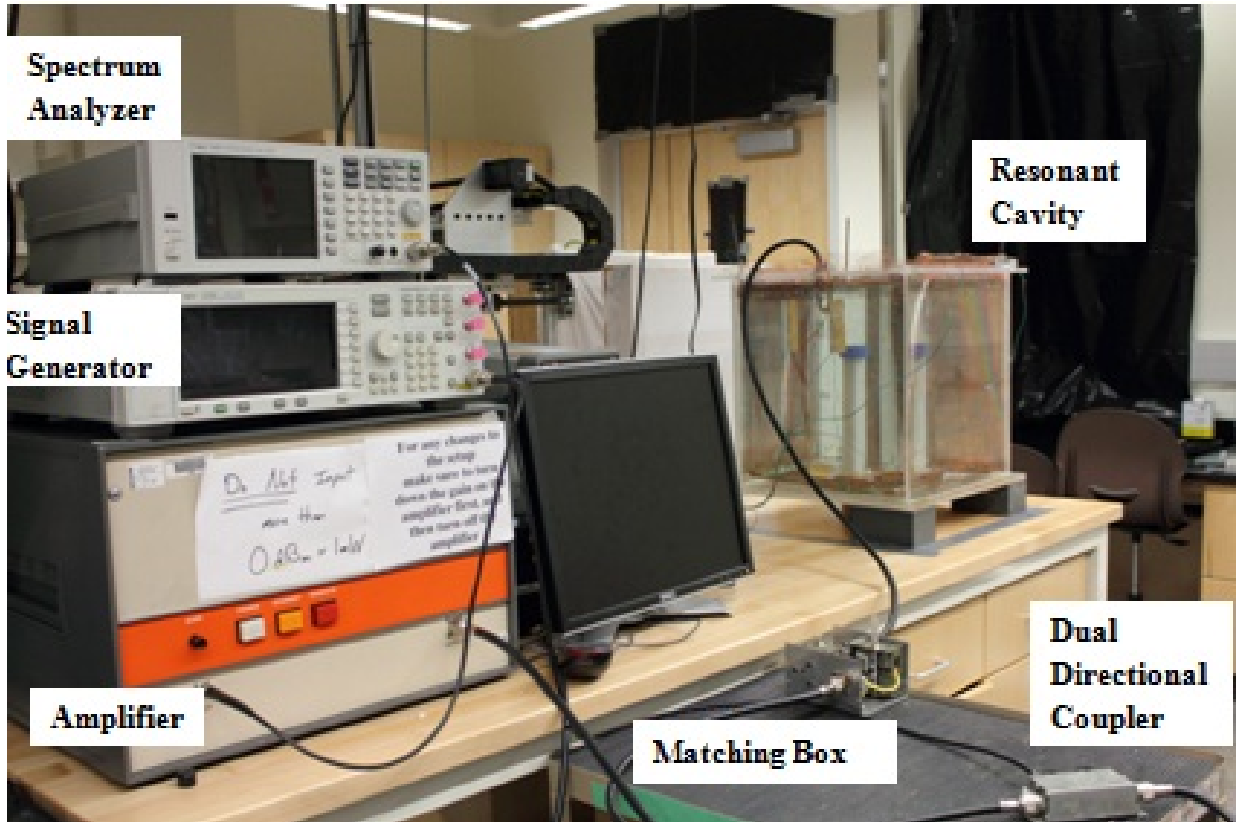


Figure 31 Test apparatus used in modified experimental setup including amplifier, signal generator, spectrum analyzer, and the dual-direction coupler and matching box (respectively, right and left on the black table).

Imaging- Digital imaging was used to analyze the transport of the dye and to determine the stimulation effect. Taking images at consistent time intervals and using the images to measure dye concentrations can help to determine the transport rate.

Images are taken using a Canon Rebel T2i 18-megapixel digital camera. The camera uses an EFS 18-55 mm lens, fully zoomed out to encompass the entire testing medium. To ensure consistent and stable images, a tripod supports the camera. To actuate

the camera and minimize vibrations, a remote capture program is used to control and download images. Canon's EOS software package, specifically the remote capture function, is used to capture images at designated intervals. Captured images are downloaded directly to the computer through the remote capture program. Images can be captured at a range of intervals, but were taken at 30 second intervals for this experiment.

The camera is set in manual mode to enable the control of shutter speed, aperture, ISO (image sensor sensitivity), and image format to provide consistency across experiments. Images are captured in RAW format not to introduce distortion from compression artifacts. A shutter speed of 1/40 sec, an aperture setting of F5.6, and an ISO of 400 produces the best results with the lighting conditions. The lighting apparatus is explained in the following section. The manual-focus mode was found to be consistent and, therefore, was used for this experiment.

The lighting of the test medium is very important for the analysis of the diffusion. Images were captured on the opposite side of the light source to enable measurements of the dye through the light transmission mode. To ensure a uniformly lit background, a light box was built along with a diffusive filter. The light box consists of a wooden frame built out of 5.08×10.16 cm (2" \times 4") fir attached to a 12.7-mm (1/2-inch) plywood backing. Three 60.96-cm (2') long florescent tube lights were attached to the inside and back of the box. To diffuse the light, a layer of white Lycra was stretched to cover the 12.7-mm (1/2 inch) plywood backing. To diffuse the light further and to create a more uniform backlight for the apparatus, a second frame covered with another layer of white Lycra was used. These two layers of Lycra were spaced approximately 25 cm apart to diffuse the light enough to reduce drastic backlight gradients to an acceptable level

although not enough to completely eliminate variations in the light intensity. Figure 32a shows the structure of the lighting box and Lycra layers while Figure 32b shows the lighting device when the lights are on.

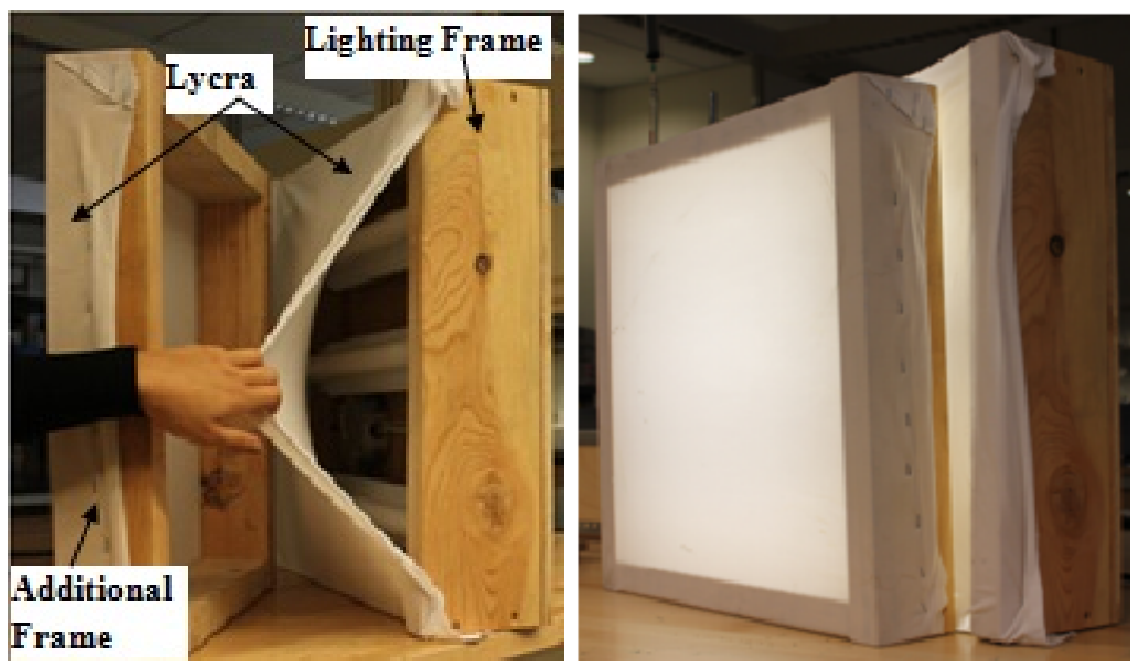


Figure 32 (a) Lighting frames with a layer of Lycra and the additional frame with another layer of Lycra to create uniform lighting and (b) above-mentioned frames when lights are on.

The pixel values of the two-dimensional (2D) digital images correlate to the integral of the dye concentration along lines of sight. The images are broken into a matrix, which can be processed to determine the properties of the dye transport. The values of these matrices report the pixel intensity at different locations within the medium. It is important to note that the intensity values in image matrices represent the degree of brightness of the pixels. As a result, darker pixels (pixels containing more dye) have smaller values of pixel intensity in the broken matrices of digital images. This

image analysis enables the study of the transport mechanism of the dye and the effects of EM stimulation.

Electric Field Mapping- The full 3D vector electric field is necessary to understand the RF radiation pattern and correlate the RF field to the dye concentration and transport, and it is necessary to understand the stimulation mechanisms. However, the measurement of the field using the existing Z-polarized (vertical), monopole probe (RG-402, with 25 mm of the outer conductor stripped) results in a field amplitude dominated by the Z-component of the electric field. Therefore, an experimentally validated simulated electric field using COMSOL software is needed. Hence, the electric field is mapped in the test region using a three-dimensional (3D) computer-controlled translation-table. A 50- Ω coaxial probe connected to a spectrum analyzer is moved to nodes of a desired 3D grid. By probing the medium and recording the electric field measurements, a 3D map of the field is constructed. The triaxial antenna-positioner is built using an aluminum frame, stepper motors, and ball screws for positioning. The mechanical and electrical components are designed and built in-house. Figure 33 shows the triaxial antenna-positioning device connected to the coaxial probe.

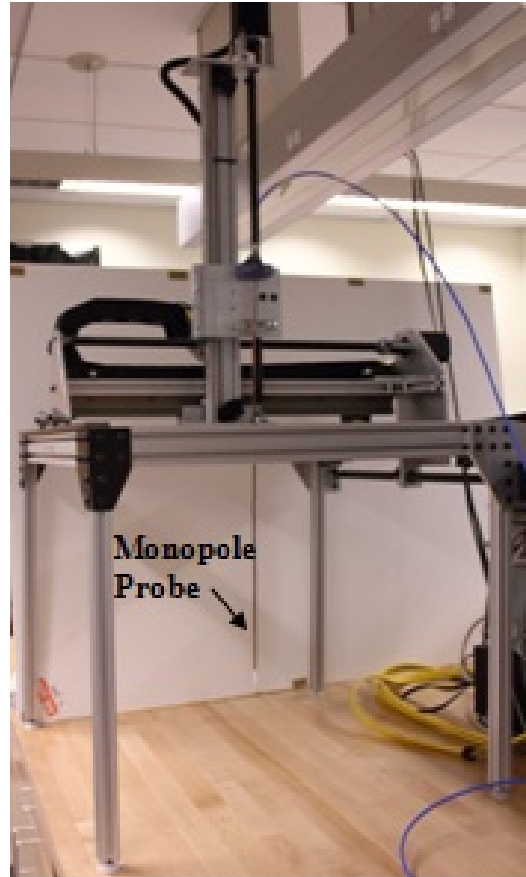


Figure 33 Triaxial antenna-positioner connected to measuring coaxial, monopole probe.

The frame of the triaxial antenna-positioner is built out of a T-slotted aluminum frame made of 80/20 brand material bolt-joined using aluminum plates. There are metal tracks for the tool fixture to travel linearly along the three axes. Three stepper motors turning ball screws provide accurate translation of the aperture to enable precise and consistent positioning. The three stepper motors, a controller network, and drivers are all acquired from Keling Inc. The tool fixture consists of an aluminum plate with two hole-drilled plastic pieces to attach and hold the antenna. The hole-drilled plastic pieces secure the glass tube casing over the monopole probe to provide rigidity and waterproofing. The probe is constructed of a rigid coaxial wire (RG 402) with 25 mm of the outer shield

stripped and connected to the spectrum analyzer through an 18-GHz precision test cable. The 18 GHz precision test cable is made of an RG 58 coaxial cable with an N-type male connector at the spectrum analyzer connection and an SMA male connector at the probe end.

In order to move the triaxial antenna-positioner to a designated measurement location, a path script is written using Microsoft Excel and then exported into a tab-delimited file. The script consists of three columns corresponding to the three Cartesian coordinates (X, Y, and Z) of the probing node. To minimize errors, the path moves to each (X, Y) coordinates and then completes all moves on the Z-axis correlating to points on the X-Y plane. The probe stops for 2 seconds prior to taking a measurement to allow the cable to rest, and hence, the spectrum analyzer to acquire consistent readings. Readings collected using the spectrum analyzer at each point are exported to a tab-delimited, 4-column text file, corresponding to X, Y, Z, and the power measurement. Figure 34 shows an example of the output “txt” file.

X	Y	Z	P
-4.000	-10.000	-12.000	8.725
-4.000	-10.000	-10.000	8.555
-4.000	-10.000	-8.000	8.288
-4.000	-10.000	-6.000	7.689
-4.000	-10.000	-4.000	5.633
-4.000	-10.000	-2.000	1.963
-4.000	-10.000	0.000	-3.504
-4.000	-10.000	2.000	-14.170
-4.000	-10.000	4.000	-10.717
-4.000	-10.000	6.000	-5.342
-4.000	-10.000	8.000	-3.794
-4.000	-10.000	10.000	-3.532
-4.000	-10.000	12.000	-3.338
-4.000	-8.000	12.000	-3.391
-4.000	-8.000	10.000	-4.776
-4.000	-8.000	8.000	-6.633
-4.000	-8.000	6.000	-10.950
-4.000	-8.000	4.000	-13.194
-4.000	-8.000	2.000	-4.048
-4.000	-8.000	0.000	1.496
-4.000	-8.000	-2.000	5.352
-4.000	-8.000	-4.000	7.620
-4.000	-8.000	-6.000	8.251
-4.000	-8.000	-8.000	8.537
-4.000	-8.000	-10.000	8.684
-4.000	-8.000	-12.000	8.780
-4.000	-6.000	-12.000	8.787
-4.000	-6.000	-10.000	8.724
-4.000	-6.000	-8.000	8.618
-4.000	-6.000	-6.000	8.443
-4.000	-6.000	-4.000	8.105
-4.000	-6.000	-2.000	7.297
-4.000	-6.000	0.000	4.676
-4.000	-6.000	2.000	1.285
-4.000	-6.000	4.000	-2.891
-4.000	-6.000	6.000	-6.276

Figure 34 Output file of LABVIEW showing Cartesian coordinates of each measuring node as well as measured power magnitude.

The program developed in LabView software controls the three stepper motors through a control box. The program is written to move the probe in three directions in incremental moves, according to a tab-delineated text-script written for the desired path, along either of the depth (vertical, XZ and YZ) and/or cross-sectional (horizontal, XY) slices. The probing to map the electric field is conducted on two-dimensional 2-cm-grid slices in the test medium. It is important not to interfere with the antenna, support table, upper supports of the antenna, and dye injection pipette while electric field mapping is performed. The measurements are the peak power, as recorded by the spectrum analyzer at the frequency of the signal. The spectrum analyzer is controlled remotely by the LabView program and set to a range of available frequencies of 50 MHz to 200 MHz, which are the lower and upper limits of the spectrum analyzer.

Temperature Measurement- In order to investigate the effect of temperature on the dye flow, the temperature of the water close to the antenna body was recorded at different EM-stimulation frequencies. The thermometer is a Go!Temp brand with a resolution of 0.07°C and Logger Lite™ software that enables the user to collect the temperature at different times. The software also plots the temperature versus time for the collected data. The temperature is recorded at 1-minute time intervals for different tests with different applied frequencies. It was verified that the RF stimulation did not affect the measurement circuitry.

Stimulation- The modified experimental setup is also simulated in COMSOL Multiphysics. The step-by-step description of COMSOL simulation is provided in Appendix B. Figure 35 shows the model of the improved experimental setup in COMSOL Multiphysics.

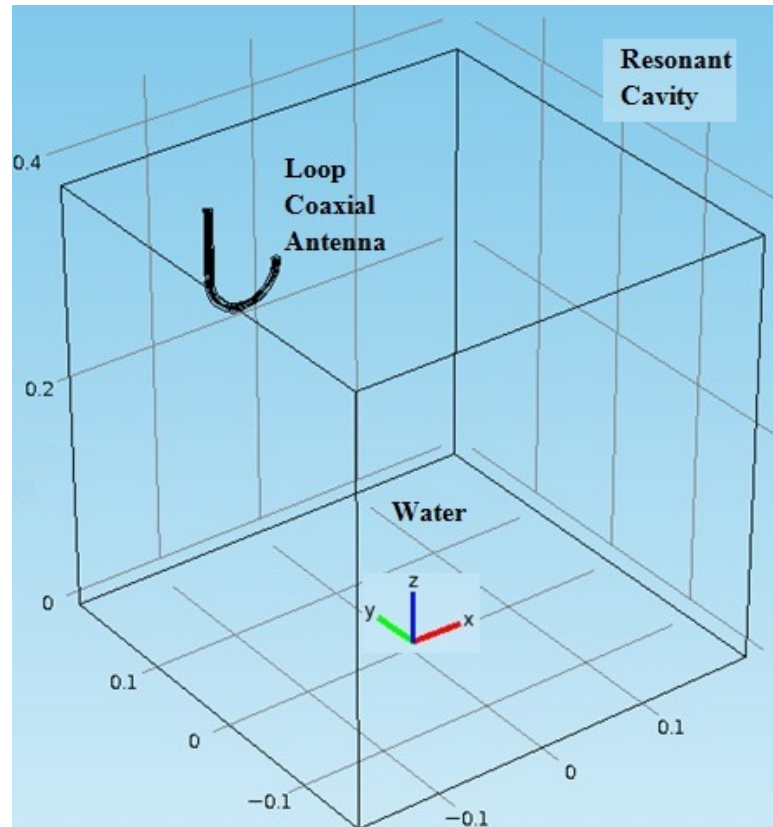


Figure 35 Modified experimental setup as modeled in COMSOL Multiphysics. The coordinate system shows the axes direction and the origin of the axes. The numbers in the figure are in meters.

After the model is validated with the experimental results, the total field values from the COMSOL results can be imported into MATLAB to enable a dielectrophoresis study. If dielectrophoresis is the controlling mechanism for the dye motion, a force should exist in the opposite direction of the gradient of the electric field squared ($\nabla|E|^2$). In other words, because the dielectric constant of the dye is smaller than that of water, the direction of the dielectrophoretic force should be from the larger electric field intensity toward the lower electric field intensity.

The electric field components of the simulated model in COMSOL Multiphysics are exported to MATLAB. The exported files contain the electric field components at all

nodes in the medium spaced on a 2 cm grid. Figure 36 represents the location of the nodes in the domain under study as well as the coordinate system for the geometry. A MATLAB script file (m.file) (provided in Appendix D) was written and developed using a forward finite difference method to calculate the gradient of the electric field squared ($\nabla|E|^2$) based on the equation

$$|\nabla E|^2 = \frac{|E|_{i+1,j,k}^2 - |E|_{i,j,k}^2}{dx} \hat{i} + \frac{|E|_{i,j+1,k}^2 - |E|_{i,j,k}^2}{dy} \hat{j} + \frac{|E|_{i,j,k+1}^2 - |E|_{i,j,k}^2}{dz} \hat{k}, \quad (33)$$

and the results can be plotted to investigate whether the flow of the dye agrees with the dielectrophoretic force directions.

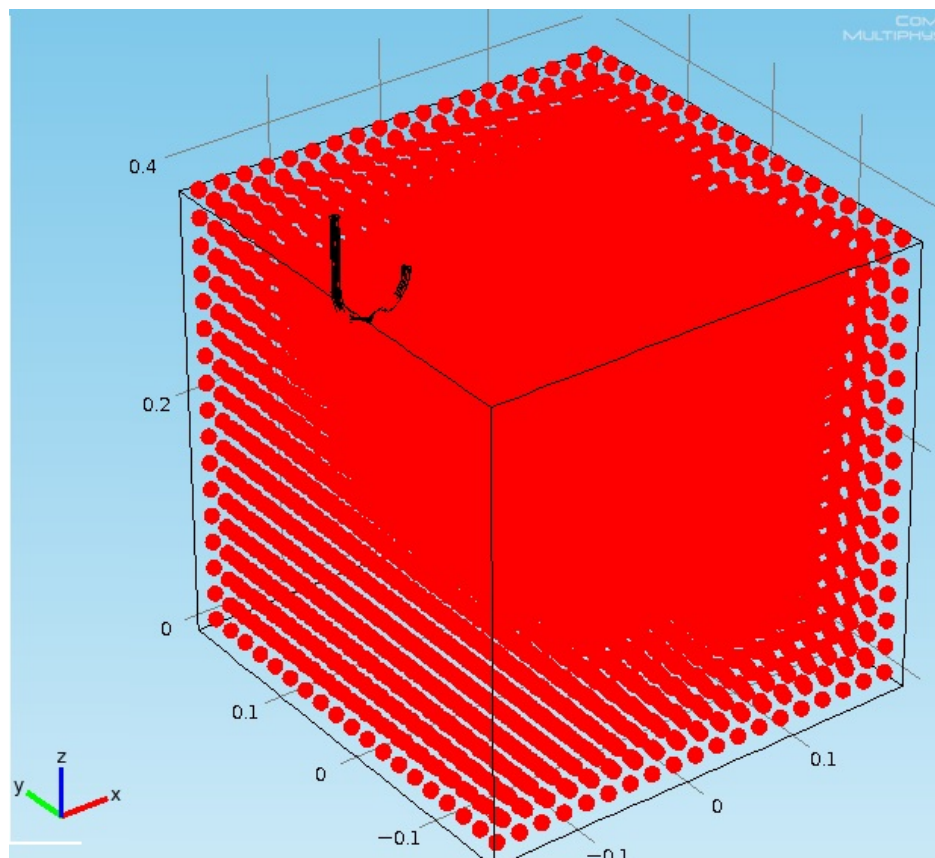


Figure 36 Location of nodes used to analyze effect of electric field pattern in COMSOL Multiphysics. The numbers in the figure are in meters.

Digital Analysis and Evaluations- Image analysis is performed to extract meaningful information from images by means of digital image processing techniques. In this work, RAW-format images are converted to the TIFF format and imported into MATLAB. The imported images are in an $m \times n \times 3$ matrix format with “m” and “n” representing the size of images (the length and width of images according to the camera zooming) and “3” representing the three color spectra (red, green, and blue) of images. Since the dye is green and light transmission mode is used for imaging, the red and blue spectra would best reveal the transport of the dye. Hence, only the red and blue spectra are analyzed. Each imported image is broken into two matrices of $m \times n$ size for red and

blue color spectra. The averaged, background image is subtracted from every image, leaving only the transporting dye. The elements of subtracted matrices represent the intensity of pixels at different locations in the box. It is important to note that pixel values are nonlinearly related to the location. The calibration factor that converts image pixel intensities to dye concentration varies spatially. As a result, pixel values before calibration to dye concentration at different locations cannot easily be compared. However, at each specific location, the change of the pixel intensity over time reveals information about the change in dye concentration. For a specific pixel, smaller values of pixel intensity indicate less light for that pixel, corresponding to greater dye concentration. Therefore, in subtracted images pixels where dye exists have negative values.

The existence of copper meshes in images, acting as the boundaries of the resonant cavity, adds enormous difficulty to any calibration required to convert pixel intensities to dye concentration. However, importing images into MATLAB and obtaining subtracted matrices for each test can enable us to perform several analyses. Different analyses have been performed on digital images to study the effect of EM stimulation. Below is a summary of these analyses for the results of the next chapter.

Pixel Intensity Summation: In order to eliminate the reflection of the boundaries of the box, a zone is selected to measure the amount of dye that has left the injection cup in each test. Figure 37 shows the zone used for this analysis. The selection of this zone is based on the upward transport of the dye as explained in the next chapter. The amount of the dye entering this zone is calculated at different time steps and is summed and recorded as the total amount of the dye in this zone at that specific time. To calculate the

amount of the dye, the background picture is subtracted from the test pictures to eliminate everything but the transporting dye. This amount is calculated over time (~100 minutes) for tests at frequencies of 65 MHz and 75 MHz and at various power levels (0W, 10W, 20W, and 30W). It is noteworthy that because of the unsuccessful calibration of images, the analysis is performed on the matrices containing the pixel intensities without any calibration. As a result, larger amounts of the dye in the zone are equivalent to smaller values of the sum of the pixel intensities not calibrated to dye concentration. However, in order to better analyze the data, the pixel values are adjusted to represent the larger values for darker pixels.

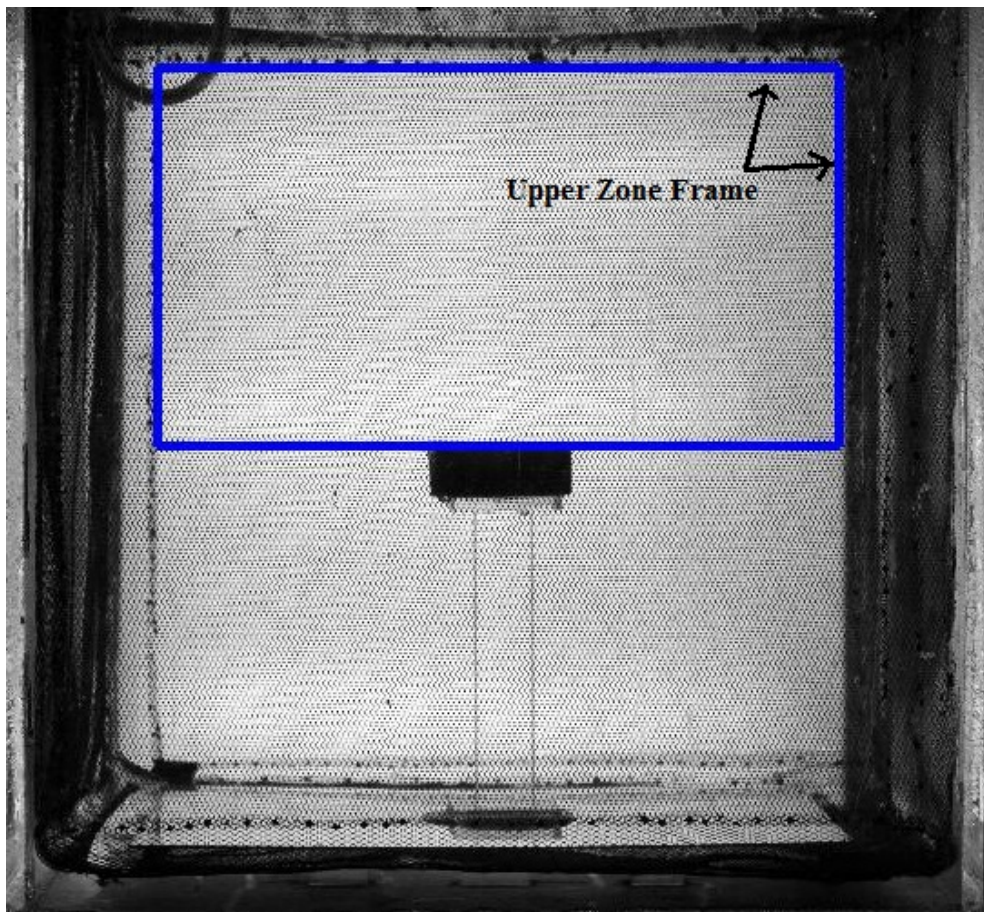


Figure 37 Study zone in Intensity Summation analysis referred to as upper zone.

Finger Height: In order to study the characteristics of the dye fingers such as their height and width, a finger zone is defined for the images. This zone is shown in Figure 38, which includes the dye fingers for the majority of time during the upward movements of the dye, when the medium is stimulated at 65 MHz. This study is limited to the tests performed at 65 MHz because of stronger, more controlled finger movements at this specific frequency. After the background image is subtracted from the test images, the analysis can begin. As mentioned, for the subtracted image matrices, negative pixel values represent locations with higher dye concentration. The number of pixels containing dye is recorded for different heights of the selected zone at different times. The number is a representation of the width of the finger. This method enables a study of the width of the fingers at different heights for each test. At each height, the width is summed over time, and the results can be plotted versus height. The results are shown in the next chapter.

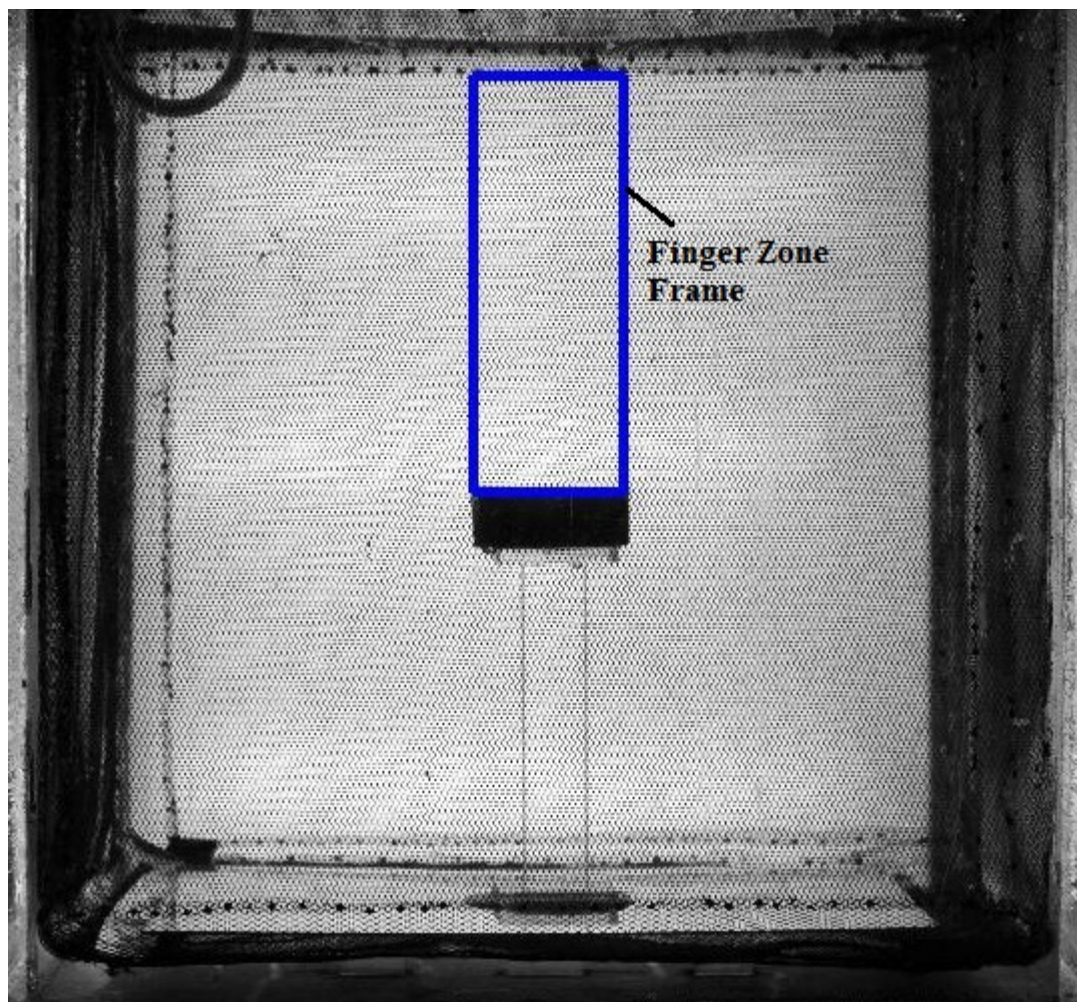


Figure 38 The study zone in the Finger Height analysis referred to as the finger zone.

CHAPTER FOUR: SUMMARY OF RESULTS AND DISCUSSION

The results of this work are presented in two sections. In the first section, the results of the simulation and further analysis of Sangrey's work by the author are provided. As discussed later, these results provided the impetus to modify the experimental setup for a better understanding of the controlling phenomenon in his work. In the second section, the results of the experiments performed with the modified setup are discussed. The results from the analysis of the experimental and simulation data for the new setup are also explained to quantify the effect of EM stimulation.

Section 1: Simulation, Digital Analysis, and Evaluations

Simulations

The simulation, using COMSOL Multiphysics, of the experimental setup of Sangrey's work (2011) is studied at the experimental operating frequency of 154 MHz. The simulation is capable of providing the electromagnetic field vectors and contour maps at various locations within the studied medium. The contour maps of E_z (Z-component of electric field) are investigated here for comparison with the experimental results. The experimentally measured electric field values are dominated by the Z-component of the electric field because of the vertical orientation of the measuring (vertically polarized monopole) probe. Therefore, in order to compare the simulation results with the experimental results, the measured field is compared with the simulated E_z . Figure 39 shows a schematic of the location of nine selected depth (vertical) slices

within the medium on which the experimental probing was performed. The simulated contour map of E_z is also studied on corresponding slices to validate the simulation. Figure 40 shows the experimental and simulated contour maps of the electric field amplitude on corresponding depth-slices shown in Figure 39.

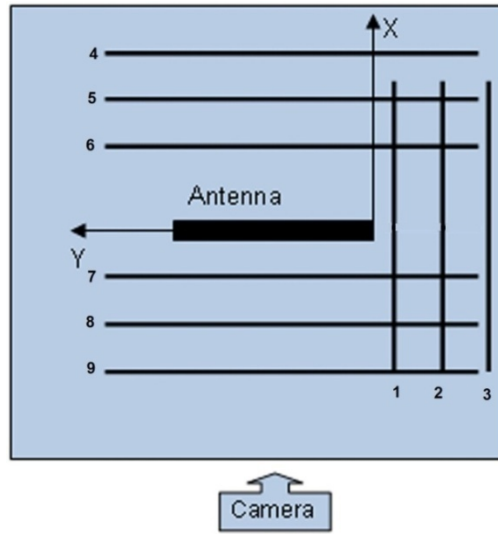


Figure 39 Schematic of locations (top view of the setup) of field mapping on depth (vertical) slices.

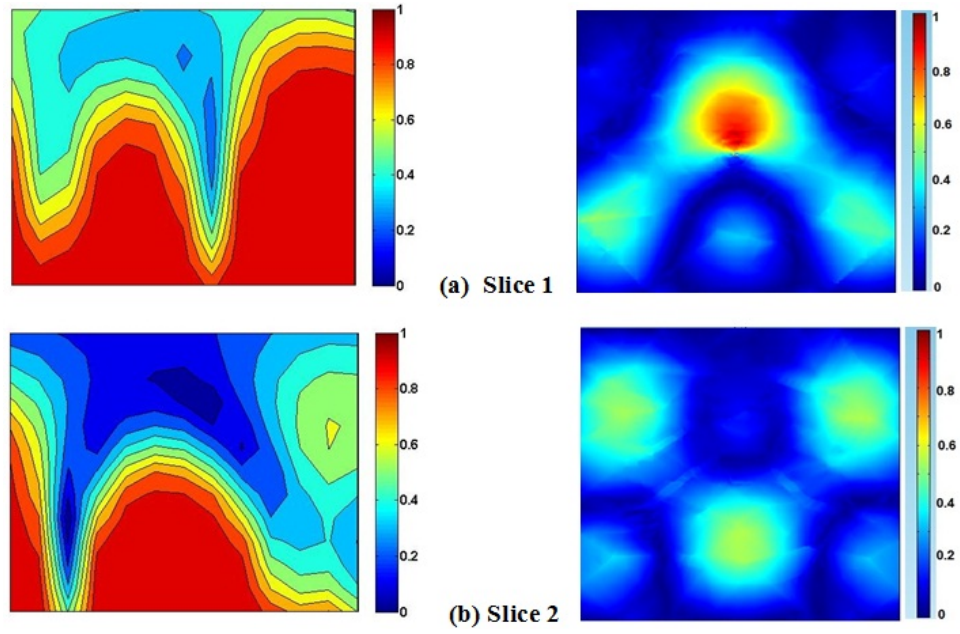


Figure 40 Experimentally measured (left) and simulated in COMSOL Multiphysics (right) normalized electric field color map for depth-slices of Figure 39: a) Slice 1 (XZ Slice), b) Slice 2 (XZ Slice).

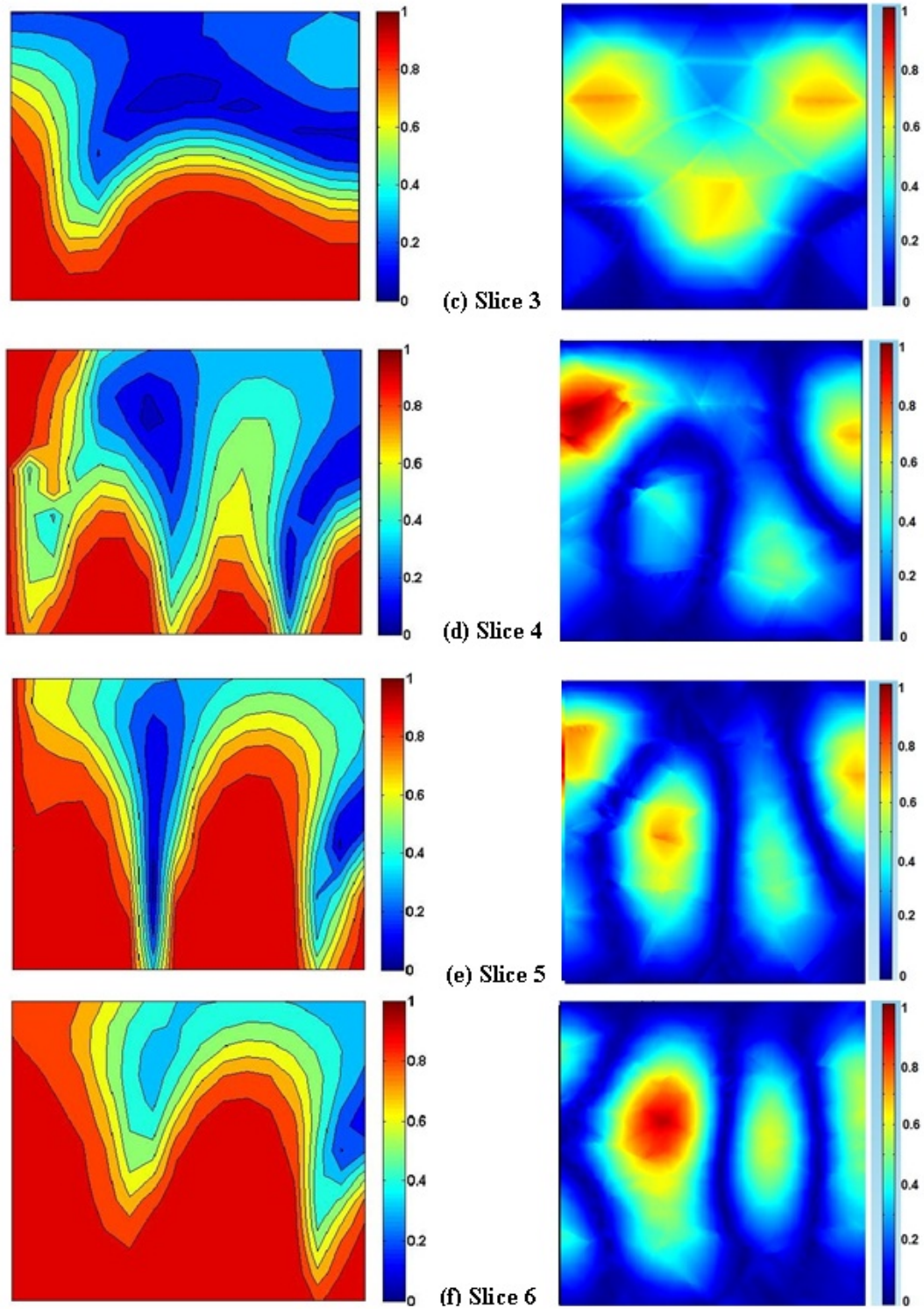


Figure 40 (Cont.) Experimentally measured (left) and simulated in COMSOL Multiphysics (right) normalized electric field color map for depth-slices of Figure 39: c) Slice 3 (XZ Slice), d) Slice 4 (YZ Slice), e) Slice 5 (YZ Slice), f) Slice 6 (YZ Slice).

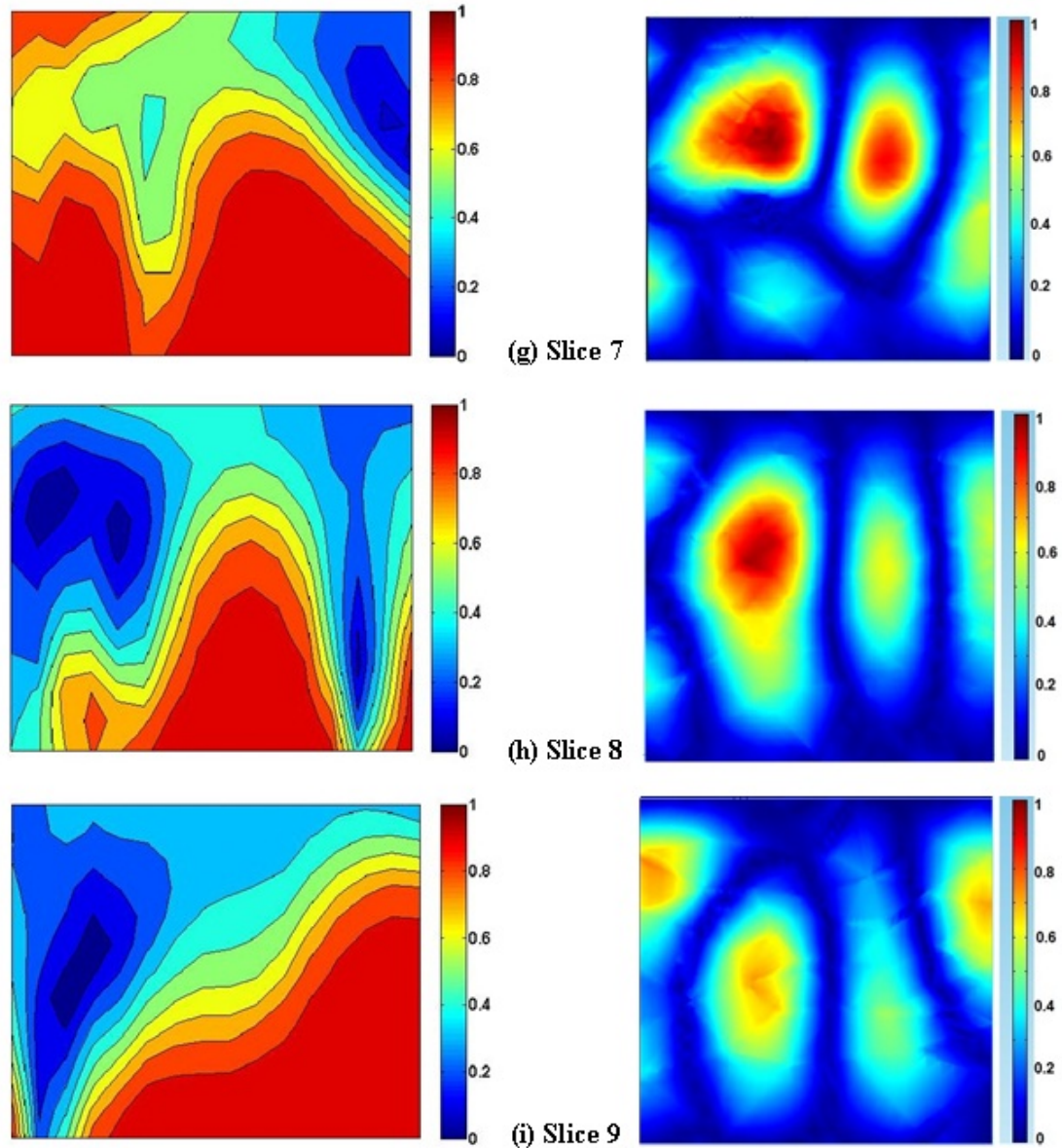


Figure 40 (Cont.) Experimentally measured (left) and simulated in COMSOL Multiphysics (right) normalized electric field color map for depth-slices of Figure 39: g) Slice 7 (YZ Slice), h) Slice 8 (YZ Slice), and i) Slice 9 (YZ Slice).

As seen in Figure 40, equivalent slices (experimental and simulated slices at the same location with respect to the antenna) do not provide the same pattern of the electric field. In all measured field maps, the highest intensity of the electric field is toward the bottom of the tank. The reason for this pattern is not completely understood. For

experimentally measured slices perpendicular to the antenna direction (Slice 1, 2, and 3), as the probing distance from the antenna increases from 2 cm to 6 cm and then to 10 cm, the intensity of the electric field decreases, but not as much as expected for the case of an attenuating propagating wave. In the case of a standing wave pattern, the field does not decrease radially away from the antenna. A standing wave pattern with a wavelength expected for the medium is visible in the color maps of the three components of the experimental electric field. The Faraday cage most likely causes this standing wave pattern instead of a propagating wave pattern. On the other hand, in the simulated electric field maps, the highest intensity of the electric field occurs toward the left (horizontally) and middle (vertically) of the tank.

The difference between the experimental and simulated results can be explained by the fact that not all details such as the body of the antenna positioning translation table was exactly modeled. Although the Faraday cage was supposed to isolate the medium from the surrounding environment, the metal structure of the translation table was placed within the cage and may have interfered with the electric field measurement. The antenna-positioning robotic table was placed within the cage since it was initially expected that the lossy water medium would minimize this interference. As a result, the experimental and simulated results do not agree. This discrepancy is the motivation behind modifying the setup from a Faraday cage to a resonant cavity. The prepared resonant cavity prevents any interference from surrounding structures because it can exclude the environment under study from outside objects, including the antenna positioner.

Digital Analysis and Evaluation

Investigation of Effect of Electric Field Magnitude on Concentration- The change in dye concentration in several sets of grouped nodes within digital images collected by Sangrey (2011), described in Chapter 3, is investigated. Figure 41 shows the location of two of the grouped nodes on the experimental contour map of electric field integrated along Y-axis. The study is limited to certain areas of the medium because of the existing boundaries and because of noisy areas from the reflection of light off acrylic walls and because of the random and strongly varying electric field pattern.

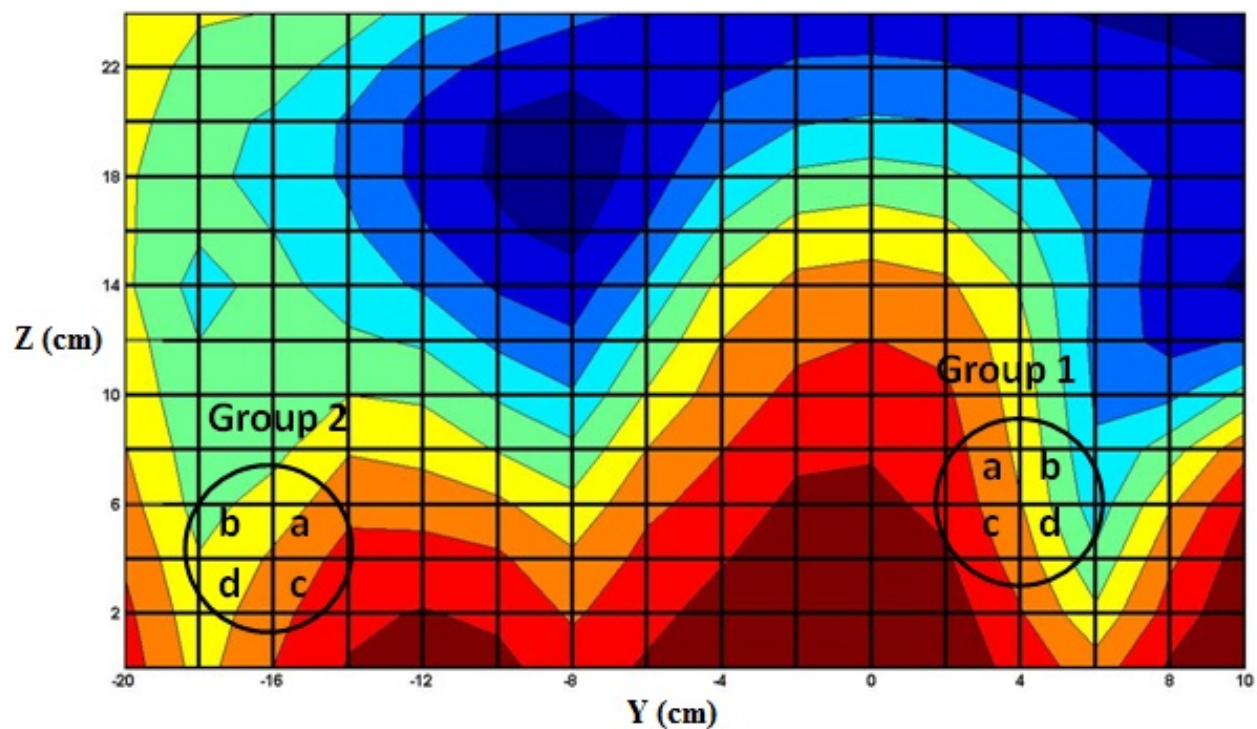


Figure 41 Grouped nodes used for investigation of effect of electric field magnitude on dye concentrations in Sangrey's work (2011). All parallel lines are located at a 2cm distance from their neighboring lines. Locations of perpendicular line-crossings coincide with nodes used in digital analysis.

Figures. 42 and 43 show the change of dye concentration for Groups 1 and 2 over time, respectively. As shown in Figure 41, grouped nodes “a” and “d” are along a contour line whereas grouped nodes “b” and “c” are perpendicular to the same contour line. The first interpretation of these figures is that for each power level, the divergence of the concentration of nodes along a contour line is less than that of the nodes perpendicular to the same contour line. In other words, the difference is greater for nodes normal to a contour line due to the flow or the movement of the finger flow perpendicular to contour lines. Although the difference between the concentrations of nodes normal to a contour line is larger, there is not a specific trend with the power magnitude, and the results do not appear monotonically related to the applied power. As a result, the correlation between the transport mechanism and electric field is more complicated. This complication is because at 30 W of RF power, the finger movement seems as random as the unstimulated tests. In order to derive a quantitative result from this study, a more organized field pattern –that would move the dye in one direction or contain the dye in the injection cup— is required to enable the investigation of the effect of the electric field magnitude on the dye concentration. This setup is feasible through appropriate design of a resonant cavity as performed for the modified setup.

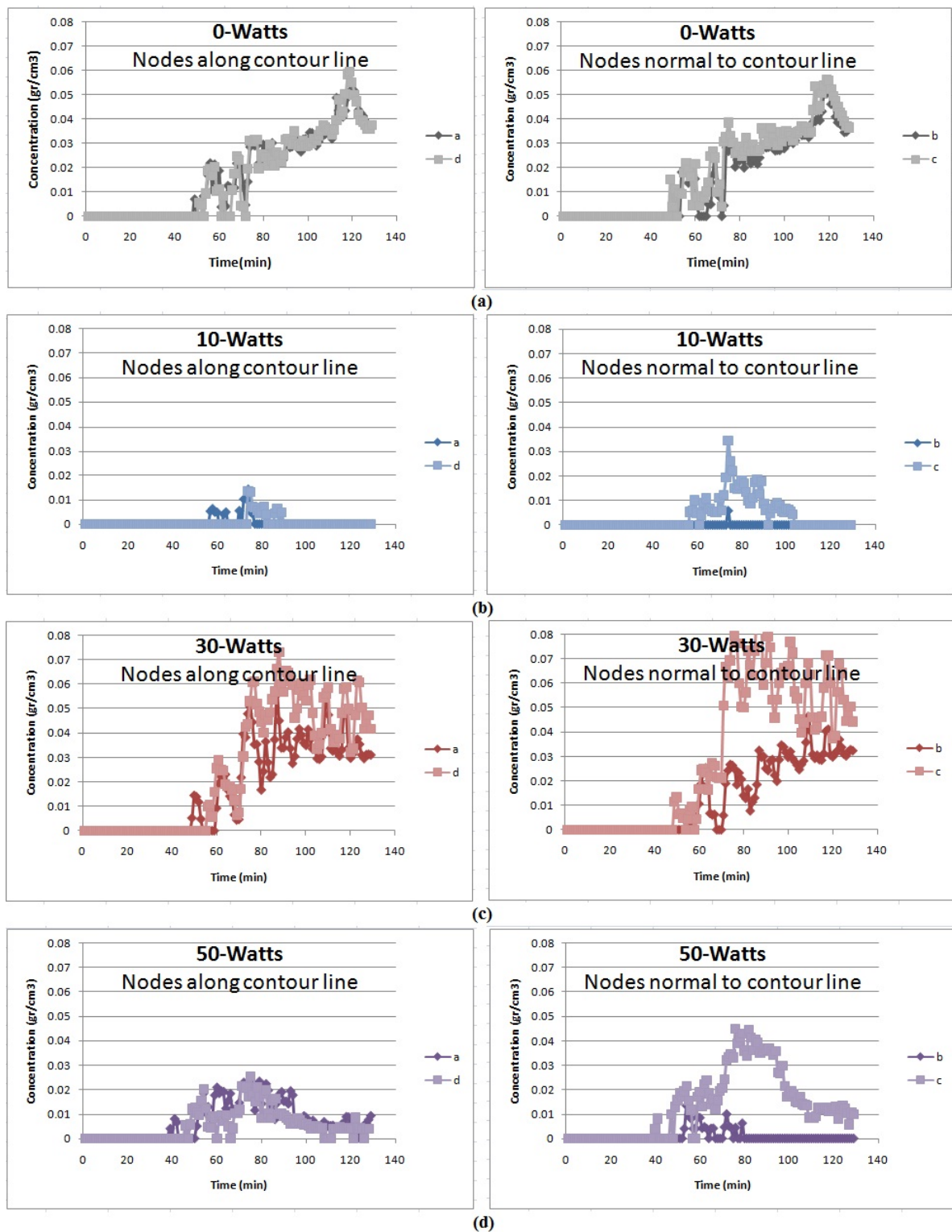


Figure 42 Change of Concentration over time for Group 1 for: (a) 0 W, (b) 10 W, (c) 30 W, (d) 50 W; ‘a’ and ‘d’ are groups of nodes tangential to electric field contour lines, and ‘b’ and ‘c’ are groups of nodes normal to electric field contour lines.

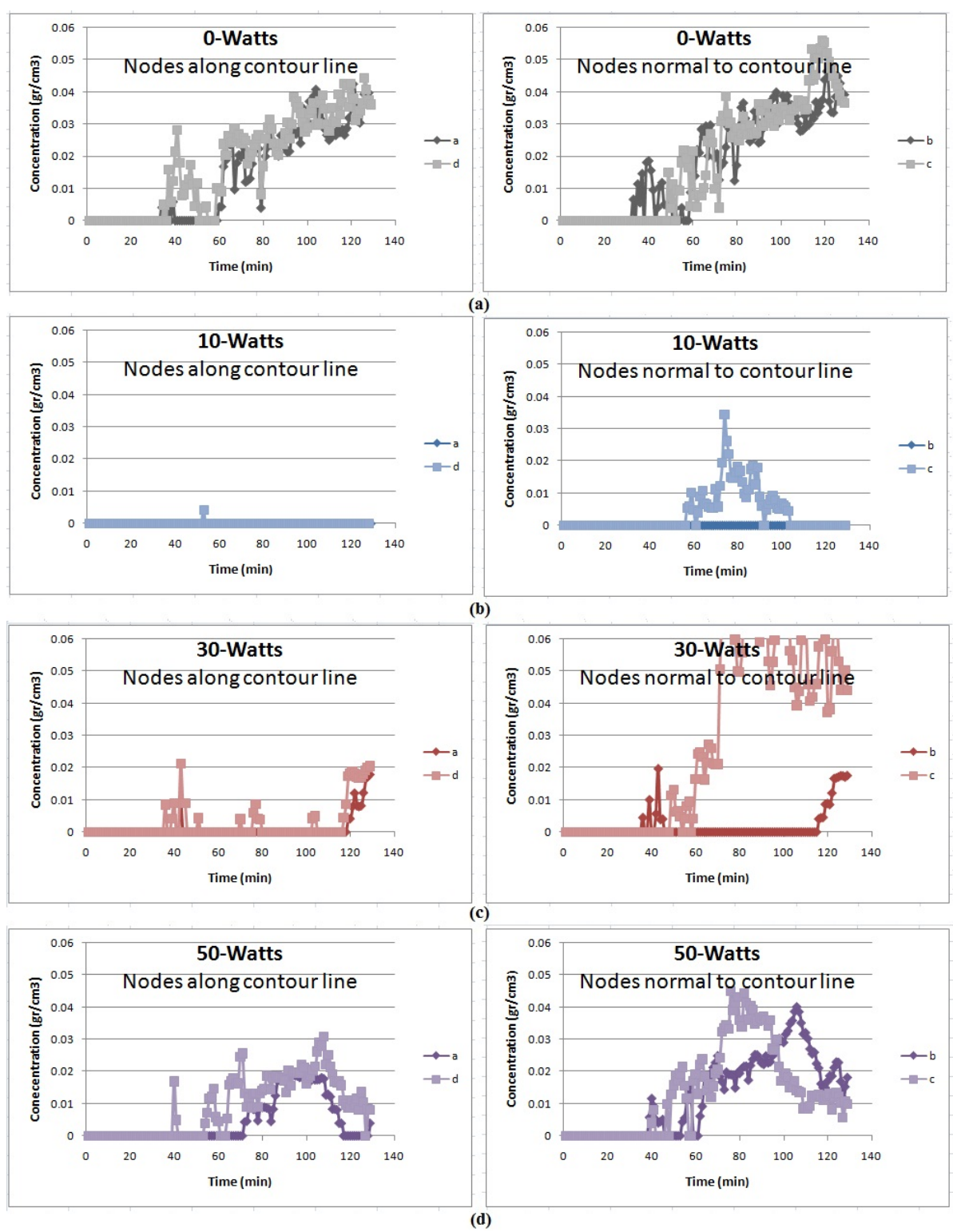


Figure 43 Change of Concentration over time of Group 2, for (a) 0 W, (b) 10 W, (c) 30 W, (d) 50 W; ‘a’ and ‘d’ are groups of nodes tangential to electric field contour lines, and ‘b’ and ‘c’ are groups of nodes normal to electric field contour lines.

Investigation of Effect of Power Level on Transport Rate- In this section, attempts are made to find the correlation between the rate of dye transport and the electric power level. One approach to obtain a quantitative representation for the transport rate is calculation of the diffusion coefficient. Although during the stimulation, other phenomena are present and control the transport of the dye, Eqn. 30 is used to calculate D for all the tests. The resultant D will not be the exact value of the diffusion coefficient but an effective (equivalent) representation of the rate of transport of the dye for each test (i.e., an equivalent value representing a mix of dominant diffusion and much smaller advection and finger movement, if only the diffusive flow equation is used to explain the flow).

For each test, a MATLAB code (.m file) is developed to calculate D for all nodes at all times. The values of D are stored and averaging is performed to provide an average rate of transport. If simple averaging is performed over the entire region, including the fingering areas, the values obtained for D will be unreasonably large even for the unstimulated tests. A simple averaging of D over time and the entire medium for two unstimulated runs results in a value of $D = 0.056 \text{ cm}^2/\text{s}$. This value is unrealistically large for liquid-in-liquid diffusion. Therefore, the diffusion equation cannot be used when the diffusion is not dominant over other forms of flow in the entire space. However, if the study is limited to the regions where viscous fingers do not exist, the transport mechanism of the dye should be dominantly diffusion, and the D values should be of acceptable values within the order of magnitude of liquid-liquid diffusion. It is also assumed that inside the regions of the fingers, diffusion could be occurring. In order to present a consistent analysis for all tests, averaging D is limited to values within the

common range of diffusion coefficient for a liquid in water diffusion (i.e., 10^{-4} - 10^{-6} cm^2/s ; Cussler, 1997).

A more detailed study on the unstimulated tests shows that the viscous fingering of the dye during diffusion almost never stops. This phenomenon occurs everywhere in the acrylic box during the transfer mechanism. Nevertheless, inspecting the concentration of the dye at specific nodes and times with an acceptable value of D (i.e., 10^{-4} to 10^{-6} cm^2/s) confirms the previous hypothesis about diffusion and fingering zones and provides interesting results. Reasonable values of the diffusion coefficient at different nodes are observed when the concentration is low (far outside fingers) or where the node is located within a stable high-concentration area (within stable fingers). In the former situation where the node is located far from the fingering area, diffusion can take place whereas in the latter case, the diffusion is indeed occurring within the fingering region. The dye diffusion coefficient was also experimentally measured using an NMR spectrometer. The results provide a diffusion coefficient in the order of 10^{-6} cm^2/s , which agrees with the modified analytical data.

Because of the tendency of the dye to move toward the right side of the medium during EM stimulation, a modified version of the code was developed in MATLAB and utilized. The modified version separately performs the calculation and averaging of D values for Zones 2 and 4. The averaging is limited to the areas with D values within the allowable range. The calculated diffusion coefficients for Zones 4 and 2 are listed in Tables 4.1 and 4.2 for all the tests. As is shown, the calculated average D values for the test performed at 10W are not within the acceptable range, and analysis is not applicable

on these data. The script file for the calculation of D in Zone 4 is provided in Appendix C.

Table 4.1 Diffusion Coefficient for Zone 4, calculated according to Equation 30.

Diffusion Coefficient of Zone 4			
Input Power (W)	Range of D ($\times 10^4 \text{ cm}^2/\text{s}$) (W/O considering common range of D)		D_{ave} ($\times 10^4 \text{ cm}^2/\text{s}$)
0	Test 1	-147—1108	5.22
	Test 2	-0.51—3.90	
10	Test 1	-0.11—0.08	4.54
	Test 2	-0.62—0.35	
30	Test 1	-7.90—4.90	4.65
	Test 2	-1.17 — 1.19	
50	Test 1	-2.80 — 5.80	5.13
	Test 2	-1.50 — 7.30	

Table 4.2 Diffusion Coefficient for Zone 2, calculated according to Equation 30.

Diffusion Coefficient of Zone 2			
Input Power (W)	Range of D ($\times 10^4 \text{ cm}^2/\text{s}$) (W/O considering common range of D)		D_{ave} ($\times 10^4 \text{ cm}^2/\text{s}$)
0	Test 1	-232.00 — 6.00	5.6
	Test 2	-.93 — .60	
10	Test 1	-.08 — 0.16	N/A
	Test 2	-.30 — 0.03	
30	Test 1	-0.2 — 0.04	3.15
	Test 2	-0.14 — 0.09	
50	Test 1	-0.19 — 4.07	3.88
	Test 2	-0.65 — 0.20	

In order to demonstrate the effect of EM power level on the rate of transport, the results are also plotted in Figure 44. As shown in Figure 44, D is almost the same for the two zones before stimulation. However, after EM stimulation begins, the magnitude of average D becomes larger for Zone 4 compared to Zone 2. This increase indicates an effect from the electric field pattern and the antenna configuration on the rate of

transport. The decrease in the D values immediately after the beginning of EM stimulation can be attributed to the fact that the electric field pattern pushes the dye to regions other than what is forced by the diffusion phenomenon.

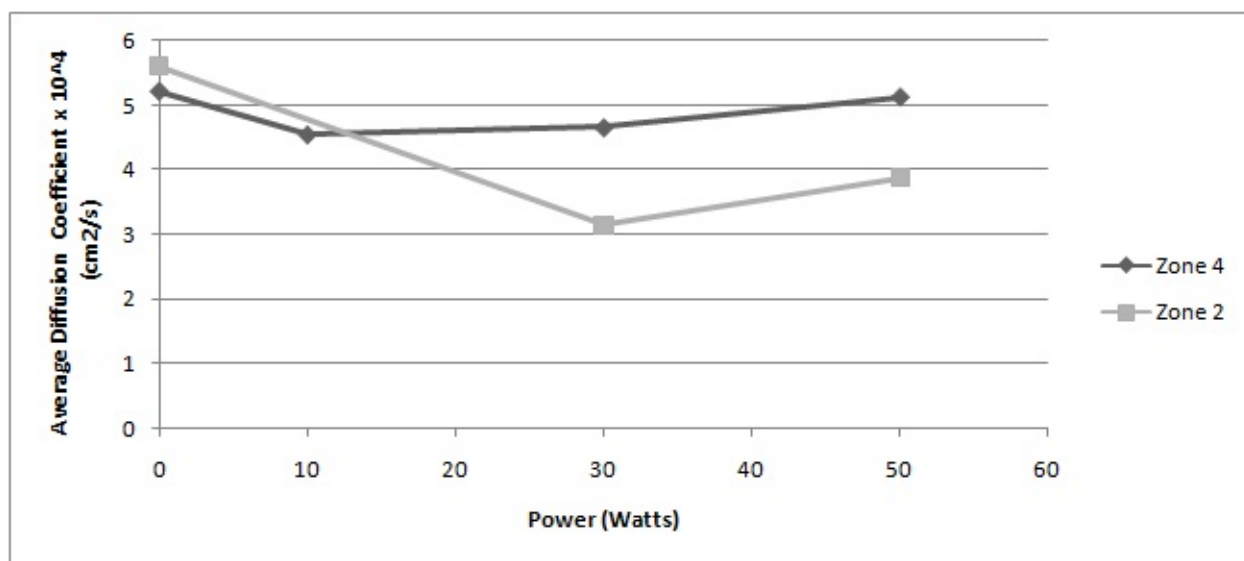


Figure 44 Average diffusion coefficient (D) versus power for Zones 2 and 4 of Sangrey's (2011) results.

Section 2: Modified Setup

As described in the previous chapter, the frequency of EM waves was chosen based on the validation of the COMSOL simulation according to the experimental electric field measurements. The simulated model was validated at a frequency of 65 MHz. Therefore, the tests were performed at this frequency.

Unstimulated Tests

After complete injection of the dye, small portions of the dye rise from the cup and then descend downward due to the dye density being slightly larger than that of water (1 gr/cm³). There is a relatively random time interval (5 to 12 minutes) between each time the dye rises out of the cup. However, approximately 1 hour past the start of the

experiment, this time interval decreases, and more continuous risings are observed. Figure 45 shows an example of the dye transport in an unstimulated test.

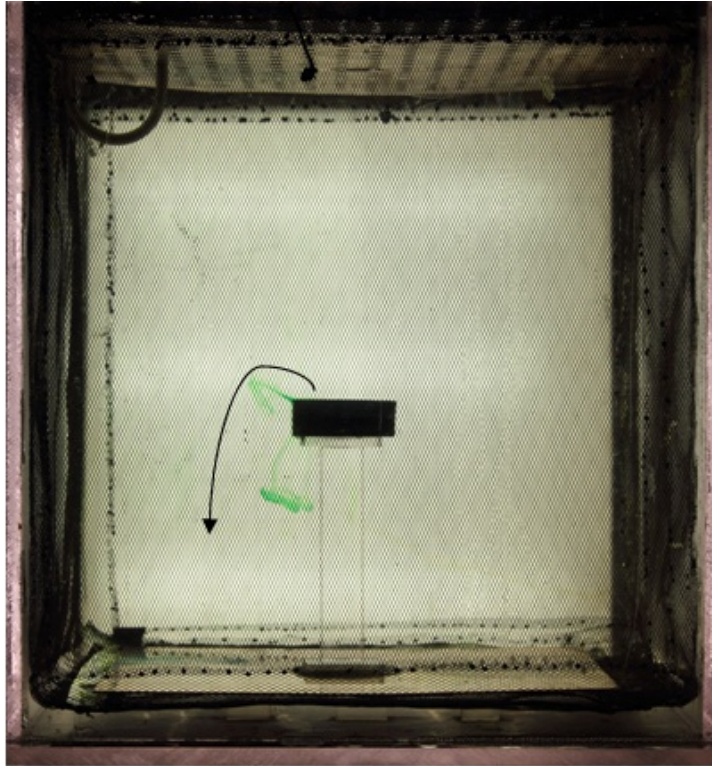


Figure 45 Dye transport during unstimulated test; dye randomly rises out of injection cup and descends.

Stimulated Tests

When the medium is electromagnetically stimulated at the frequency of 65 MHz, there is an upward flow of the dye. Portions of the dye rise out of the cup and move toward the top boundary of the resonant cavity. After reaching the top boundary, the dye spreads horizontally in random directions.

The stimulated experiment was performed at 10, 20, and 30 W to investigate the effect of the power level. As the magnitude of the power increases, the rate of the upward

flow of the dye increases. Figures. 46, 47, and 48 illustrate the flow of the dye 20 minutes after the dye injection at power magnitudes of 10, 20, and 30 W, respectively. As seen in Figures. 46, 47, and 48, with the increase in the applied power, larger portions of the dye flow upward.

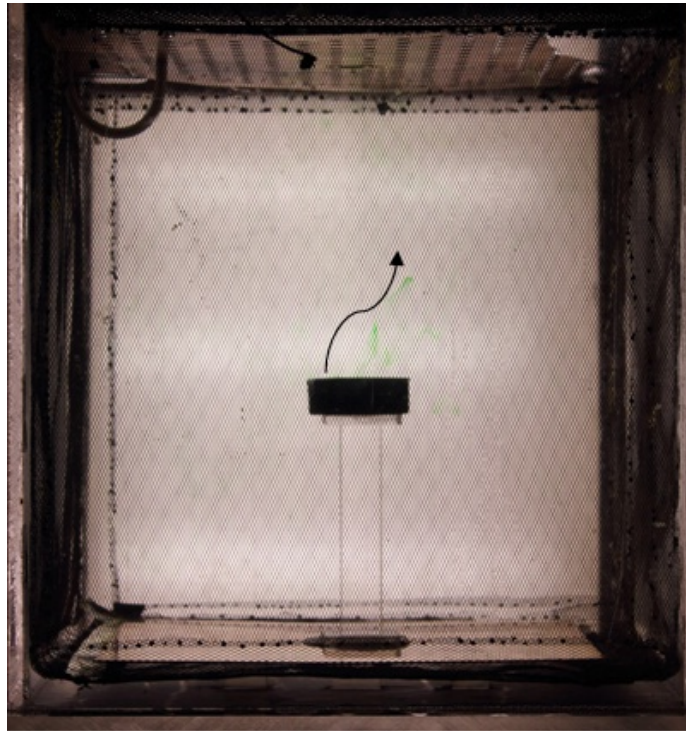


Figure 46 Dye flow in an EM-stimulated experiment at 65 MHz frequency and power level of 10 W at 20 minutes; dye rises out of injection cup toward top boundary.

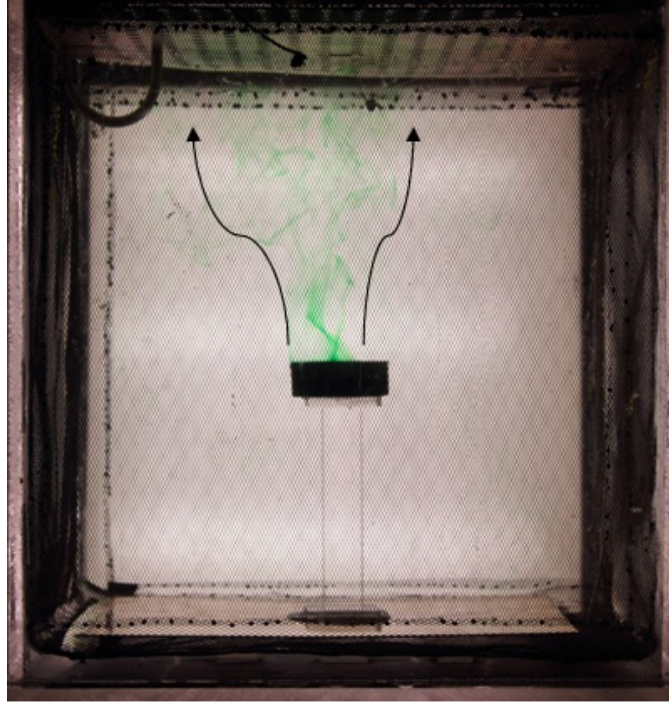


Figure 47 Dye flow in an EM-stimulated experiment at 65 MHz frequency and power level of 20 W at 20 minutes; dye rises toward top boundary at a faster rate compared to 10 W case.

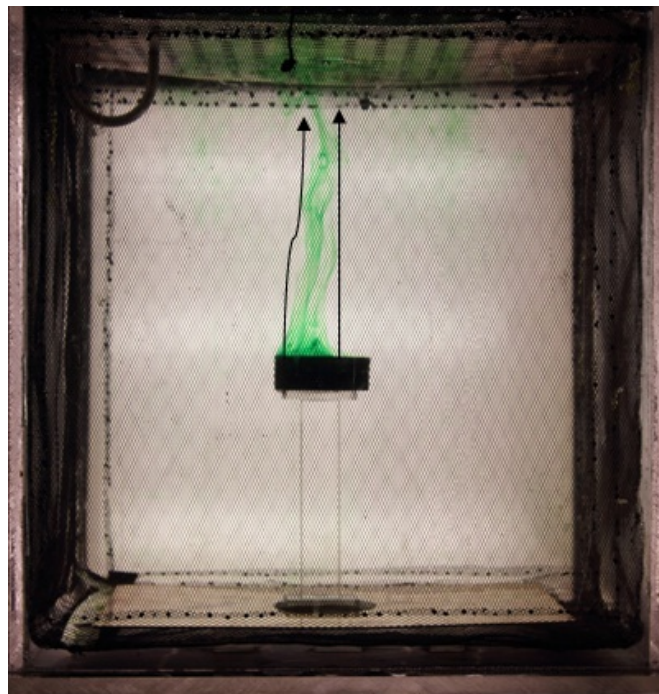


Figure 48 Dye flow in an EM-stimulated experiment at 65 MHz frequency and power level of 30 W at 20 minutes; dye rises out of injection cup toward top boundary at a faster rate compared to 10 W and 20 W cases.

Threshold Power- In order to find the threshold of power needed to electromagnetically induce the upward dye transport, the test started with no stimulation, and then the EM stimulation gradually started with an incrementally increasing power level. At each power level, the test was conducted for 1 hour, and the power was increased at 2 W increments by turning up the gain control on the amplifier. Thereafter, the test was again conducted for 1 hour. The one hour observation period for each power level was based on the results of the unstimulated test. Since after one hour of unstimulated tests the flow of the dye follows a more continuous pattern, 1 hour was chosen to be the waiting time to observe the effect of any power level on the dye flow. For each power level, the test continued for one hour, and if the dye flow resembled the unstimulated test during this period, the power was increased 2 W. This process continued until the upward flow of the dye was initiated. The upward flow of the dye started at a power of $P = 6$ W. However, at this power level, the dye did not travel all the way to the top boundary. The dye only moved half the distance to the top boundary and then spread around and downward. When the power is increased to $P = 8$ W, both upward and downward movements can be observed. However, the upward flow is clearly visible with rarely any downward flow at $P = 10$ W. As a result, $P = 6$ W is assumed to be the threshold to initiate a weak upward flow at the frequency of $f = 65$ MHz. However, $P = 10$ W is the necessary power threshold for a strong upward flow all the way to the top boundary at the frequency of $f = 65$ MHz.

Frequency Effect- Although only the 65 MHz simulated electric field was successfully validated against the experimental results, the experiment was repeated for other frequencies as well. Because of the strongly varying experimental field pattern

associated with these other frequencies, the choice of the frequency was based on the quality of impedance matching and, in turn, acquiring safe levels of (i.e., low) reflected power into the amplifier monitored by the spectrum analyzer. As a result, several tests were performed at 60, 69, 75, and 77 MHz at the RF power of 30W. Despite the tests performed at 65 MHz, during the stimulation at these other frequencies —except for 75 MHz— the flow of the dye was observed to be similar to the unstimulated tests. In other words, the stimulation had no apparent effect on the flow of the dye. At 75 MHz, however, after injection, the dye remained inside the cup for as long as the medium was stimulated. The test was repeated three times, and the results were consistent. Simulated electric field by COMSOL seems to confirm this according to a potential dielectrophoretic nature. However, the experimental electric field measurements showed no consistency with the simulation and created a random field pattern. Nevertheless, the result is noteworthy for future studies. It should be mentioned that the test performed at 75 MHz was repeated at 10W, 20W, and 30W and the dye remained inside the cup in all cases down to a power threshold of 3 W (when only the operate button on the amplifier was on and the gain nub on the amplifier was not used). Figures. 49 through 53 show the typical dye flow at 30 W power and the frequencies of 60, 65, 69, 75, and 77 MHz, respectively.

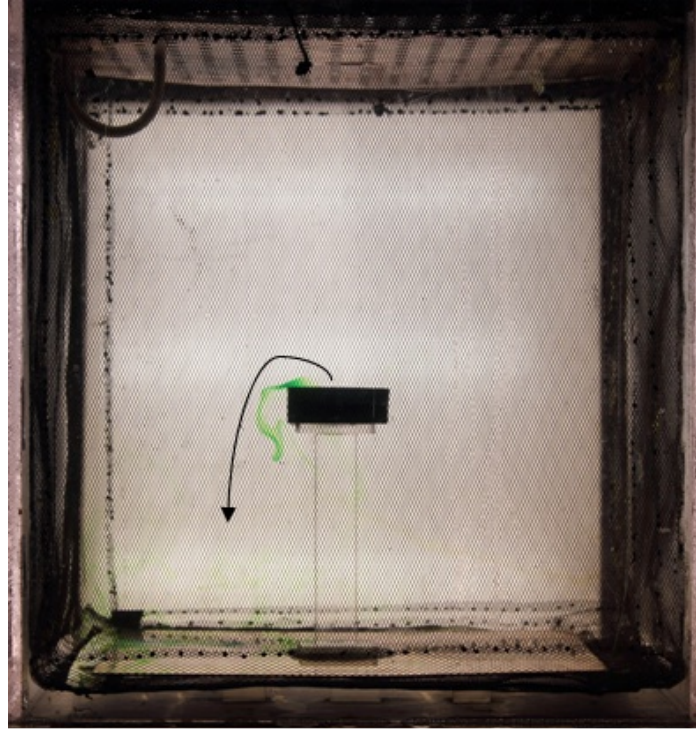


Figure 49 Dye flow in an EM-stimulated experiment at 60 MHz frequency and power level of 30 W; dye rises out of injection cup and descends toward bottom boundary similar to unstimulated tests.

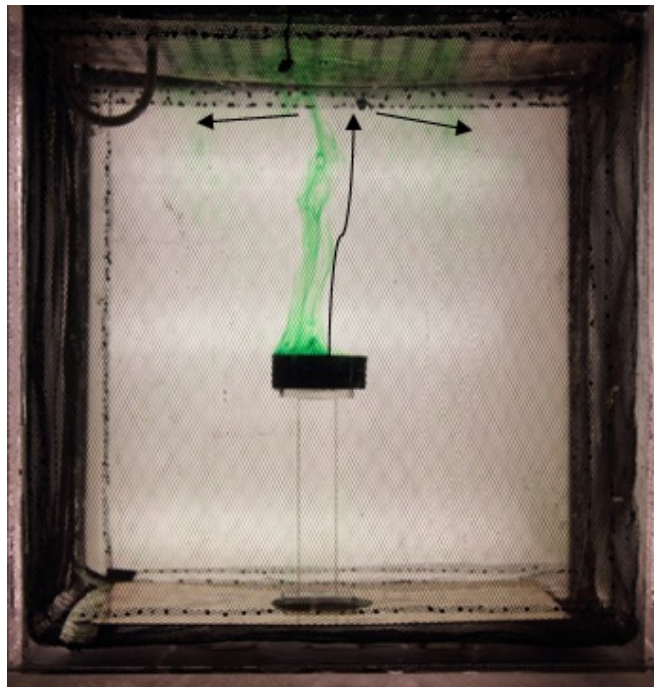


Figure 50 Dye flow in an EM-stimulated experiment at 65 MHz frequency and power level of 30 W; dye rises out of injection cup toward top boundary.

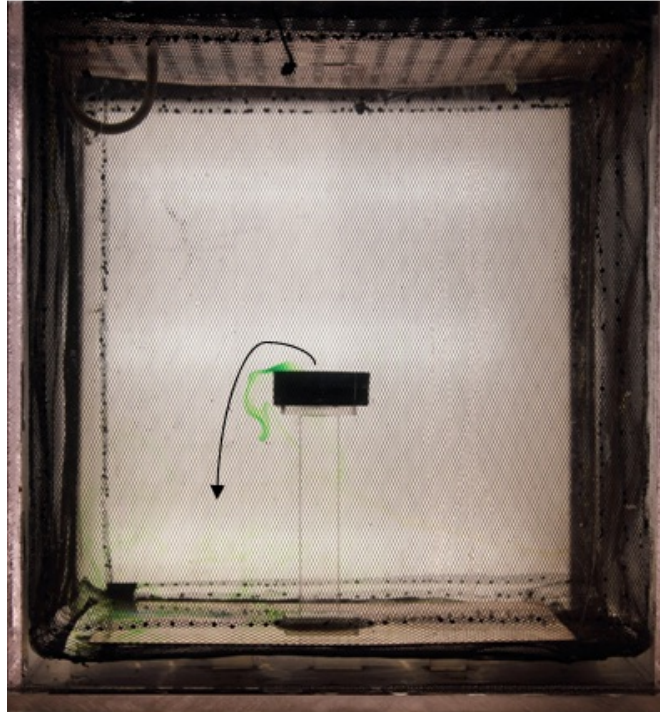


Figure 51 Dye flow in an EM-stimulated experiment at 69 MHz frequency and power level of 30 W; dye rises out of injection cup and descends toward bottom boundary similar to unstimulated tests.

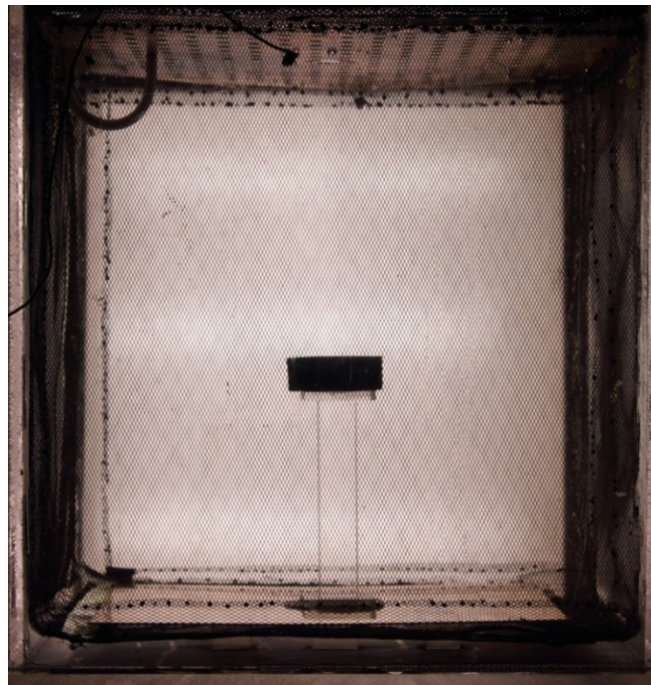


Figure 52 Dye flow in an EM-stimulated experiment at 75 MHz frequency and power level of 30 W; dye stays in injection cup as long as medium is stimulated.

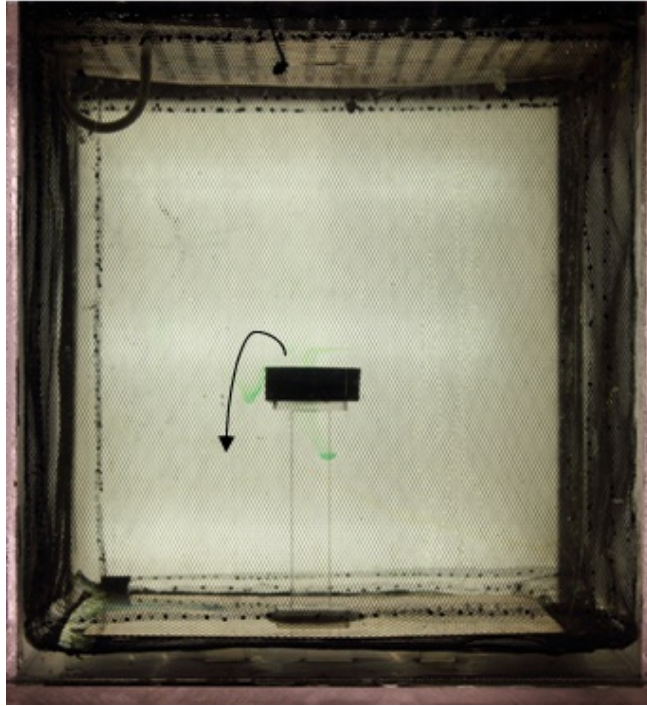


Figure 53 Dye flow in an EM-stimulated experiment at 77 MHz frequency and power level of 30 W; dye rises out of injection cup and descends toward bottom boundary similar to unstimulated tests.

Temperature Effects- In order to investigate the effect of temperature on the dye flow attributed to convection, the temperature of the water was recorded at different EM-stimulation frequencies for the highest input RF power of 30 W. Figure 54 shows the change of temperature over time for different frequencies at a distance of 1 cm from the center of the loop antenna. As expected and as seen in Figure 54, the temperature slightly increases for all the frequencies over time since the loop antenna heats up due to resistive heat generation. The maximum change in temperature is less than 1°C (less than 0.4°C in 20 minutes) for all frequencies. The same rise in the temperature is observed for all frequencies while the radiation pattern and dye flow are different at 65 MHz. This

suggests that the flow of the dye is not convective (i.e., due to the thermal effect or merely thermal effect) and is due to other phenomena related to the electromagnetic field.

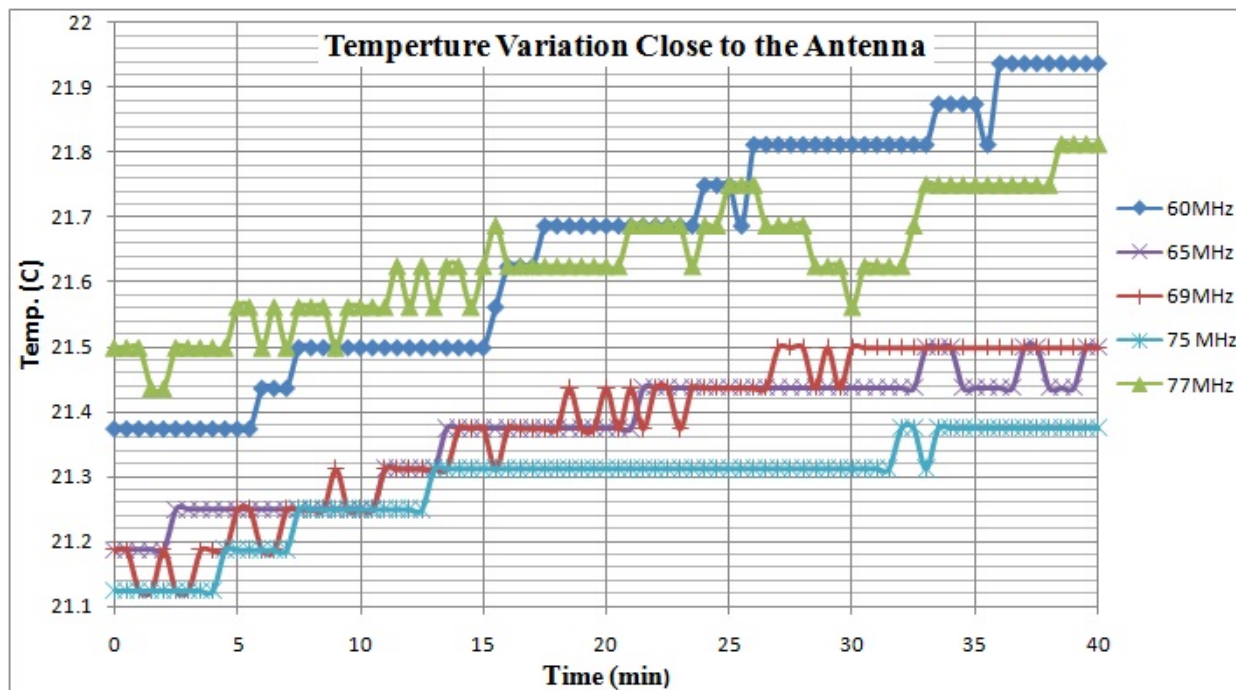


Figure 54 Change of water temperature 1 cm away from the center of the loop antenna at different frequencies over time for an RF power of 30 W.

Quality Factor Calculation- In order to have an understanding of the resonance condition for this setup, the quality (Q) factor of the resonant cavity is calculated based on the electric field data from the COMSOL simulation. The electric field magnitudes at several frequencies of a regular grid are exported into MATLAB. The exported data are averaged over the volume and plotted versus frequency. Figure 55 provides the plot of the average electric field magnitude versus frequency for the resulting data from the simulation of the modified experimental setup. According to Eqn. 22, the two peaks in Figure 55 are observed at the first two modes (TE_{110} and TE_{111}/TM_{111}) of the cavity at the

frequencies of 62 MHz and 75 MHz, respectively, with a significantly larger peak for the first mode.

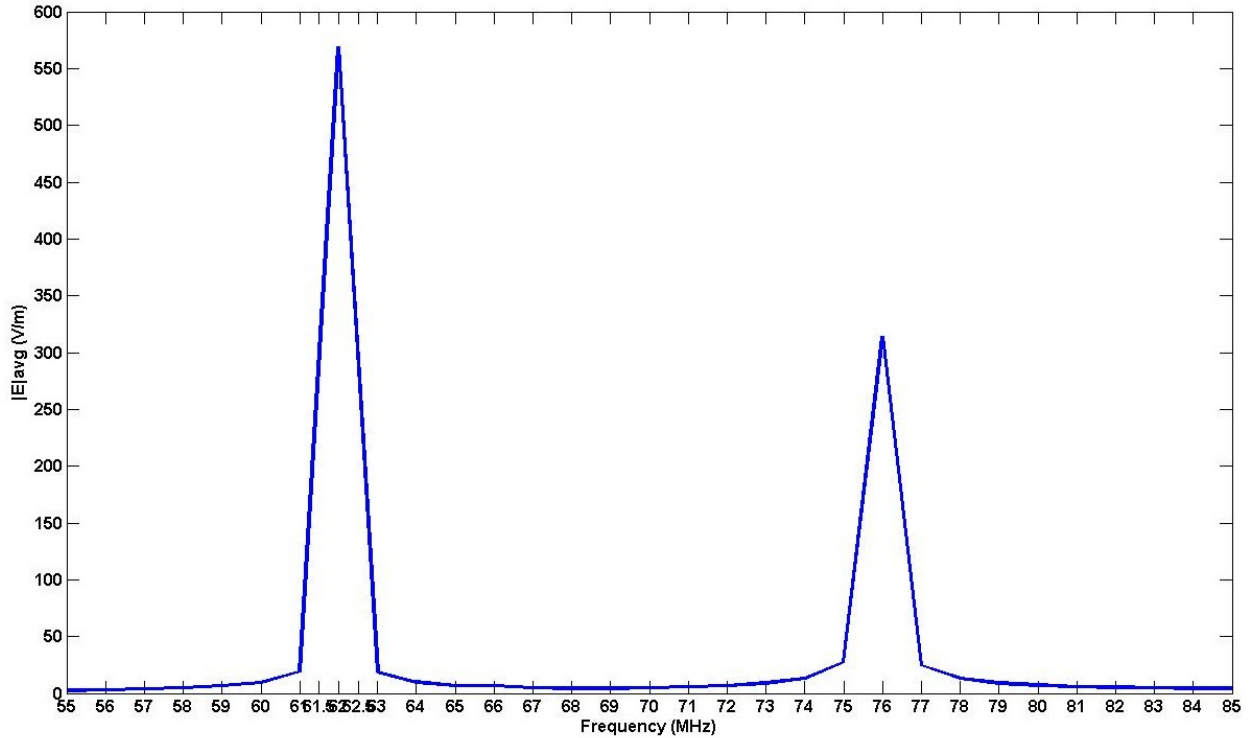


Figure 55 Plot of average magnitude of electric field over volume versus frequency for simulation data using COMSOL Multiphysics to represent quality factor (Q -value); two peaks occur at first two modes, TE_{110} and TE_{111}/TM_{111} at 62 MHz and 75 MHz, respectively in the ascending frequency order.

Using the simple method to calculate Q described in Chapter 2, the value of Q at 62 MHz is estimated as follows.

$$Q = \frac{f_0}{\Delta f} \approx \frac{62\text{MHz}}{2.5\text{MHz}} = 24.8 \text{ .}$$

According to Figure 55, the resonance occurs at 62 MHz. Considering the large dimensions of the resonant cavity and the high loss tangent of water, the obtained value of Q shows a satisfying resonance.

Field Pattern Effect- As described in Chapter 3, if dielectrophoresis is the controlling mechanism for the dye transport, a force should exist in the opposite direction of the gradient of the electric field squared ($\nabla|E|^2$). Because of the monotonically changing electric field (measured experimentally) at 65 MHz, this force is expected to be in the positive Z direction (upward) at and above the location of the injection cup within the medium. As shown previously for the 65 MHz case, the larger values of electric field occur at the bottom of the medium, and the magnitude of the electric field decreases from the bottom to the top. The measured electric field can be seen in Figure 24. Figure 56 shows an example of the experimentally measured electric field as well. While this figure shows only one of several slices, the field pattern is almost the same for all similar depth slices in the medium, meaning that except for the areas very close to the antenna, the maximum electric field occurs at the bottom of the medium, and the minimum electric field occurs at the top.

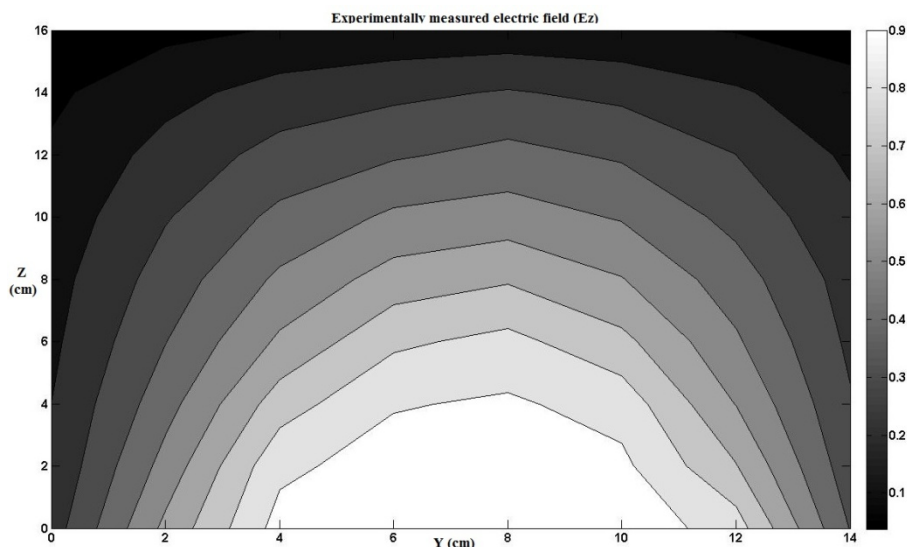


Figure 56 Map of experimentally measured electric field normalized to maximum electric field value in entire cavity, with maximum electric field at 65 MHz and 30 W of power.

As explained previously, because of the orientation of the measuring probe, the measured electric field is mostly the Z component. In other words, the monopole probe is vertically polarized (i.e., reception of a monopole antenna is always much stronger for the component of the electric field parallel to its orientation, in this case, Z component). In order to investigate whether dielectrophoresis is the controlling phenomenon, the study needs to be performed over other components of the electric field. For this purpose, the study is performed on the full 3D electric field vectors of the simulated electric field validated against the experimentally collected one. However, validation of the simulated field is only performed through a comparison between the only available measurement (E_z) and the simulated E_z . This approach is an acceptable practice for validation of the simulated electric field. The reason is the constrained relation between the three components of electric fields in a uniform, isotropic medium for a well-known antenna like a loop, monopole, or a dipole antenna, which enables prediction of two components if one is known.

Three matrices of the three components of the gradient of the electric field squared ($\nabla|E|^2$) vector are computed. However, because of the 2D format of the images, the Y component is redundant. The components of interest are only the X and Z components (first and third component in Eqn. 33). According to Eqn. 33, each of these components creates a dielectrophoretic force, which would potentially move the dye in the X and Z directions. The fact that the dye concentration at each node within digital images represents the concentration integrated over the Y-axis implies an integration of the force over the Y-axis as well. As a result, the X and Z components of the gradient of the electric field squared were integrated over the Y-axis. Although there are

dielectrophoretic forces in the Y direction as well, the flow of the dye in this direction cannot be observed in the acquired 2D digital images of this study.

According to Eqn. 26, a particle with a relative dielectric permittivity greater than that of the medium (water, ≈ 81) moves toward the positive field gradient and vice versa. As expected for most matters, the dye used in this experiment has a dielectric permittivity less than that of water. Thus, if dielectrophoretic forces are present, those forces should be in the direction of the negative gradient of the field squared ($-\nabla|E|^2$). Obtaining the direction of the $\nabla|E|^2$ vector, the direction of the dielectrophoretic forces can be predicted. Therefore, if the components of the $\nabla|E|^2$ vector are positive, the dielectrophoretic forces should be in the negative direction of the axes and vice versa. Figure 57 represents the contour map of the Z-component of the $\nabla|E|^2$ vector, and Figure 58 represents that of the X-component of the $\nabla|E|^2$ vector as obtained from the code (script: m-file) developed in MATLAB (see Appendix D).

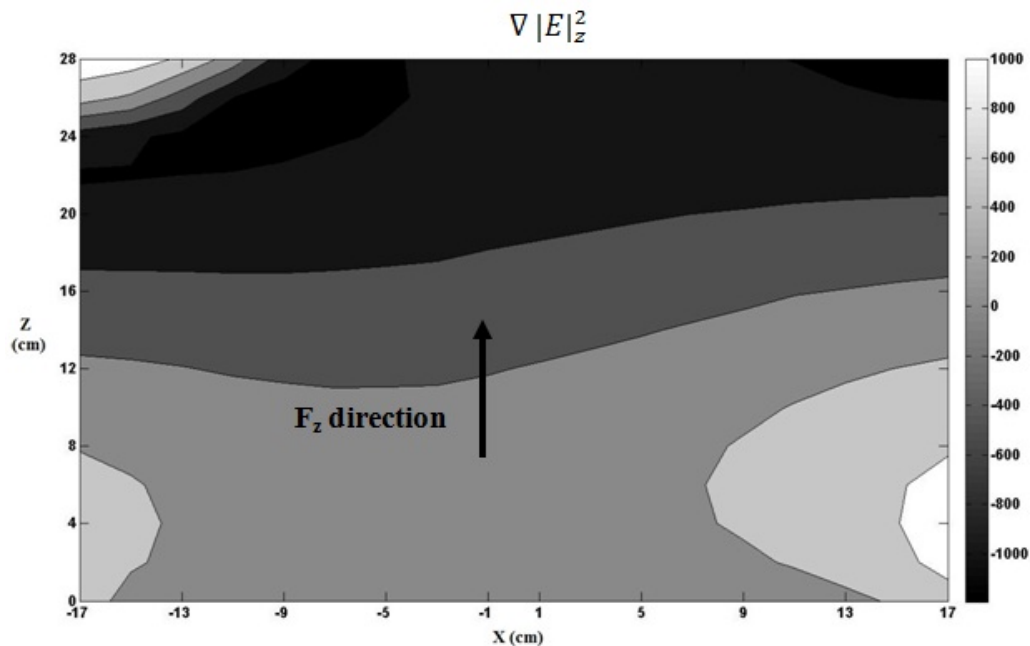


Figure 57 Contour map of Z-component of $\nabla|E|^2$ (V^2/m^3) according to COMSOL Multiphysics results at 65 MHz.

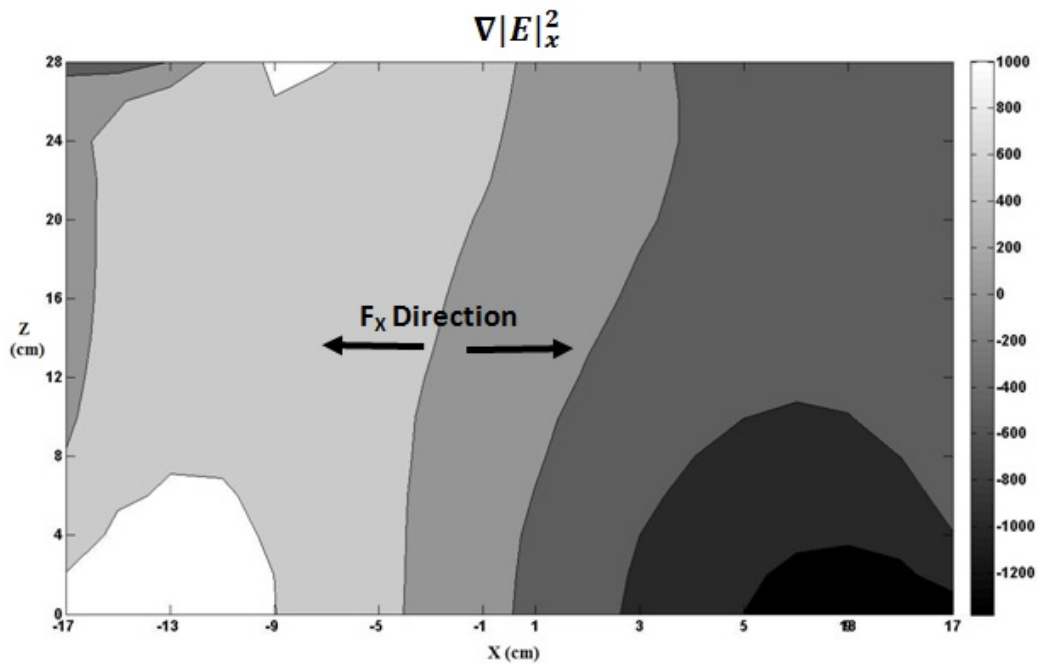


Figure 58 Contour map of X-component of $\nabla|E|^2$ (V^2/m^3) according to COMSOL Multiphysics results at 65 MHz.

According to Figures. 57 and 58, the Z-component of $\nabla|E|^2$ is negative with an increasing magnitude toward the top. As a result, because of smaller dielectric constant of dye compared to that of water, the direction of the dielectrophoretic forces are in the positive Z-direction (i.e., upward) at 65 MHz. This result is in agreement with the results from the experimental field investigation as well.

On the other hand, the X-component of the $\nabla|E|^2$ vector creates a force that drags the dye toward the side walls of the cavity. However, the magnitude of the forces in the X direction is almost $\frac{1}{2}$ of the magnitude of the vertical forces. As a result, the upward flow of the dye dominates the horizontal flow. In fact the horizontal flow appears to dominate after the dye reaches near the top boundary, and the upward flow has slowed or stopped. Since the dye has a flow in both right and left directions after it reaches the top boundary, the observed flow can be interpreted as a mix of dielectrophoresis and diffusion.

Digital Analysis and Evaluations- In order to study the effect of the applied RF frequency and power on the dye flow, two sets of studies on the digital image pixel intensities were performed. In the first study, "Pixel Intensity Summation," the sum of the pixel intensities in a region referred to as the "upper zone" is evaluated (for more information, see Chapter 3). The pixel intensity data are adjusted in a way that lower values of the pixel intensities refer to brighter pixels or pixels with less amounts of the dye. As a result, a comparison of the summation of pixel intensities for the tests can be performed to evaluate the variations of the total amount of dye that leaves the injection cup upward into the upper zone. A code (*m.file*) is developed in MATLAB to analyze the sum of pixel intensities, which is presented in Appendix E.

The summation is performed on the set of the experiments performed at 65 MHz (10 W, 20 W, and 30W) as well as for the test performed at 75 MHz (30 W) and the unstimulated test. Figure 59 shows the plot of the summation of pixel intensities over time for these tests.

As described previously, no dye transport was observed for the tests performed at 75 MHz. It is, therefore, expected that the summation of pixel values for this test to be constant over time. However, the plot shows some variation over time attributed to the errors associated with this method of evaluation.

Because the movement of the dye in the unstimulated test is mostly downward, not much dye enters the upper zone. As a result, the amount of the dye entering this zone is not large enough to overcome the error values. Although the dye transport for the 65 MHz case at 10 W is upward and thus into the upper zone, the amount of the dye flowing into this zone is not enough to overcome the errors associated with this method of evaluation. Hence, the same argument is valid for the stimulated test of 65 MHz at 10 W as well where the background noise is dominant. In summary, the change of the sum of pixel intensities over time for the unstimulated test, stimulated test at 75 MHz (30 W with power), and 65 MHz (with a power less than 10W) follow the same pattern.

The plot of pixel values over time for the stimulated tests of 65 MHz at 20 W and 30 W, however, shows different results. As seen in Figure 59, the change of this summation over time is larger compared to 10 W case. The sum of adjusted pixel intensities increases over time for these two tests, meaning pixels become darker. This refers to the presence of more dye in the upper region.

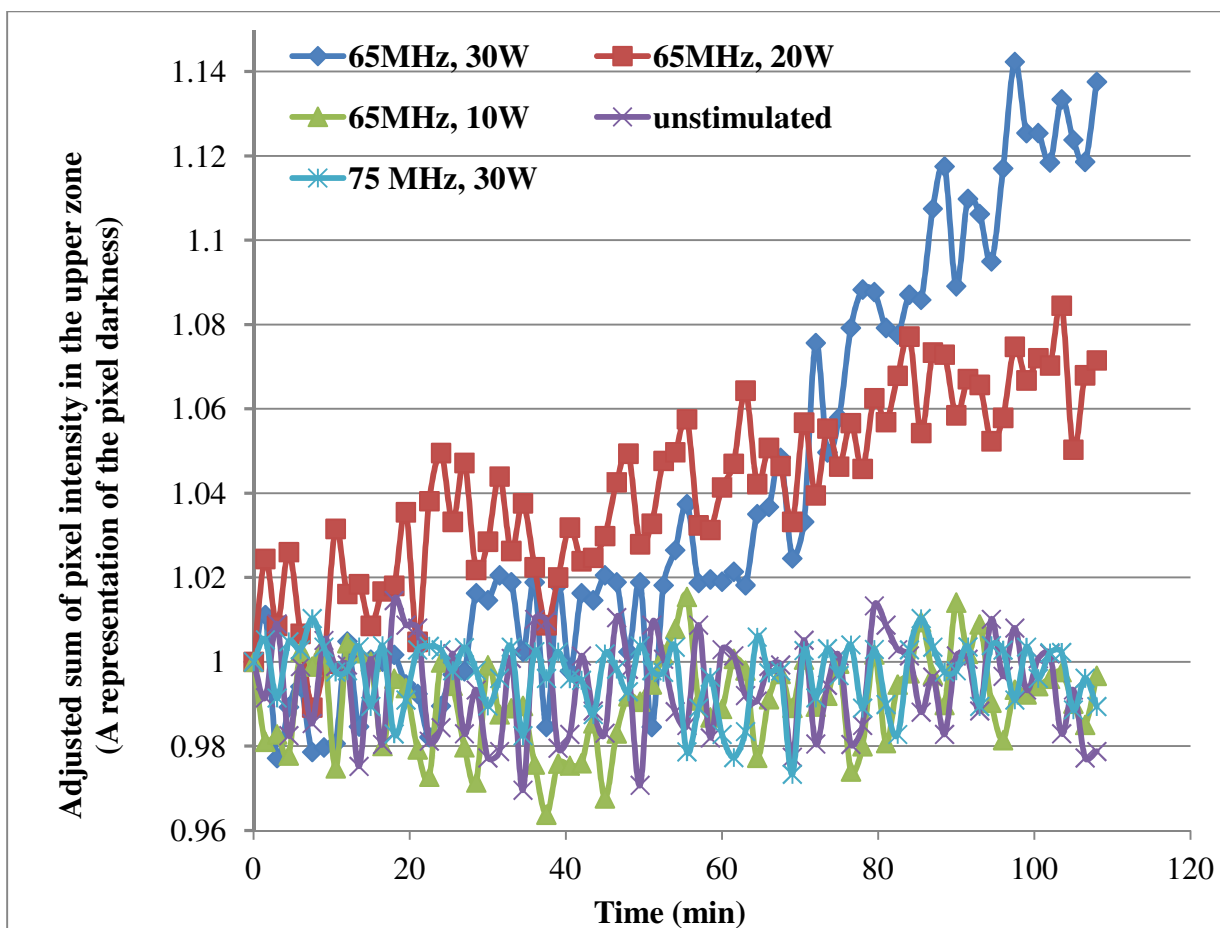


Figure 59 Plot of adjusted sum of image pixel intensities (representing transported dye amount) vs. time for unstimulated test, three stimulated tests at 65 MHz at power levels of 10 W, 20 W, and 30 W as well as a stimulated test at 75 MHz and 30 W; summation is performed over upper zone in digital images.

In order to quantify the variations in the sum of pixel values over time for each test, the relative change (%) of the summation is also calculated. Therefore, the last three datasets ($t=105$ min., $t=106.5$ min., and $t=108$ min.) are averaged and subtracted from the initial dataset ($t=0$) of the curves of Figure 59. The relative change (%) was calculated and plotted versus power shown in Figure 60. This value is almost the same for the unstimulated test, the stimulated tests at 75 MHz, and the stimulated test at 65 MHz at 10 W. However, the relative change increases rapidly for the stimulated tests of

65 MHz at 20 W and 30 W power levels. The value of this variation at 30 W is almost twice as large as that of 20 W.

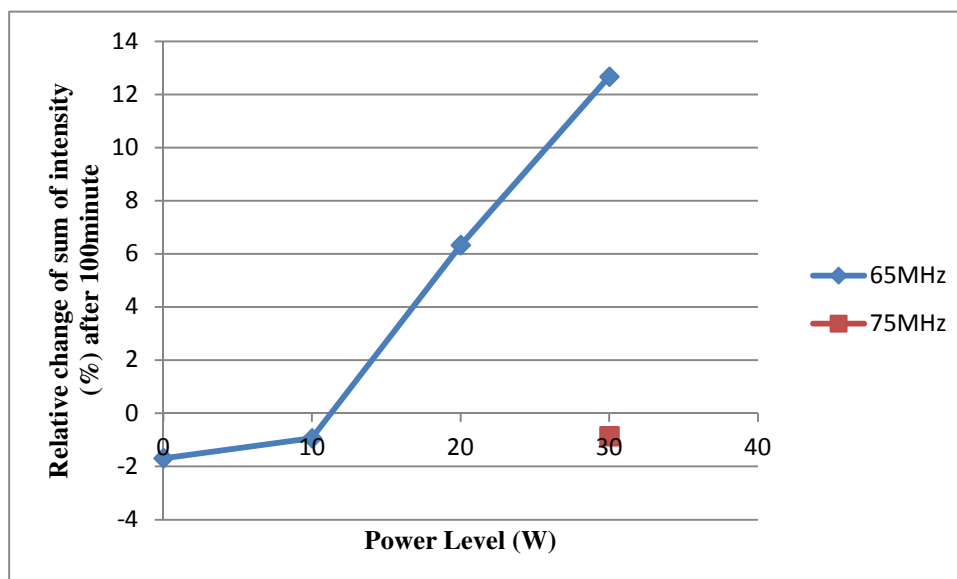


Figure 60 Plot of adjusted sum of pixel intensities (representing transported dye) vs. power for unstimulated test, three stimulated tests at 65 MHz and 10 W, 20 W, and 30 W, and stimulated test at 75 MHz and 30 W; summation is performed over upper zone in digital images.

A “finger width” study is the second set of studies that are performed on the digital images to evaluate the characteristics of the dye fingers as the dye moves upward at 65 MHz. The purpose of this study is to investigate the effect of the power level on the shape of the dye fingers (specifically the vertical profile of the finger width). A finger zone is defined based on the number of pixel intensity above a visually selected threshold (i.e., with the amount of dye above a visually selected dye concentration, for more information see Chapter 3). In other words, a finger zone is defined (see Chapter 3), and the number of pixels that contain more dye (i.e., pixels with negative values after being subtracted from the background pixels value) is calculated along the vertical (Z) axis for

this zone. The threshold pixel intensity is defined in the MATLAB code (*m.file* of Appendix F) that can separate the pixels containing enough dye to represent a finger compared to other pixels. The number of pixels containing enough dye to represent a finger is counted for various points along the vertical (Z) axis in the finger zone. This number is summed over time and is plotted versus height in Figure 61. The horizontal axis shows the number of pixels that are assumed to contain dye. The vertical axis represents the distance from the injection cup in the vertical direction. Thus, an elevation profile (i.e., width of fingers versus elevation) of the accumulated-over-time finger width is computed for 10 W, 20 W, and 30 W power levels at 65 MHz and shown in Figure 61.

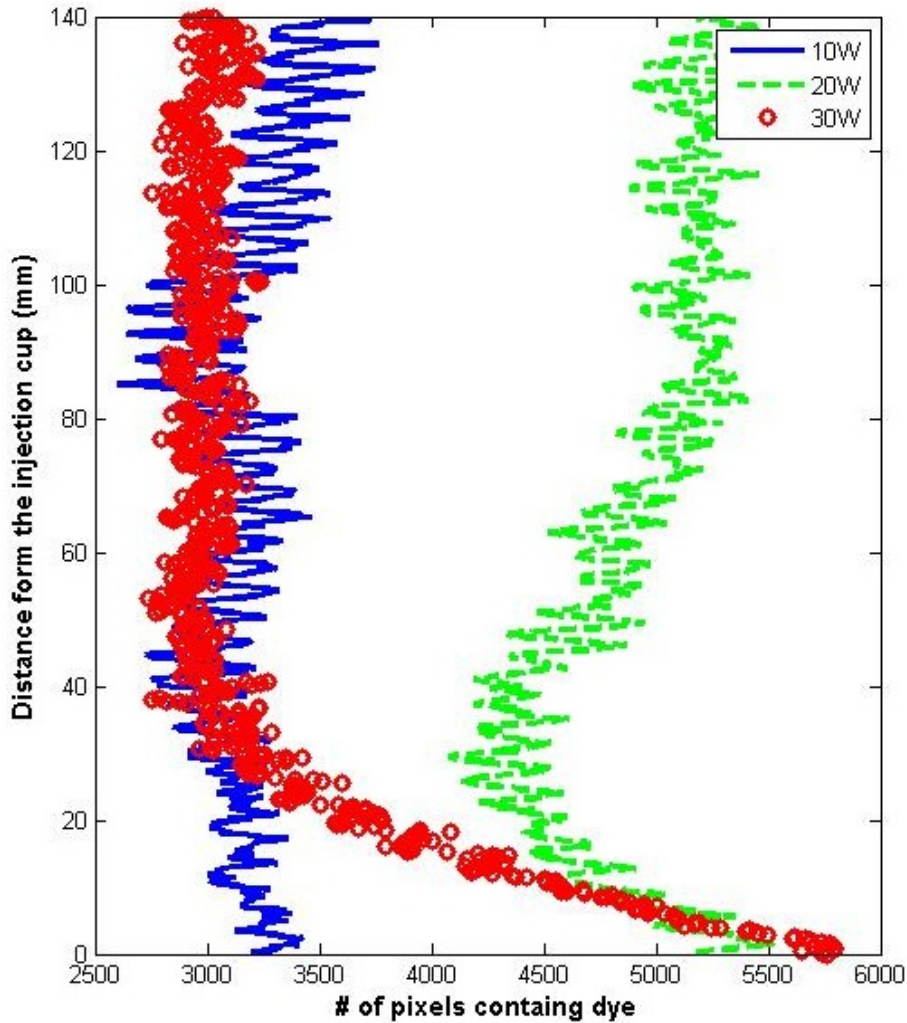


Figure 61 Plot of total of number of pixels containing enough dye to be considered a finger (representing width of the dye finger) accumulated over time vs. vertical distance above injection cup.

As shown in Figure 61, the finger width (i.e., the number of pixels containing enough dye to be considered a finger) for the test performed at 65 MHz and 10 W is almost constant over height and is always smaller than this number for 20 W and 30 W power levels.

For the 20-W case, the finger width is almost constant over height as well. However, the finger width is larger than that for the 10-W case. This is representative of a

more concentrated upward dye flow compared to the 10-W case that is not focused and disperses gradually.

For the test at 30 W, the plot shows totally different results. The number of pixels containing enough dye to be assumed a finger decreases rapidly with the increase of the vertical distance from the injection cup. Observing the pictures associated with this test reveals that a much darker fingers at this power level tend to move faster and in a more straight, focused, and robust shape. The fingers of this test are narrower but at the same time contain more dye. As a result, although the total number of pixels containing the finger becomes smaller, the sum of the concentration of the dye within the narrower finger region is much higher.

CHAPTER FIVE: CONCLUSION

This research is the first step to reach the first objective of the investigation of the effect of EM stimulation on transport mechanisms. The data clearly show that the use of EM stimulation does affect the dye flow through water.

Stimulating Effects

The previous work performed by Sangrey (2011) at 154 MHz and the work performed here with the modified experimental setup prove that the dye flow is altered and directed by the electromagnetic stimulation of the medium. The antenna design and, hence, radiation pattern are keys determining the effect on transport mechanisms. For the horizontally polarized, L-shaped antenna used in Sangrey's experiment (2011), the dye was transported toward the tip of the antenna after descending out of the injection cup. For the loop antenna used in the modified experiment of this work at 65 MHz, however, the dye rises out of the injection cup upward. The reason is that each antenna design and operating frequency creates a specific electric field pattern that can affect the dye flow differently. Since there was minimal temperature gradient measured within the medium ($< 1^{\circ}\text{C}$) and because of the inconsistent flow pattern compared to any potential convective flow due the heat source (antenna), the transport mechanism is believed to have been mostly controlled by the EM stimulation and not by a strong convective flow.

Effects of Power Level

The quantitative analysis of Sangrey's work (2011) by the author proves that the rate of transport is affected by the EM power level. Utilizing the diffusion coefficient as a representative of the transport rate shows that the flow rate increases with the increase of power level. Special attention should be paid to the application of the diffusion equation only to regions where the diffusion phenomenon can be the dominant flow mechanism (i.e., where viscous fingers do not exist or within stable fingers).

Modified Experimental Setup

In an attempt to find the relationship between EM stimulation and dye concentration in Sangrey's work (2011), the need for a modified experimental setup was clear. In this work, a modified setup was created that can help correlate the electric field characteristics to the dye transport by providing a monotonically changing pattern of electric field intensity.

The modified experimental setup used a water-filled, loop-coupled, resonant-cavity as the testing medium. A loop antenna is used to launch RF waves into the cavity. The resonant cavity prevents any interference from the surrounding medium while generating a strongly focused electric field inside the medium. An injection cup was placed close to the center of the medium for the initial containment of the dye after injection. If the medium is not stimulated by the electromagnetic waves, the dye will rise out of the cup and randomly descend toward the bottom of the medium.

However, the EM-stimulation effects on the medium were demonstrated at a frequency of various frequencies. At a frequency of 65 MHz, the dye moves towards

the top boundary of the medium with its flux increasing as a function of the input EM power. The experiment was performed at 65 MHz and at different power levels of 10 W, 20 W, and 30 W. The rate of dye flow was greatly increased with the increase in the EM power.

The stimulation was also repeated for the frequencies of 60, 69, 75, and 77 MHz. The results showed that except for $f = 75$ MHz, the dye flowed similar to the unstimulated test. At 75 MHz, however, the dye was contained inside the cup so long as the medium was stimulated by a power larger than 3 W. This result could be explained by the simulated electric field pattern and the resulting dielectrophoretic force. However, the simulated electric field at this frequency could not be validated since it did not match the experimentally measured electric field.

Temperature Effect

In this study, the temperature of the medium was monitored at different frequencies of EM stimulation (60, 65, 69, 75, 77 MHz) at the RF power level of 30 W at a location 1 cm away from the center of the loop antenna where maximum heat is expected to be generated. The temperature variation for all frequencies followed the same pattern. However, only at the frequency of 65 MHz, the upward dye flow was generated. The study, therefore, proves that the small temperature increase within the medium and convective flow is not the reason for the rising dye. In addition, the containing effect for the 75 MHz case explicitly refutes any convective flow effect. Thus, the dye flow is believed to be controlled by the electromagnetic stimulation rather than temperature variations (i.e., convection).

Dielectrophoresis Study

Because the dye used in the experiment is nonreactive and electrically inert, the most likely controlling factor for the dye transport could be dielectrophoresis. As expected for most material, the dye used in this experiment has a dielectric constant less than that of water ($\epsilon_{water} = 81$). Hence, if dielectrophoretic forces are present, they should be in the direction of the negative gradient of the electric-field-squared (i.e., toward regions of lower electric field intensity and, hence, lower EM power density). The use of an organized (i.e., monotonically increasing in one direction) electric-field radiation pattern within the resonant cavity helped make the investigation of dielectrophoresis possible.

The upward flow of the dye in the 65 MHz case can be due to the dominant, upward dielectrophoretic force. For the 65 MHz case, results are consistent with both the experimental (obtained by probing) and simulated electric-field patterns (simulated using COMSOL Multiphysics). The containment of the dye in the injection cup in the 75 MHz case can also be due to the dominant, downward dielectrophoretic force. For the 75 MHz case, results are consistent with only simulated electric-field patterns obtained by simulation of the electric field using COMSOL Multiphysics.

In the horizontal direction, dielectrophoretic forces are smaller than those in the vertical direction. The directions of these forces are toward the side walls of the box. The experimental dye flow is also in agreement with these results. Because the forces are stronger in the vertical direction, the dye flows upward. Then, the dye starts to disperse toward the sides of the medium due to the horizontal dielectrophoretic and

diffusion forces, after the dye reaches the top boundary. It is noteworthy that the space near the top boundary is where there is no room for the vertical movement or where the vertical component of the dielectrophoretic force is less dominant compared to the horizontal component. As a result, dielectrophoresis along with diffusion can be the mechanisms contributing to the transport of the horizontally dispersing dye.

Digital Analysis

Although the existence of the copper mesh, acting as the boundary of the resonant cavity, distorts acquired digital images and does not allow any calibration of these images to the dye concentration, several studies are performed on the raw data of the digital pictures for the 65 MHz cases. These raw values are in fact the pixel intensities, which are nonlinearly—and spatially variable—related to the dye concentration. The results from these studies cannot lead to an exact quantitative analysis of the concentration but are the only quantitative representatives of the dye flow.

Image Pixel-Intensity Summation

In the study performed on the pixel values referred to as “Pixel-Intensity Summation,” the sum of the pixel values within a rectangle zone containing the region above the injection cup is calculated. The results show that this value substantially increases over time by increasing the power level applied at 65 MHz.

Finger-Width Profile

In another study, the vertical profile of the finger width and the shape of the rising finger for the experiments performed at 65 MHz are analyzed. The results show that the width of the fingers increases when the power is increased from 10 W to 20 W. However, when the power is raised to 30 W, the width decreases rapidly after rising a small distance above the injection cup. The width is larger at the vicinity of the injection cup, but smaller at all other locations. This is due to the fact that as power increases more dye moves upward causing the fingers of the 20 W case to be wider than the 10 W case. However, at 30 W, even though the amount of the dye leaving the cup is even more, the fingers are more vertically-directed and focused due to the strong dielectrophoretic force compared to diffusion. This results in wider fingers at 20 W and narrower, but darker, more concentrated fingers at 30 W.

Conclusion

This thesis is a first step in the study of the effects of EM waves on the improvement of air sparging in saturated media. The contributions of this work to the hypothesis presented in the thesis are listed below.

- EM waves can control the flow in saturated media.
- The Antenna design is a key factor in controlling the direction of the flow.
- The rate of transport increases by the increase in the EM power level launched into the medium.
- The similar temperature change pattern at the vicinity of the antenna—expected to be the closest point to the heat source—for different values of frequencies in the

setup presented in here suggests that the change of the temperature and convection are not dominant factors controlling the flow.

- The dielectrophoretic studies are in agreement with the flow pattern. As a result, dielectrophoretic forces can be the dominant factor behind the EM stimulation of the flow.

Correlating the electric field/power with the dye transport rate requires more analysis. This work is a good basis for continuing research into the mechanism creating the effects observed in this study. The experience gained and methods developed in this work can be modified and improved in future studies. It is suggested that for future studies, transparent, electrically conductive sheets be used for resonant cavity construction. This would enable better digital visual analysis and calibration of digital images to the dye concentration. It can also be helpful to prepare a creative setup that would allow a uniform dye flow without any viscous finger creation to better study pure diffusion. The existence of the viscous fingers prevents numerical analysis of the dye diffusion due to the semi-random, complicated nature of fingering.

REFERENCES

- Balanis, C. A., 1989, *Advanced Engineering Electromagnetics*, first Edition, John Wiley & Sons, New York.
- Benner, M. L., Mohtar, R. H., and Lee, L. S., 2002, "Factors affecting air sparging remediation systems using field data and numerical simulations," *Journal of Hazardous Materials*, B95 pp.: 305–329
- Braida, W. and Ong, S. K., 2001, "Air sparging Effectiveness: Laboratory Characterization of Air-channel Mass Transfer Zone for VOC Volatilization," *Journal of Hazardous Materials*, B87, pp. 241-258.
- Brown, R.G., Sharpe, R.A., Hughes, W. L., and Post, R.E., 1973, *Lines, waves, and antennas, the transmission of electric energy*, Second Edition, John Wiley & Sons, New York.
- Chao, K. P., Ong, S. K., and Protopapas A., 1998, "Water-to-air mass transfer of VOCs: laboratory-scale, air sparging system," *Journal of Environ. Eng.*, Vol. 124, No. 11, pp. 1054-1060.
- Cussler, E. L., 1997, *Diffusion, Mass Transfer in Fluid Systems*, Second Edition, Cambridge University Press, United Kingdom.
- Dey, S. and Mirra, R., 1998, "Efficient Computation of Resonant Frequencies and Quality Factors of Cavities via a Combination of the Finite-Difference Time-Domain

- Technique and the Padé Approximation,” *IEEE Microwave and Guided Wave Letters*, Vol. 8, No. 12, pp. 415- 417.
- Domenico, P. A. and Schwartz, F. W, 1997, *Physical and Chemical Hydrogeology*, Second Edition, John Wiley & Sons, New York.
- Hilhorst, M. A., 1998, *Dielectric Characterization of Soil, Doctoral Dissertation*, Wageningen Agricultural University, Wageningen, The Netherlands.
- Johnson, R. L., Johnson, P. C., McWhorter, D. B., Hinchee, R. E., and Goodman, I., 1998, “An Overview of In situ Air Sparging,” *Journal of Groundwater Monitoring and Remediation*, Vol. 13, Issue 4, pp. 127-135.
- Lee, C. S., Lee, S. W, and Chuang, S. L., 1985, “Plot of modal field distribution in rectangular and circular waveguides,” *IEEE Trans. Microwave Theory Tech.*, Vol. MTT-33, pp. 271- 27.
- Marley, M. C., Droste, E. X., and Bruel, C. J., 1996, “Use air sparging and vapor extraction to remediate subsurface organics,” in *E: Wastewater and groundwater Treatment*, <Online at <http://www.globalspec.com/reference/9391/349867/use-air-sparging-and-vapor-extraction-to-remediate-subsurface-organics>, last accessed October 2011>
- Mokkapati, V.R.S.S., 2011, *Micro and Nanofluidic devices for single cell and DNA analysis*, PhD thesis, Bangalore University, India, April, <Online at <http://repository.tudelft.nl/view/ir/uuid:7cf3908d-62de-402b-9551-c83c5239b003/> >

- Price, S. L., Kasevich, R. S., Johnson, M. A., Wilberg, D., and Marley, M. C., 1999, "Radio Frequency Heating for Soil Remediation," *Journal of the Air and Waste Management Association*, Vol. 49, pp. 136-145.
- Sangrey, H .D. O, 2011, *EM stimulation of water for geotechnical applications*, MS Thesis, Boise State University, Boise, May, Print.
- Suthersan, S. S. and Raton, B., 1999, "IN SITU Air SPARGING, Remediation engineering, design concepts", CRC Press LLC < Online at <http://www2.bren.ucsb.edu/~keller/courses/esm223/SuthersanCh04AirSparge.pdf> >.
- U.S. Geological Survey (USGS), 2005, Water Science for Schools data available on the World Wide Web (Groundwater use in the United States), online at < <http://ga.water.usgs.gov/edu/wugw.html>, last accessed July 2012 >
- Vermeulen, F. and McGee, B., 2000, "In-situ Electromagnetic Heating for Hydrocarbon Recovery and Environmental Remediation," *Journal of Canadian Petroleum Technology*, Vol. 39, No. 8, pp. 25-29.
- Yegian, M. K., Eseller-Bayat, E., Alshawabkeh, A., and Ali, S., 2007, "Induced Partial Saturation for Liquefaction Mitigation: Experimental Investigation," *Journal of Geotechnical and Geoenvironmental Engineering, ASCE*, Vol. 133, No. 4, pp. 372-380.

APPENDIX A

Simulation of Sangrey's (2011) Experimental Setup in COMSOL Multiphysics

Simulation of Sangrey's (2011) Experimental Setup in COMSOL

Multiphysics

Modeling Instruction:

MODEL WIZARD

- 1 Go to the **Model Wizard** window.
- 2 Click **Next**.
- 3 In the **Add physics** tree, select **Radio Frequency>Electromagnetic Waves, Frequency Domain (emw)**.
- 4 Click **Next**.
- 5 Find the **Studies** subsection. In the tree, select **Preset Studies>Frequency Domain**.
- 6 Click **Finish**.

GLOBAL DEFINITIONS

To help in creating the geometry, define some parameters defining its dimensions.

Parameters

- 1 In the **Model Builder** window, right-click **Global Definitions** and choose **Parameters**.
- 2 In the **Parameters** settings window, locate the **Parameters** section.
- 3 In the table, enter the following settings:

Table A.1 List of parameters used for modeling

Name	Expression	Name	Expression	Name	Expression
D_1	2[mm]	L_3	7[cm]	b_4	49[cm]
D_2	7[mm]	a	38[cm]	b_5	52[cm]
D_3	7[mm]	d	19[cm]	b_6	69[cm]
D_4	10[mm]	b_1	68[cm]	t	0.3[m]
L_1	8[cm]	b_2	32[cm]	f	154[MHz]
L_2	1.5[cm]	b_3	97[cm]		

Note that as long as you specify the unit in a bracket in the table, you can use different dimensions for length. A schematic of the geometry is shown in Figure A1 to provide a better understanding of the introduced parameters.

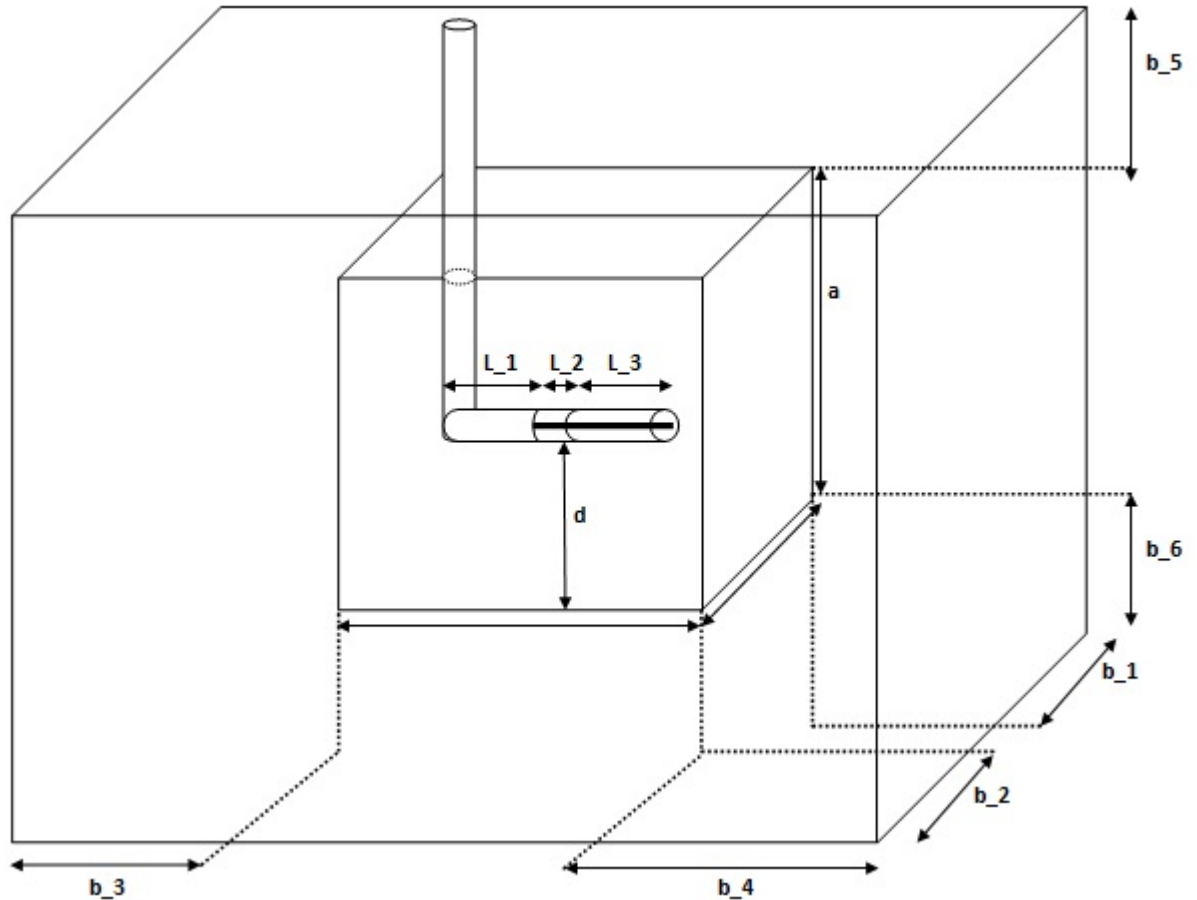


Figure A.1 Schematic of experimental setup of Sangrey (2011).

G E O M E T R Y 1

Cylinder 1

1 In the **Model Builder** window, under **Model 1**, right-click **Geometry 1** and choose **Cylinder**.

2 In the **Cylinder** settings window, locate the **Size and Shape** section.

3 In the **Radius** edit field, type $D_3/2$.

4 In the **Height** edit field, type $a-d+D_3/2+b_5+.02-.007$.

5 In the **Position** edit field, type $x:-L_1$, $y: 0$, $z: d+D_3/2$.

5 In the **Axis** edit field, type $x: 0$, $y: 0$, $z: 1$.

Cylinder 2

1 In the **Model Builder** window, under **Model 1**, right-click **Geometry 1** and choose **Cylinder**.

2 In the **Cylinder** settings window, locate the **Size and Shape** section.

3 In the **Radius** edit field, type $D_3/2$.

4 In the **Height** edit field, type $L+D_3/2-.03$.

5 In the **Position** edit field, type $x:-L_1-d_3/2$, $y: 0$, $z: d$.

5 In the **Axis** edit field, type $x: 1$, $y: 0$, $z: 0$.

Work Plan 1

1 In the **Model Builder** window, under **Model 1**, right-click **Geometry 1** and choose **Work Plane**.

2 In the **Geometry**, under work plane, right-click and choose **Circle**.

3 In the **Circle** settings window, locate the **Size and Shape** section.

4 In the **Radius** edit field, type $D_2/2$.

5 In the **Position** edit field, choose **Base: Center**, and type $x: 0$, $y: d$.

6 In the **Geometry**, under work plane, right-click and choose **Circle**.

7 In the **Circle** settings window, locate the **Size and Shape** section.

8 In the **Radius** edit field, type $D_1/2$.

9 In the **Position** edit field, choose **Base: Center**, and type $x: 0$, $y: d$.

10 In the **Geometry**, under work plane, right-click and choose **Boolean Operation>Differences**.

11 In the **Difference** settings window, locate the **Objects to add** and **Objects to subtract** section.

12 In the **Objects to add** setting, choose **C1**.

13 In the **Objects to subtract** setting, choose **C2**.

14 In the **Model Builder** window, under **Work Plane 1**, right-click and choose **Extrude**.

15 In the **Extrude** settings window, specify the **Distances** and type: $L_2+0.03$.

Work Plan 2

1 In the **Model Builder** window, under **Model 1**, right-click **Geometry 1** and choose **Work Plane**.

2 In the **Geometry**, under work plane, right-click and choose **Circle**.

3 In the **Circle** settings window, locate the **Size and Shape** section.

4 In the **Radius** edit field, type $D_1/2$.

5 In the **Position** edit field, choose **Base**: Center, and type x: 0, y: d.

6 In the **Model Builder** window, under **Work Plane 1**, right-click and choose **Extrude**.

7 In the **Extrude** settings window, specify the **Distances** and type: $L_2+L_3+0.03$.

Work Plan 3

1 In the **Model Builder** window, under **Model 1**, right-click **Geometry 1** and choose **Work Plane**.

2 In the **Geometry**, under work plane, right-click and choose **Circle**.

3 In the **Circle** settings window, locate the **Size and Shape** section.

4 In the **Radius** edit field, type $D_2/2$.

5 In the **Position** edit field, choose **Base**: Center, and type x: 0, y: d.

6 In the **Geometry**, under work plane, right-click and choose **Circle**.

7 In the **Circle** settings window, locate the **Size and Shape** section.

8 In the **Radius** edit field, type $D_1/2$.

9 In the **Position** edit field, choose **Base: Center**, and type x: 0, y: d.

10 In the **Geometry**, under work plane, right-click and choose **Boolean Operation>Differences**.

11 In the **Difference** settings window, locate the **Objects to add** and **Objects to subtract** section.

12 In the **Objects to add** setting, choose **C1**.

13 In the **Objects to subtract** setting, choose **C2**.

14 In the **Model Builder** window, under **Work Plane 1**, right-click and choose **Extrude**.

15 In the **Extrude** settings window, specify the **Distances** and type: L_3.

Block 1

1 In the **Model Builder** window, under **Model 1**, right-click **Geometry 1** and choose **Block**.

2 In the **Block** settings window, locate the **Size and Shape** section.

3 In the **Width** edit field, type a.

4 In the **Depth** edit field, type a.

5 In the **Height** edit field, type a.

6 In the **Position** edit field, choose **Base: Center**, and type x0, y: 0, z: a/2.

7 In the **Axis** edit field, type x: 0, y: 0, z: 1.

Block 2

1 In the **Model Builder** window, under **Model 1**, right-click **Geometry 1** and choose **Block**.

2 In the **Block** settings window, locate the **Size and Shape** section.

3 In the **Width** edit field, type b_3+a+b_4 .

4 In the **Depth** edit field, type b_1+a+b_2 .

5 In the **Height** edit field, type b_5+a+b_6 .

6 In the **Position** edit field, choose **Base:** Center, and type x: $(b_4-b_3)/2$, y: $(b_1-b_2)/2$, z: $b_5+a-b_6)/2$.

7 In the **Axis** edit field, type x: 0, y: 0, z: 1.

Block 3

1 In the **Model Builder** window, under **Model 1**, right-click **Geometry 1** and choose **Block**.

2 In the **Block** settings window, locate the **Size and Shape** section.

3 In the **Width** edit field, type b_3+a+b_4 .

4 In the **Depth** edit field, type t.

5 In the **Height** edit field, type b_5+a+b_6 .

6 In the **Position** edit field, choose **Base:** Corner, and type x: $-(b_3+a/2)$, y: $-(b_2+a/2)0$, z: $-(a_{13})$.

7 In the **Axis** edit field, type x: 0, y: 0, z: 1.

M A T E R I A L S

1 In the **Model Builder** window, under **Model 1**, right-click **Materials** and choose **Open Material Browser**.

2 In the **Material Browser** window, locate the **Materials** section.

3 In the tree, select **Built-In>Copper**.

4 Right-click and choose **Add Material to Model** from the menu.

5 In the tree, select **Built-In>Acrylic Plastic**.

6 Right-click and choose **Add Material to Model** from the menu.

7 In the tree, select **Built-In>Water**.

8 Right-click and choose **Add Material to Model** from the menu.

9 In the tree, select **Built-In>Air**.

10 Right-click and choose **Add Material to Model** from the menu.

11 Right-click **Material** and choose **Material**.

12 Go to the **Rename Material** dialog box and type Dielectric in the **New name** edit field.

13 Click **OK**.

Copper

1 In the **Model Builder** window, under **Model 1>Materials**, click **Copper**.

2 Select Domain 4, 5, 6, 7, and 9.

Acrylic Plastic

1 In the **Model Builder** window, under **Model 1>Materials**, click **Acrylic plastic**.

2 Select Domain 10, 11, 12, 14, and 58.

Water

1 In the **Model Builder** window, under **Model 1>Materials**, click **Water**.

2 Select Domain 3 only.

Air

1 In the **Model Builder** window, under **Model 1>Materials**, click **Air**.

2 Select Domain 1, and 2.

Dielectric

1 In the **Model Builder** window, under **Model 1>Materials**, click **Dielectric**.

2 Select Domain 8, and 9.

3 In the **Material** settings window, locate the **Material Contents** section.

4 In the table, enter the following settings:

Table A.2 Dielectric Properties

Property	name	Value	Unit	Property group
Electric Conductivity	sigma	0	S/m	Basic
Relative Permittivity	epsilon _r	2.03	1	Basic
Relative Permeability	mu _r	1	1	Basic

ELECTROMAGNETIC WAVES, FREQUENCY DOMAIN*Electromagnetic Waves (emw)*

- 1** In the **Model Builder** window, click **Electromagnetic Waves (emw)**.
- 2** In the **Electromagnetic Waves** settings window, select the **Domains**.
- 3** From the **Selection** list, choose **Manual**.
- 2** Select Domain 1, 2, 3, 8, and 10.

Perfect Electric Conductor

- 1** In the **Model Builder** window, right-click **Electromagnetic Waves (emw)** and choose **Perfect Electric Conductor**.
- 2** In the **Perfect Electric Conductor** settings window, locate the **Boundary Selection** section.
- 3** Select Boundaries 15, 16, 17, 18, 19, 20, 21, 24, 25, 31, 32, 34, 35, 38, 39, 41, 42, 43, 44, 45, 46, 50, 51, 53, 54, and 57.

Port 1

- 1** In the **Model Builder** window, right-click **Electromagnetic Waves**, and choose the boundary condition **Port**.
- 2** In the **Port** settings window, locate the **Boundary Selection** section.
- 3** Select Boundary 37.
- 4** Locate the **Port Properties** section. From the **Type of port** list, choose **Coaxial**.
- 5** From the **Wave excitation at this port** list, choose **On**.

Perfectly Matched Layer

1 In the **Model Builder** window, right-click **Electromagnetic Waves (emw)**, and choose **perfectly Matched Layer**.

2 In the **Perfectly Matched Layer** settings window, locate the **Domain Selection** section.

3 Select Domain 1.

MESH

In order to control the study time and to get a good accuracy, the mesh should be especially defined by the user.

1 In the **Model Builder** window, under **Model 1**, right-click **Mesh 1** and choose **Free Tetrahedral**.

Size

1 In the **Model Builder** window, under **Model 1>Mesh 1**, click **Size**.

2 In the **Size** settings window, locate the **Element Size** section.

3 From the **Predefined** list, choose **Normal**.

Size 1

1 In the **Model Builder** window, under **Model 1>Mesh 1**, right-click **Free Tetrahedral 1** and choose **Size**.

2 In the **Size** settings window, locate the **Geometric Entity Selection** section.

3 From the **Geometric entity level** list, choose **Domain**.

4 From the **Selection** list, choose 3.

5 Locate the **Element Size** section. From the **Predefined** list, choose **Fine**.

Size 2

1 In the **Model Builder** window, under **Model 1>Mesh 1**, right-click **Free Tetrahedral 2** and choose **Size**.

2 In the **Size** settings window, locate the **Geometric Entity Selection** section.

3 From the **Geometric entity level** list, choose **Domain**.

4 From the **Selection** list, choose 2, 8, and 10.

5 Locate the **Element Size** section. From the **Predefined** list, choose **Normal**.

Sweep 1

1 In the **Model Builder** window, under **Model 1>Mesh 1**, right-click **Sweep**.

2 In the **Size** settings window, locate the **Geometric Entity Selection** section.

3 From the **Geometric entity level** list, choose **Domain**.

4 From the **Selection** list, choose 1.

5 Locate the **Element Size** section. From the **Predefined** list, choose **Extremely Coarse**.

STUDY 1

Step 1: Frequency Domain

1 In the **Model Builder** window, under **Study 1**, click **Step 1: Frequency Domain**.

2 In the **Frequency Domain** settings window, locate the **Study Settings** section.

3 In the **Frequencies** edit field, type f.

4 In the **Model Builder** window, click **Study 1**.

5 Click the **Compute** button.

R E S U L T S

3D Plot Group 1

1 In the **Model Builder** window, right-click **Results**, and choose **3D Plot Group**.

2 Right-click **3D Plot Group 1** and choose **Slice**.

3 In the **Slice** settings window, click **Replace Expression** in the upper-right corner of the **Expression** section. From the menu, choose any component of an interest. You can also simply type **abs (Ez)**.

4 Locate the **Plane Data** section. From the **Plane** list, choose **xz-planes**.

5 From the **Entry method** list, choose **Coordinates**.

6 In the **z-coordinates** edit field, type .08.

Although the component of interest is the magnitude of E_z ($|E_z|$), for this model to be compared with the experimental results of Sangrey's (2011), various plots of other components of the electromagnetic field can be also obtained.

APPENDIX B

Simulation of a Resonant Cavity for the Modified Experimental Setup

Simulation of a Resonant Cavity for the Modified Experimental Setup

Modeling Instruction:

MODEL WIZARD

- 1 Go to the **Model Wizard** window.
- 2 Click **Next**.
- 3 In the **Add physics** tree, select **Radio Frequency>Electromagnetic Waves, Frequency Domain (emw)**.
- 4 Click **Next**.
- 5 Find the **Studies** subsection. In the tree, select **Preset Studies>Frequency Domain**.
- 6 Click **Finish**.

GLOBAL DEFINITIONS

To help in creating the geometry, define some parameters defining its dimensions.

Parameters

- 1 In the **Model Builder** window, right-click **Global Definitions**, and choose **Parameters**.
- 2 In the **Parameters** settings window, locate the **Parameters** section.
- 3 In the table, enter the following settings:

Table B.1 List of parameters used for modeling

Name	Expression
D_1	2[mm]
D_2	7[mm]
D_3	7[mm]
D_4	10[mm]

Note that as long as you specify the unit in a bracket in the table, you can use different dimensions for length.

G E O M E T R Y 1

Block 1

1 In the **Model Builder** window, under **Model 1**, right-click **Geometry 1** and choose **Block**.

2 In the **Block** settings window, locate the **Size and Shape** section.

3 In the **Width** edit field, type a .

4 In the **Depth** edit field, type a .

5 In the **Height** edit field, type a .

6 In the **Position** edit field, choose **Base: Center**, and type $x: 0, y: 0, z: a/2$.

7 In the **Axis** edit field, type $x: 0, y: 0, z: 1$.

Work Plan 1

1 In the **Model Builder** window, under **Model 1**, right-click **Geometry 1** and choose **Work Plane**.

2 In the **Geometry**, under work plane, right-click and choose **Circle**.

3 In the **Circle** settings window, locate the **Size and Shape** section.

4 In the **Radius** edit field, type $D_2/2$.

5 In the **Position** edit field, choose **Base: Center**, and type $x: 0, y: d$.

6 In the **Geometry**, under work plane, right-click and choose **Circle**.

7 In the **Circle** settings window, locate the **Size and Shape** section.

8 In the **Radius** edit field, type $D_1/2$.

9 In the **Position** edit field, choose **Base: Center**, and type $x: 0, y: d$.

10 In the **Geometry**, under work plane, right-click and choose **Boolean Operation>Differences**.

11 In the **Difference** settings window, locate the **Objects to add** and **Objects to subtract** section.

12 In the **Objects to add** setting, choose **C1**.

13 In the **Objects to subtract** setting, choose **C2**.

14 In the **Model Builder** window, under **Work Plane 1**, right-click and choose **Extrude**.

15 In the **Extrude** settings window, specify the **Distances** and type: 0.06.

Work Plan 2

1 In the **Model Builder** window, under **Model 1**, right-click **Geometry 1** and choose **Work Plane**.

2 In the **Geometry**, under work plane, right-click and choose **Circle**.

3 In the **Circle** settings window, locate the **Size and Shape** section.

4 In the **Radius** edit field, type $D_1/2$.

5 In the **Position** edit field, choose **Base**: Center, and type x: 0, y: d.

6 In the **Model Builder** window, under **Work Plane 1**, right-click and choose **Extrude**.

7 In the **Extrude** settings window, specify the **Distances** and type: 0.06.

Helix 1

1 In the **Model Builder** window, under **Model 1**, right-click **Geometry 1** and choose **More Primitives>Helix**.

2 In the **Helix** settings window, locate the **Size and Shape** section.

3 In the **Number of turns** edit field, type 0.5.

4 In the **Major Radius** edit field, type 0.03.

5 In the **Minor Radius** edit field, type $D_1/2$.

6 In the **Axial Pitch** edit field, type .0001.

7 In the **Radial Pitch** edit field, type 0.

8 In the **Chirality** edit field, choose **Left handed**.

9 In the **End Caps** edit field, choose **Parallel to axis**.

10 In the **Position** edit field, type x: 0.03, y: 0, z: 0.38.

11 In the **Axis** edit field, type x: 0, y: 1, z: 0.

Helix 2

1 In the **Model Builder** window, under **Model 1**, right-click **Geometry 1** and choose **More Primitives>Helix**.

2 In the **Helix** settings window, locate the **Size and Shape** section.

3 In the **Number of turns** edit field, type 0.5.

4 In the **Major Radius** edit field, type 0.03.

5 In the **Minor Radius** edit field, type $D_2/2$.

6 In the **Axial Pitch** edit field, type .0001.

7 In the **Radial Pitch** edit field, type 0.

8 In the **Chirality** edit field, choose **Left handed**.

9 In the **End Caps** edit field, choose **Parallel to axis**.

10 In the **Position** edit field, type x: 0.03, y: 0, z: 0.38.

11 In the **Axis** edit field, type x: 0, y: 1, z: 0.

Move 1

1 In the **Model Builder** window, under **Model 1**, right-click **Geometry 1** and choose **Transform>Move**.

2 In the **Move** settings window, locate the **Displacement** section.

3 In the **Displacement** edit field, choose type x: $0.38/2-0.08$, y: 0, z: 0.

Mirror 1

1 In the **Model Builder** window, under **Model 1**, right-click **Geometry 1** and choose **Transform>Mirror**.

2 In the **Mirror** settings window, locate the **Point on Plane of Reflection** section.

3 In the **Point on Plane of Reflection** edit field, type x: $(.1665+.1135)/2$, y: 0, z: 0.38

3 In the **Normal Vector to Plane Reflection** edit field, type x: 1, y: 0, z: 0

Move 2

1 In the **Model Builder** window, under **Model 1**, right-click **Geometry 1** and choose **Transform>Move**.

2 In the **Move** settings window, locate the **Displacement** section.

3 In the **Displacement** edit field, type x: 0.014, y: 0, z: 0.

Mirror 2

1 In the **Model Builder** window, under **Model 1**, right-click **Geometry 1** and choose **Transform>Mirror**.

2 In the **Mirror** settings window, locate the **Point on Plane of Reflection** section.

3 In the **Point on Plane of Reflection** edit field, type x: 0, y: 0, z: 0.38

3 In the **Normal Vector to Plane Reflection** edit field, type x: 1, y: 0, z: 0

M A T E R I A L S

1 In the **Model Builder** window, under **Model 1**, right-click **Materials** and choose **Open Material Browser**.

2 In the **Material Browser** window, locate the **Materials** section.

3 In the tree, select **Built-In>Copper**.

4 Right-click and choose **Add Material to Model** from the menu.

7 In the tree, select **Built-In>Water**.

10 Right-click and choose **Add Material to Model** from the menu.

11 Right-click **Material** and choose **Material**.

12 Go to the **Rename Material** dialog box and type Dielectric in the **New name** edit field.

13 Click **OK**.

Copper

- 1 In the **Model Builder** window, under **Model 1>Materials**, click **Copper**.
- 2 Select Domain 4, and 5.

Water

- 1 In the **Model Builder** window, under **Model 1>Materials**, click **Water**.
- 2 Select Domain 1 only.

Dielectric

- 1 In the **Model Builder** window, under **Model 1>Materials**, click **Dielectric**.
- 2 Select Domain 2, and 3.
- 3 In the **Material** settings window, locate the **Material Contents** section.
- 4 In the table, enter the following settings:

Table B.2 Dielectric Properties

Property	name	Value	Unit	Property group
Electric Conductivity	sigma	0	S/m	Basic
Relative Permittivity	epsilon _r	2.03	1	Basic
Relative Permeability	mu _r	1	1	Basic

E L E C T R O M A G N E T I C W A V E S, F R E Q U E N C Y D O M A I N*Electromagnetic Waves (emw)*

- 1 In the **Model Builder** window, click **Electromagnetic Waves (emw)**.
- 2 In the **Electromagnetic Waves** settings window, select the **Domains**.
- 3 From the **Selection** list, choose **Manual**.
- 2 Select Domain 1, 2, and 3.

Perfect Electric Conductor

- 1 In the **Model Builder** window, right-click **Electromagnetic Waves (emw)**, and choose **Perfect Electric Conductor**.

2 In the **Perfect Electric Conductor** settings window, locate the **Boundary Selection** section.

3 Select Boundaries 12, 13, 15, 16, 20, 21, 22, and 23.

Port 1

1 In the **Model Builder** window, right-click **Electromagnetic Waves**, and choose the boundary condition **Port**.

2 In the **Port** settings window, locate the **Boundary Selection** section.

3 Select Boundary 11.

4 Locate the **Port Properties** section. From the **Type of port** list, choose **Coaxial**.

5 From the **Wave excitation at this port** list, choose **On**.

MESH

Because of the reasonable size of the geometry, it is possible to have a uniform mesh size for the entire domain under study.

1 In the **Model Builder** window, under **Model 1**, right-click **Mesh 1** and choose **Physics-controlled mesh**.

2 In the **Element Size** setting, choose **Normal**.

STUDY 1

Step 1: Frequency Domain

1 In the **Model Builder** window, under **Study 1**, click **Step 1: Frequency Domain**.

2 In the **Frequency Domain** settings window, locate the **Study Settings** section.

3 In the **Frequencies** edit field, type 65e6.

4 In the **Model Builder** window, click **Study 1**.

5 Click the **Compute** button.

RESULTS

3D Plot Group 1

- 1** In the **Model Builder** window, right-click **Results**, and choose **3D Plot Group**.
- 2** Right-click **3D Plot Group 1** and choose **Slice**.
- 3** In the **Slice** settings window, click **Replace Expression** in the upper-right corner of the **Expression** section. From the menu, choose any component of an interest. You can also simply type **abs (Ez)**.
- 4** Locate the **Plane Data** section. From the **Plane** list, choose **yz-planes**.
- 5** From the **Entry method** list, choose **Coordinates**.
- 6** In the **z-coordinates** edit field, type 0

Although the component of an interest is $\text{abs}(E_z)$ for this model to be compared with the experimental electric field measurement results, various plots of other components of the electromagnetic field can be also obtained.

APPENDIX C

**Script (m.file) Code Developed in MATLAB for Calculation of Diffusion Coefficient,
D, in Zone 4**

**Script (m.file) Code Developed in MATLAB for Calculation of Diffusion Coefficient,
D, in Zone 4**

After importing the matrix that contains the concentration of the 208 nodes at 130 times, pixDyeR, the code can be run in MATLAB and the resultant D_avg would be the average diffusion coefficient

```
dt=60; % time steps of the pictures are 60 sec.
dx=2; % distance of the nodes in horizontal direction
dy=2; % distance of the nodes in vertical direction

D_mat=zeros(208,128);
Numi=zeros(208,128);
Den_1=zeros(208,128);
Den_2=zeros(208,128);
Denum=zeros(208,128);
Denumi=zeros(208,128);
N=0;
D_av=0;
P=zeros(208,1);

for m=1:128
    for j=1:5
        for k=123:127

            for i=k+(j-1)*16

                Numi(i,m)=((pixDyeR(i,m+1)-pixDyeR(i,m))/dt);
                Den_1(i,m)=pixDyeR(i-1,m)-2*pixDyeR(i,m)+pixDyeR(i+1,m);
                Den_2(i,m)=pixDyeR(i-16,m)-2*pixDyeR(i,m)+pixDyeR(i+16,m);
                Denum(i,m)=Den_1(i,m)+Den_2(i,m);
                Denumi(i,m)=Denum(i,m)/(2*dx);

                if rem(i,16)==0
                    D_mat(i,m)=0;

                elseif rem(i,16)==1
                    D_mat(i,m)=0;

                elseif Denumi(i,m)==0
                    D_mat(i,m)=0;

                else
                    D_mat(i,m)=-Numi(i,m)/(Denumi(i,m));

                end

            end

        end

    end

end
```

```
        end
    end
end

D_mx=max(max(D_mat));
D_mn=min(min(D_mat));
DFil=[];

% Calculation of average diffusion coefficient with the condition that
it should be larger than 0 and smaller than .001cm2/s.

for j=1:128
    for k=1:208
        if (D_mat(k,j)>0) && (D_mat(k,j)<.001)
            D_av=D_av+D_mat(k,j);
            N=N+1;
            DFil=[DFil,D_mat(k,j)];
            P(k)=P(k)+1;
        end
    end
end

D_avg=(D_av)/N; % the averaged diffusion coefficient
```

APPENDIX D

**Script (m.file) Code Developed in MATLAB for Calculation of Electric Field
Gradient for Dielectrophoresis Study**

Script (m.file) Code Developed in MATLAB for Calculation of Electric Field Gradient for Dielectrophoresis Study

After importing the matrix that contains the electric field magnitude at the regular grid nodes from COMSOL Multiphysics, the code can be run in MATLAB, and the resultant plots show the direction of the gradient of the magnitude of the electric field squared in X and Z directions.

```
% Import the matrix containing the magnitude of the
electric field of the nodes from COMSOL Multiphysics and
call it E.
```

```
E_norm=zeros(16,19,19);
```

```
for i=1:16
    for k=1:19
        for j=1:19
            E_norm(17-i, j, k)=E(j+(k-1)*19+(i-1)*19*19, 4);
        end
    end
end
```

```
delx=zeros(15,18,18);
dely=zeros(15,18,18);
delz=zeros(15,18,18);
dx=.02; % The distance of the nodes in x the direction.
dy=.02; % The distance of the nodes in y the direction.
dz=.02; % The distance of the nodes in z the direction.
```

```
for i=16:-1:2
    for j=1:18
        for k=1:18
            delx(i-1, j, k)=((E_norm(i, j+1, k))-(E_norm(i, j, k)))/dx;
            dely(i-1, j, k)=((E_norm(i, j, k+1))-(E_norm(i, j, k)))/dy;
            delz(i-1, j, k)=((E_norm(i-1, j, k))-(E_norm(i, j, k)))/dz;
        end
    end
end
```

```
DEF_x=zeros(15,18);
DEF_y=zeros(15,18);
DEF_z=zeros(15,18);
```

```
for i=1:15
```

```
for j=1:18
    k=1;
    while k<19

        DEF_x(i,j)=delx(i,j,k)+DEF_x(i,j);
        DEF_y(i,j)=dely(i,j,k)+DEF_y(i,j);
        DEF_z(i,j)=delz(i,j,k)+DEF_z(i,j);
        k=k+1;
    end
end
end
end
%
DEF_x_flip= flipud (DEF_x);
DEF_z_flip= flipud (DEF_z);

contourf(DEF_x_flip);colorbar;title('Fx')
figure
contourf(DEF_z_flip);colorbar;title('Fz')
```

APPENDIX E

Script (m.file) Code Developed in MATLAB to Study Pixel Intensity Summation

Script (m.file) Code Developed in MATLAB to Study Pixel Intensity Summation

```

clear all;clc;

frame = [1100 300;4350 3300]; %This is the upper region for 75MHz
pix.
corners = [500 200;2750 1450]; %This is the upper region for 75MHz
pix.
DirName = 'E:\For Elisa\75MHz_30Watts_30sec\';
im2 = imread([DirName 'DPP_0001.TIF']);
imshow(im2(frame(1,2):frame(2,2), frame(1,1):frame(2,1)), []);
hold on
plot([corners(1,1) corners(2,1) corners(2,1) corners(1,1)
corners(1,1)], ...
[corners(2,2) corners(2,2) corners(1,2) corners(1,2)
corners(2,2)], ...
'LineWidth', 4);
hold off
%%

step=3; % step betwvn picture numbers. 1step=30sec.
Start_time=1; %picture #
End_time=40;
N=floor((End_time-Start_time)/step);

%%
%-----
--
%-----75MHz-----
--
%-----
--

I=zeros(1201,2221,N);
BG=zeros(1201,2221);
hh=0;
corners = [1625 550;3845 1750]; %This is the upper region for 75MHz
pix.
DirName = 'E:\For Elisa\75MHz_30Watts_30sec\';
im2 = imread([DirName 'DPP_0001.TIF']);
figure
imshow(im2(corners(1,2):corners(2,2), corners(1,1):corners(2,1)), []);
C0 = im2(corners(1,2):corners(2,2), corners(1,1):corners(2,1));

for jj=1:1201
    for kk=1:2221

        BG(jj, kk)=C0(jj, kk);

    end
end

for ii = Start_time:step:End_time,

```

```

        hh=hh+1;
        im_test = imread([DirName 'DPP_' num2str(ii,'%04d') '.TIF']);
%this is the file to open and get intensity values from
        im_crop = im_test(corners(1,2):corners(2,2),
corners(1,1):corners(2,1));

        for jj=1:1201
            for kk=1:2221

                I(jj,kk,hh)=im_test(jj,kk);

            end
        end
end

clear im_test;
clear im_crop;
clear C0;
clear im2;

I_dif=zeros(1201,2221,N);
for kk=1:hh
I_dif(:, :, kk)=I(:, :, kk)-BG(:, :);
end

clear BG;
clear I;

sum_75=zeros(N,1);
for kk=1:N
    for ii=1:1201
        for jj=1:2221

            sum_75(kk,1)=sum_75(kk,1)+I_dif(ii, jj, kk);

        end
    end
end

clear I_dif;
%%

%-----
%-----
%-----0Watts-----
%-----
%-----

I=zeros(1201,2221,N);
BG=zeros(1201,2221);
hh=0;
corners = [1215 550;3435 1750]; %This is the upper region for the
unstimulated pix.

```

```

DirName = 'E:\For Elisa\Unstimulated\';
im2 = imread([DirName 'DPP_0001.TIF']);
imshow(im2(corners(1,2):corners(2,2), corners(1,1):corners(2,1)), []);
C0 = im2(corners(1,2):corners(2,2), corners(1,1):corners(2,1));

for jj=1:1201
    for kk=1:2221

        BG(jj, kk)=C0(jj, kk);

    end
end

for ii = Start_time:step:End_time,

    hh=hh+1;
    im_test = imread([DirName 'DPP_' num2str(ii, '%04d') '.TIF']);
    %this is the file to open and get intensity values from
    im_crop = im_test(corners(1,2):corners(2,2),
corners(1,1):corners(2,1));

    for jj=1:1201
        for kk=1:2221

            I(jj, kk, hh)=im_test(jj, kk);

        end
    end
end

clear im_test;
clear im_crop;
clear C0;
clear im2;

I_dif=zeros(1201,2221,N);
for kk=1:hh
    I_dif(:, :, kk)=I(:, :, kk)-BG(:, :);
end

clear BG;
clear I;

sum_0=zeros(N,1);
for kk=1:N
    for ii=1:1201
        for jj=1:2221

            sum_0(kk,1)=sum_0(kk,1)+I_dif(ii, jj, kk);

        end
    end
end
end

```

```

clear I_dif;
%%

%-----
%-----30Watts-----
%-----

f=zeros(1201,2221,N);
BG=zeros(1201,2221);
hh=0;
corners = [1520 600;3740 1800]; %This is the upper region for the
stimulated pix.
DirName = 'E:\For Elisa\second run\30W-5second,3may,5ccdye-\New folder
(2)\';
im2 = imread([DirName 'DPP_0001.TIF']);
%imshow(im2(corners(1,2):corners(2,2), corners(1,1):corners(2,1)),[]);
C0 = im2(corners(1,2):corners(2,2), corners(1,1):corners(2,1));

for jj=1:1201
    for kk=1:2221

        BG(jj,kk)=C0(jj,kk);

    end
end

for ii = Start_time:step:End_time,

    hh=hh+1;
    im_test = imread([DirName 'DPP_' num2str(ii,'%04d') '.TIF']);
%this is the file to open and get intensity values from
    im_crop = im_test(corners(1,2):corners(2,2),
corners(1,1):corners(2,1));

    for jj=1:1201
        for kk=1:2221

            f(jj,kk,hh)=im_test(jj,kk);

        end
    end
end

clear im_test;
clear im_crop;
clear C0;
clear im2;

f_dif=zeros(1201,2221,N);
for kk=1:hh
f_dif(:, :, kk)=f(:, :, kk)-BG(:, :);

```

```

end

clear BG;
clear f;

sum_30=zeros(N,1);
for kk=1:N
    for ii=1:1201
        for jj=1:2221

            sum_30(kk,1)=sum_30(kk,1)+f_dif(ii,jj,kk);

        end
    end
end

clear f_dif;
%%

%-----
%-----20Watts-----
%-----

g=zeros(1201,2221,N);
hh=0;
BG=zeros(1201,2221);
%corners = [1480 600;3700 1800]; %This is the upper region for the
stimulated pix.
corners = [1740 600;3960 1800];
%DirName = 'E:\For Elisa\second run\20Watts, 64 Mhz,25 apr\New
Folder\';
DirName = 'E:\For Elisa\second run\30 watts,63.9Mhz,20April\New
Folder\';
im2 = imread([DirName 'IMG_0001.TIF']);
imshow(im2(corners(1,2):corners(2,2), corners(1,1):corners(2,1)), []);
C0 = im2(corners(1,2):corners(2,2), corners(1,1):corners(2,1));
for jj=1:1201
    for kk=1:2221

        BG(jj,kk)=C0(jj,kk);

    end
end

for ii = Start_time:step:End_time,

    hh=hh+1;
    im_test = imread([DirName 'IMG_' num2str(ii,'%04d') '.TIF']);
%this is the file to open and get intensity values from
    im_crop = im_test(corners(1,2):corners(2,2),
corners(1,1):corners(2,1));

```

```

    for jj=1:1201
        for kk=1:2221

            g(jj, kk, hh)=im_test(jj, kk);

        end
    end
end

clear im_test;
clear im_crop;
clear C0;
clear im2;

g_dif=zeros(1201, 2221, N);
for kk=1:hh
    g_dif(:, :, kk)=g(:, :, kk)-BG(:, :);
end

clear BG;
clear g;

sum_20=zeros(N, 1);
for kk=1:N
    for ii=1:1201
        for jj=1:2221

            sum_20(kk, 1)=sum_20(kk, 1)+g_dif(ii, jj, kk);

        end
    end
end

clear g_dif;
%%

%-----
%-----
%-----10Watts-----
%-----
%-----

h=zeros(1201, 2221, N);
BG=zeros(1201, 2221);
hh=0;
corners = [1500 600; 3720 1800]; %This is the upper region for the
stimulated pix.
DirName = 'E:\For Elisa\New Folder\10watts, 64mhz, 24apr, main
runnt=10s\New Folder\';
%im2 = imread([DirName 'DPP_0001.TIF']);
im2 = imread([DirName 'IMG_0001.TIF']);
%imshow(im2(corners(1,2):corners(2,2), corners(1,1):corners(2,1)), []);

```

```

C0 = im2(corners(1,2):corners(2,2), corners(1,1):corners(2,1));
for jj=1:1201
    for kk=1:2221

        BG(jj,kk)=C0(jj,kk);

    end
end

for ii = Start_time:step:End_time,

    hh=hh+1;
    im_test = imread([DirName 'IMG_' num2str(ii,'%04d') '.TIF']);
%this
%is the file to open and get intensity values from
    im_test = imread([DirName 'DPP_' num2str(ii,'%04d') '.TIF']);
%this is the file to open and get intensity values from
    im_crop = im_test(corners(1,2):corners(2,2),
corners(1,1):corners(2,1));

    for jj=1:1201
        for kk=1:2221

            h(jj,kk,hh)=im_test(jj,kk);

        end
    end
end

clear im_test;
clear im_crop;
clear C0;
clear im2;

h_dif=zeros(1201,2221,N);
for kk=1:hh
h_dif(:, :, kk)=h(:, :, kk)-BG(:, :);
end

clear BG;
clear h;

sum_10=zeros(N,1);
for kk=1:N
    for ii=1:1201
        for jj=1:2221

            sum_10(kk,1)=sum_10(kk,1)+h_dif(ii, jj, kk);

        end
    end
end

clear h_dif;

```

```
%%  
  
figure(1)  
plot(sum_10, 'b', 'LineWidth', 2.5)  
hold on  
plot(sum_20, 'r', 'LineWidth', 2.5)  
hold on  
plot(sum_30, 'g', 'LineWidth', 2.5)
```

APPENDIX F

Script (m.file) Code Developed in MATLAB to Study the Fingers Width vs. Power

Script (m.file) Code Developed in MATLAB to Study the Fingers Width vs. Power

```

Clear all; clc;%%
step=3; % step betwwn picture numbers. 1step=30sec.
Start_time=1; %picture #
End_time=40;
N=floor((End_time-Start_time)/step);
f=zeros(1201,551,N);
%
%%
% -----
% -----30Watts_2nd Run-----
% -----
% -----
corners = [2100 550;2650 1750]; % This is the finger zone.
DirName = 'F:\For Elisa\Test Pix\2nd Run\64_30_30 sec\TIFF\'; % data
for experiment of interest
im= imread([DirName 'DPP_0001.TIF']);
imshow(im(corners(1,2):corners(2,2), corners(1,1):corners(2,1)), []);

hh=0;

for ii = Start_time:step:End_time,

    hh=hh+1;
    im_test = imread([DirName 'DPP_' num2str(ii,'%04d') '.TIF']);
%this is the file to open and get intensity values from
    im_crop = im_test(corners(1,2):corners(2,2),
corners(1,1):corners(2,1));
    f(:, :, hh)=im_crop;

end

clear corners;
clear im;
clear im_crop;
clear im_test;

d=zeros(1201,551,hh);
for gg=1:hh

    d(:, :, gg)=f(:, :, gg)-f(:, :, 1);

end

clear f;

n_30=zeros(701,hh);
for k=1:hh
    for i=500:1200
        for j=1:551

```

```

        if d(i,j,k)<0
            n_30(i-499,k)=n_30(i-499,k)+d(i,j,k);
        end

    end
end
end

clear d;

n_avg3_2=zeros(701,1);
for i=1:701
    for k=1:hh
        n_avg3_2(i)=n_30(i,k)+n_avg3_2(i);
    end
end

clear n_30;

n_avg3_2=flipud(n_avg3_2);

%%
%-----
%-----20Watts_2nd Run-----
%-----
%-----
corners = [2300 550;2850 1750]; % This is the finger zone.
DirName = 'F:\For Elisa\Test Pix\2nd Run\64_20_30 sec\TIFF\';
im= imread([DirName 'DPP_0001.TIF']);
imshow(im(corners(1,2):corners(2,2), corners(1,1):corners(2,1)), []);

hh=0;

for ii = Start_time:step:End_time,

    hh=hh+1;
    im_test = imread([DirName 'DPP_' num2str(ii,'%04d') '.TIF']);
    %this is the file to open and get intensity values from
    im_crop = im_test(corners(1,2):corners(2,2),
corners(1,1):corners(2,1));
    f(:, :, hh)=im_crop;

end

clear corners;
clear im;
clear im_crop;

```

```

clear im_test;

d=zeros(1201,551,hh);
for gg=1:hh
    d(:,:,gg)=f(:,:,gg)-f(:,:,1);
end

clear f;

n_20=zeros(701,hh);
for k=1:hh
    for i=500:1200
        for j=1:551
            if d(i,j,k)<0
                n_20(i-499,k)=n_20(i-499,k)+d(i,j,k);
            end
        end
    end
end

n_avg2_2=zeros(701,1);
for i=1:701
    for k=1:hh
        n_avg2_2(i)=n_20(i,k)+n_avg2_2(i);
    end
end

clear n_20;

n_avg2_2=flipud(n_avg2_2);

%%
%-----
%-----
%-----10Watts_2nd Run-----
%-----
%-----
%-----
hh=0;
DirName = 'F:\For Elisa\Test Pix\2nd Run\64_10-30 sec\0-10\TIFF\';
corners = [2300 560;2850 1760];
im= imread([DirName 'DPP_0001.TIF']);

```

```

imshow(im(corners(1,2):corners(2,2), corners(1,1):corners(2,1)), []);

for ii = Start_time:step:End_time,

    hh=hh+1;
    im_test = imread([DirName 'DPP_' num2str(ii, '%04d') '.TIF']);
    %this
    %is the file to open and get intensity values from
    im_crop = im_test(corners(1,2):corners(2,2),
corners(1,1):corners(2,1));
    f(:, :, hh)=im_crop;

end

clear corners;
clear im;
clear im_crop;
clear im_test;

d=zeros(1201,551, hh);
for gg=1:hh

    d(:, :, gg)=f(:, :, gg)-f(:, :, 1);

end

clear f;

n_10=zeros(701, hh);
for k=1:hh
    for i=500:1200
        for j=1:551

            if d(i, j, k)<0

                n_10(i-499, k)=n_10(i-499, k)+1;

            end

        end
    end
end

clear d;

n_avg1_2=zeros(701, 1);
for i=1:701
    for k=1:hh

        n_avg1_2(i)=n_10(i, k)+n_avg1_2(i);

    end
end

```

```
end

clear n_10;

n_avg1_2=flipud(n_avg1_2);

z=0:0.2:140;
figure
plot(n_avg1,z,'b','LineWidth',2.5)
hold on
plot(n_avg2,z,'g','LineWidth',2.5)
plot(n_avg3,z,'r','LineWidth',2.5)
xlabel('# of pixels containing dye','FontSize',11,'FontWeight','BOLD')
ylabel('Distance from the injection cup (mm)','FontSize',11,'FontWeight','BOLD')
legend('10W','20W','30W')
hold off
```